UNIVERSITÀ DEGLI STUDI DI PARMA

Doctoral Program in Industrial Engineering

NUMERICAL MODELLING OF ADHESIVE JOINTS DEBONDING UNDER FATIGUE LOADING

Doctoral Disertation by

Gregorio Giuliese

Supervisor:
Prof. Alessandro Pirondi

The Chair of the Doctoral Program:
Prof. Agostino Gambarotta

XXVII CYCLE

to Luisa

Abstract

Composite and hybrid metal/composite structures are nowadays present not only in the aerospace industry, but thanks to continuous performance improvement and cost reduction, also many more industrial fields are approaching the use of multimaterial structural elements.

This requires, in turn, extensive use of adhesive bonding and a more and more sophisticated capability to simulate and predict the strength of bonded connections where, for this purpose, analytical methods are being progressively integrated or replaced by finite element analysis (FEA). To ensure the safety of the resulting structures, it is imperative to understand their fatigue behaviour. Thus the rise of the application of adhesive bonding has gone hand in hand with the development of models capable to predict the fatigue life that is related to the initiation and propagation of defects starting at free edges of joining regions or other features, such as through-thickness holes.

The cohesive zone model (CZM) has found a wide acceptance as a tool for the simulation of debonding in adhesively bonded joints. This model is commonly used for the simulation of the quasi-static fracture problems, especially in the case of interface cracks such as in bonded joints and de-

lamination in composites. The possibility to simulate the growth of a crack without any remeshing requirements and the relatively easy possibility to manipulate the constitutive law of the cohesive elements makes the cohesive zone model attractive also for the fatigue crack growth simulation.

The purpose of this work is to develop the two-dimensional cohesive zone model presented by Pirondi and Moroni [66, 65, 67]. A cohesive damage model has been implemented by means of the USDFLD and URDFIL subroutines in the commercial software *Abaqus*, in order to take into account the damage produced by fatigue loading. The fatigue debonding of composite assemblies under Mode I, Mode II and mixed-Mode I/II loading conditions is simulated by the cohesive zone model. The cohesive zone model has been then extended to simulate the propagation of three-dimensional cracks with quasi-straight crack front. The CZM was tested on various joint geometries characterized by different mixed mode ratios, in order to verify accuracy, robustness and performance in terms of computational time. In order to investigate the model sensitivity to material behavior, two kind of materials were simulated, one representing an elastic, isotropic aluminum alloy and another one an elastic, orthotropic composite laminate. Lastly a new procedure for simulating fatigue debonding with cohesive zone is presented. Unlike the previous approaches, propagation of arbitrarily shaped cracks can be simulated.

The present work was supported by Regione Emilia Romagna within SPINNER 2013: Program Number 067/11 - “Sviluppo, caratterizzazione e modellazione di strutture in materiale composito intelligente”.

Contents

List of Figures

List of Tables

Nomenclature

a	crack length
a_0	initial crack length
A_d	damaged area of the representative element
A_e	nominal area ofthe representetive element (assumed to be the area associated with an Integration Point)
b	adherend width
C	coefficient of Paris-like law of fatigue carck growth
C_I	coefficient of mode I Paris-like law of fatigue crack growth
C_{II}	coefficient of mode II Paris-like law of fatigue crack growth
D	damage variable
da/dN	crack growth rate
E	Young's modulus
G	strain energy release rate
G_c	critical strain energy release rate
G_I	strain energy release rate in mode I
G_{eqC}	Critical Strain Energy Release Rate (mixed-mode)
G_{eq}	Equivalent Strain Energy Release Rate (mixed-mode)
G_{III}	strain energy release rate in mode III
G_{II}	strain energy release rate in mode II
G_{pl}	strain energy release rate upper limit used in the Paris law
h	adherend thickness

K	stress intensity factor
K_{12}^0	mode II initial (undamaged) stiffness
K_{22}^0	mode I initial (undamaged) stiffness
L	adherend length
L_0	overlap length
MM	mixed-mode ratio
n	exponent of mixed-mode I/II Paris-like law of fatigue crack growth
n_C	mixed-mode ratio exponent for determination of the value of "C" in the mixed-mode Paris-like law
n_I	exponent of mode I Paris-like law of fatigue crack growth
N_j	number of cycles at increment j
n_n	mixed-mode ratio exponent for determination of the value of "n" in the mixed-mode Paris-like law
n_{cz}	Number of elements lying on the process area
n_{II}	exponent of mode II Paris-like law of fatigue crack growth
N_i^j	increment of number of cycles in the element i at increment j
P_{max}	maximum load in fatigue cycle
P_{min}	minimum load in fatigue cycle
R	load ratio
s	path coordinate (J-integral)
t_A	adhesive thickness
W	strain energy density
$\Delta\sigma$	remote stress applied to a component
ΔD_{max}	maximum increment of damage in an increment of a simulation
ΔG_i^j	increment of damage in the element i at increment j
ΔG_{th}	threshold stress energy release rate cyclic range (from FCG test)
ΔK	stress intensity factor range
ΔK_{th}	threshold stress intensity factor range

ΔN^j_{min} minimum increment of number of cycles at increment j

δ normal/tangential sepration (cohesive model)

δ^0_{12} sliding corresponding to the maximum stress in the cohesive zone under mode II loading

δ^0_{22} opening corresponding to the maximum stress in the cohesive zone under mode I loading

δ^0_{23} sliding corresponding to the maximum stress in the cohesive zone under mode III loading

δ^0_m displacement corresponding to the onset of softening in mixed-mode loading

δ^c_m relative displacement corresponding to the total decohesion in mixed-mode loading

Γ_I area underlying the pure mode I cohesive law

Γ_{eq} mixed-mode cohesive energy

Γ_{II} area underlying the pure mode II cohesive law

Π path around the crak-tip (J-integral)

σ^0_{12max} maximum stress of a pure mode II cohesive law

σ^0_{22max} maximum stress of a pure mode I cohesive law

σ^0_{23max} maximum stress of a pure mode III cohesive law

$\overrightarrow{n}$ unit vector normal to the contour path

$\overrightarrow{T}$ traction vector

Chapter 1

Introduction

Composite materials and structural adhesively bonded joints are nowadays present in several fields beside the aerospace industry thanks to the continuous performance improvement and the cost reduction. However a sophisticated capability to simulate and predict the strength of bonded connection or composite part is absolutely necessary. For this purpose, analytical methods are being progressively integrated or replaced by finite element analysis (FEA).

1.1 Fracture phenomena in engineering

Many different areas in engineering are concerned with the evaluating the fracture strength and durability of constructions. Often the traditional strength theories, based on the determination of the induced stresses and the subsequent comparison with critical values, fail in predicting and avoiding fracture processes. The specific field which deals with fracture and failure processes in engineering materials and construction is called *fracture mechanics*. In this theory it is assumed that every component and every real material inevitably possesses flaws or other defects that can originate during the manufacturing process or the course of mechanical, thermal or corrosive service loading. The presence of these cracks modify the local stresses so that the classical strength criteria are insufficient for a correct design. The existence of such defects is explicitly assumed in fracture mechanics and modeled as crack of size a. Such a discrete crack is surrounded by defect-free material which is described by established material laws of continuum mechanics. Using computational methods, the stress and deformation states at the crack are determined.

The fracture of materials is a a process of the nucleation of micro-cavities or microcracks due to the breakage of atomic bonds from a nano/microscopic view point. From the macroscopic point of view, however, it is a process of the extension of cracks brought about by the coalescence of these micro-cavities. Between these two processes, there exists a mesoscopic process where the nucleation, growth and the coalescence of the microscopic cavities leads to the initiation of a macroscopic crack (see Fig. 1.1).

The development of cavities in the microscopic, mesoscopic and the macroscopic process of fracture in materials together with the resulting deterioration in their mechanical properties are called *damage* (Lemaitre and Caboche 1978,[2]). The *continumm damage mechanics* (CDM) is suitable for the modelling of micro-mechanical failure processes in

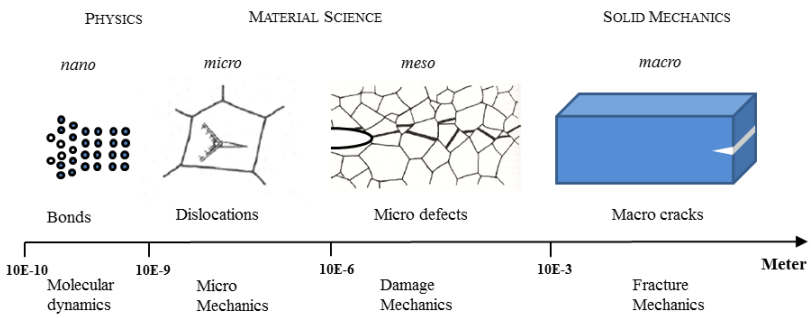

Figure 1.1: Fracture processes at different scales

a component, before a macro-crack is formed or for the modelling of the fracture process zone at the tip of a macro-crack.

In the next chapters delamination/debonding problems will be dealt with fracture mechanics and damage mechanics approaches. First it is necessary to introduce appropriate fracture-mechanical parameters to identify the loading conditions at the crack and the computational methods necessary for their evaluation.

1.2 Fracture parameters

The distinction between small scale yielding (SSY) and large scale yielding (LSY) is important with respect to the modelling of fracture. SSY correspond to case where the size of the plastic zone is much smaller than the size of the structure or component. In that case the overall behavior of the structure remains linear. LSY corresponds to the opposite case: a large portion of the specimen is plastically yielded and the overall behavior is non linear (Figure 1.2).

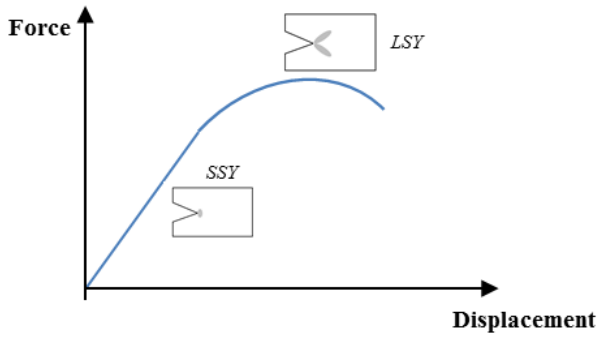

Figure 1.2: Overall behavior of a cracked structure (plastic zone in gray)

SSY can be analyzed using linear elastic fracture mechanics, LSY is analyzed using NLFM (Non Linear Fracture Mechanics)

1.2.1 Linear elastic fracture mechanics (LEFM)

It can be observed that to introduce a crack into an elastically stressed body one would have to balance the decrease in potential energy and the increase in surface energy resulting from the presence of the crack which creates new surfaces. The available amount of potential energy $-\Delta\Pi$, which is supplied by the external load and the elastically stored internal energy during the crack propagation by ΔA (the minus sign indicates the decrease of the potential energy), is called *energy release rate* and is defined for infinitesimal crack propagation as follows:

$$G = -\lim_{\Delta A} \frac{\Delta\Pi}{\Delta A} = -\frac{d\Pi}{dA} \tag{1.1}$$

Thus the crack extension occurs when G reaches a value required for material separation and formation of new surfaces. It depends on the material behavior and represents the critical material parameter . This energy balance during crack propagation, compiled by A. A. Griffith [1], has the form:

$$-\frac{d\Pi}{dA} = G = G_c \tag{1.2}$$

The value of G can be related to the applied loading using the expression of the stress tensor close to the crack tip. The literature treats three types of cracks, termed mode I, II, and III as illustrated in Figure 1.3. Mode I is a normal-opening mode and is the one we shall emphasize here, while modes II and III are shear sliding modes.

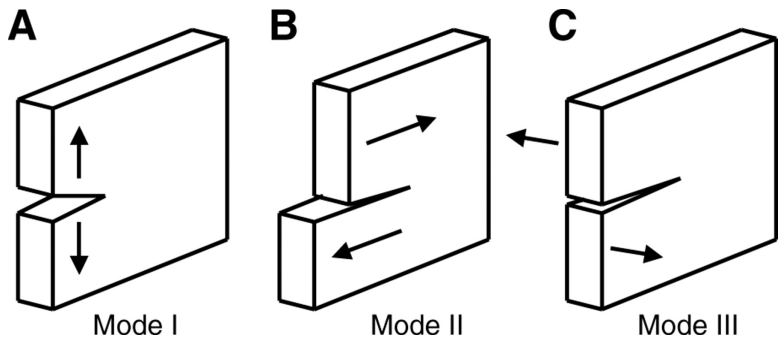

Figure 1.3: Fracture modes

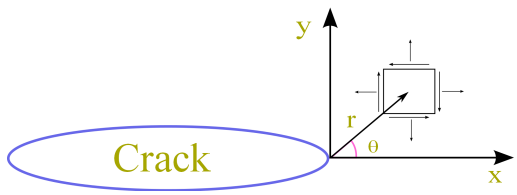

Figure 1.4: Local coordinate system at the crack tip

When defining a polar coordinate system (r, ϑ) with the origin at the crack tip (see Figure 1.4) the stress field in any linear elastic cracked body can be written as

$$\sigma_{ij} = \left(\frac{k}{\sqrt{r}}\right) f_{ij}(\theta) + other\,terms \tag{1.3}$$

where k is a constant and f_{ij} is dimensionless function of θ. The magnitude of k depends on sample geometry, the size and location of the crack, and loads on the part. As evident from Eq. (1.3) the stress near the crack tip varies with $1/\sqrt{r}$, regardless of the configuration of the cracked body. Note that when $r \to 0$ the stress approaches to ∞. In other words, when a body contains a crack, a strong concentration develops around a crack tip. Under mixed mode loading (I,II and III) each mode produces the $1/\sqrt{r}$ singularity at the crack tip, but the proportionality constant k and function f_{ij} in Eq. (1.3) depend on a specific mode. It is customary to define k in terms of the *stress intensity factor* K (SIF) and write

$$K = k\sqrt{2\pi} \tag{1.4}$$

Thus Eq. (1.3) becomes

$$\lim_{r\to 0} \sigma_{ij}^{(I,II,III)} = \frac{K_{(I,II,III)}}{\sqrt{2\pi r}} f_{ij}^{(I,II,III)}(\theta) \tag{1.5}$$

where *I, II, III* refer to individual modes. Individual contributions to a given stress component are additive.

The corresponding energy release rate is given by:

$$G = \begin{cases} \frac{1-\upsilon^2}{E}(K_I^2 + K_{II}^2) + \frac{1+\upsilon}{E}K_{III}^2 & plane\ strain \\ \\ \frac{1}{E}(K_I^2 + K_{II}^2) + \frac{1+\upsilon}{E}K_{III}^2 & plane\ stress \end{cases} \tag{1.6}$$

An alternative fracture criterion in addition to that shown in Eq. (1.2) deals with the stress state near the tip of the crack. The stress intensity factor determines the "amplitude" of the crack tip stress for a certain geometry and loading case. Thus it may be concluded that a crack will grow when K reaches a critical value. This implies that a crack growth criterion can be formulated, where the stress intensity factor for a certain situation is compared to this critical value. The value of the stress intensity factor has to be calculated. The critical value has to be known from experimental measurements. It is called the *Fracture Toughness* and denoted as K_c.

$$K_I = K_{IC}\ ;\ \ K_{II} = K_{IIC}\ ;\ \ K_{III} = K_{IIIC} \tag{1.7}$$

As mentioned above plasticity occurs at the crack tip. As long as small scale yielding prevails, it is possible to apply Irwin plastic correction [2]. Using this correction a crack of length a is considered equivalent to an effective crack of length $a_e = a + r_y$ where r_y depends on K and the yield strength of the material.

1.2.2 Non linear fracture mechanics (NLFM)

LEFM is only valid as long as nonlinear material behavior is confined to a small region surrounding the crack tip. There are many materials that show elastic-plastic deformation for which the applicability of LEFM is impossible or at least suspicious. The plastic deformations influence the situation at the crack and in the body considerably. Thus,

special failure criteria need to be established to deal with this kind of problems. This task is pursued in *Elastic-plastic fracture mechanics* (*EPFM*).

A parameter characterizing the nonlinear behavior at the crack tip is the *J-integral*. Rice [3] presented a path-independent contour integral of analysis of cracks and showed that the value of this integral is equal to the energy release rate in a nonlinear elastic body that contains crack, i.e.: J=G. This relation has become a common technique to calculate stress-intensity factors in linear elastic fracture mechanics (LEFM). Hutchinson [5, 6] and also Rice and Rosengren[7] further showed that *J-integral* uniquely characterizes crack tip stresses and strains in nonlinear material. In other words *J-integral* plays the role of an intensity factor like K in the case of linear elastic material behavior.

Consider an arbitrary counter-clockwise path (Π) around the tip of a crack (see Figure 1.5). The *J-integral* is a given by

$$J = \int_{\Pi} \left(W\,dy - \overrightarrow{T}\frac{\partial \overrightarrow{u}}{\partial x} ds \right) \tag{1.8}$$

where W is the strain energy density defined as

$$W = \int \sigma_{ij} d\varepsilon_{ij} \tag{1.9}$$

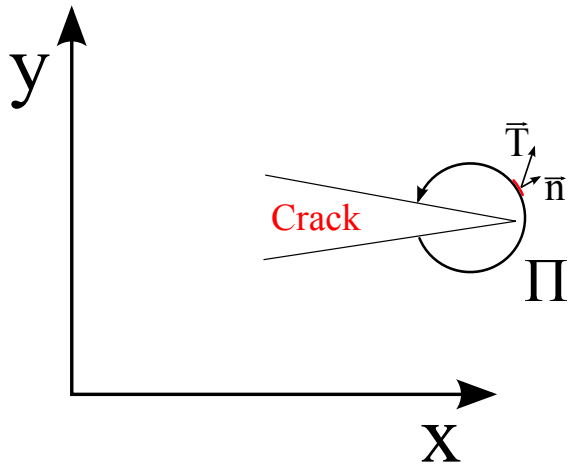

Figure 1.5: The J contour integral

Π is an arbitrary contour around the tip of the crack, $\overrightarrow{n}$ is the unit vector normal to Γ. $\vec{u}$ is the displacement field, $\overrightarrow{T}$ is the stress acting on the contour: $\overrightarrow{T} = \sigma \cdot \overrightarrow{n}$. Because of its path independence, the integral can be calculated in the remote field and characterizes also the near-tip situation.

1.3 Delamination/debonding problems

Currently, composite materials are used in a wide variety of high-performance applications. Delamination as a result of impact or a manufacturing defect can cause a significant reduction in the compressive load-carrying capacity of a structure. The stress

gradients that occur near geometric discontinuities such as ply drop-offs, stiffener terminations and flanges, bonded and bolted joints, and access holes promote delamination initiation, trigger intraply damage mechanisms, and may cause a significant loss of structural integrity. The fracture process in high performance composite laminates is quite complex, involving not only delamination, but also intralaminar damage mechanisms (e.g. transverse matrix cracking, fiber fracture).

Adhesive bonding of structural components is desirable in many instances because it eliminates the stress concentration factors caused by mechanical fastener holes. Also, weight and fabrication costs may be saved. Because composite material strength is significantly reduced when a hole is introduced, composites are extremely attractive candidates for adhesive bonding. The two disciplines, delamination of composite materials and debonding of adhesive joints, both essentially involve the separation of materials held together by polymer resins.

Adhesive joints usually fail by the initiation and propagation of flaws and, since the basic tenet of continuum fracture mechanics is that the strength of most real solids in governed by the presence of flaws, the application of such theories to adhesive joint failure has received considerable attention. The main aims of the various theories are to analyze mathematically the loads at which the flaws propagate and describe the manner in which they grow. For using bonded joints with confidence, a complete understanding of their behavior is necessary; it is thus necessary to provide parameters for characterizing crack growth independently of the geometry of the components. Different tests have been developed in order to ascertain values of various fracture parameters.

1.3.1 Mode I characterization

Mode I characterization of adhesive bonds is widespread for bonded joints and composites. The Double Cantilever Beam (DCB) is undeniably the most popular test geometry to assess the performance of an adhesive [23] or composite materials [24]. The DCB specimens consist of two cantilever arms with uniform width and thickness, bonded together by an adhesive layer or co-cured between adherends with a starter crack at one end. The first configuration is used for evaluating fracture toughness in adhesive joints, whereas the second one is used for characterizing the Fiber Reinforced Polymer Matrix Composites. The starter crack is created at one end of the specimen by placing a thin Teflon film at the midplane.

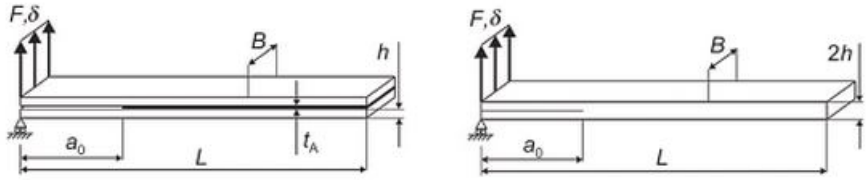

(a) (b)

Figure 1.6: Geometries of the bonded (a) and co-cured (b) DCB

a_0 is the initial crack length, t_A the adhesive thickness and L the specimen length. The load or a displacements is applied to provide a purely Mode I loading (opening

mode). A typical repeated loading-unloading response of a DCB specimen is plotted in Figure 1.7. The test is performed using a servohydraulic testing machine and the crack

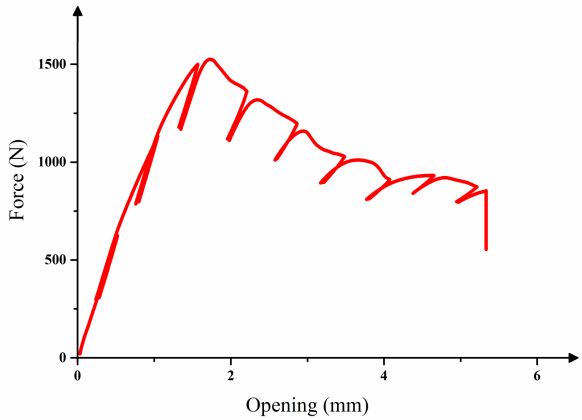

Figure 1.7: Load versus Opening in a DCB test

mouth opening displacement (Δ) is monitored using a clip-gage (Figure 1.8). Typically, loads are applied to the DCB via loading blocks or hinges adhesively bonded to the surface of the DCB.

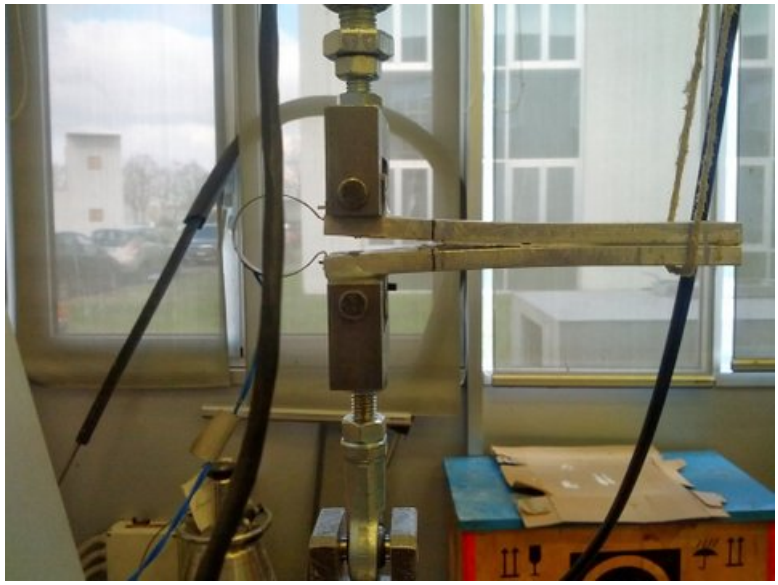

Figure 1.8: DCB test

The force increases almost linearly and reaches a peak in correspondence of which there is the onset crack. After the peak, the force decreases and the crack propagates. The several unloading/loadings are needed to make easier the strain energy release rate

calculation.

The strain energy release rate can be evaluated using the following equations [16]:

$$G = \frac{P^2}{2b}\frac{d\Psi}{da} = \frac{(Pa)^2}{bEI}\left(1 + \frac{1}{a\lambda_\sigma}\right)^2 \tag{1.10}$$

$$\Psi = \frac{\Delta}{P} = \frac{2\lambda_\sigma t}{E_a' b}\left[1 + 2\left(\lambda_\sigma a\right) + 2\left(\lambda_\sigma a\right)^2 + \frac{2}{3}2\left(\lambda_\sigma a\right)^3\right] \tag{1.11}$$

$$\lambda_\sigma^4 = \frac{6}{h^3 t}\frac{E_a^{'}}{E} \tag{1.12}$$

where a is the crack length, P is the load, E is the Young's modulus and I is the second moment of area of the beam section, $E_a^{'}$ is the plane strain Young's modulus of the adhesive and $d\Psi/da$ is the rate of change of compliance Ψ with respect to crack length.

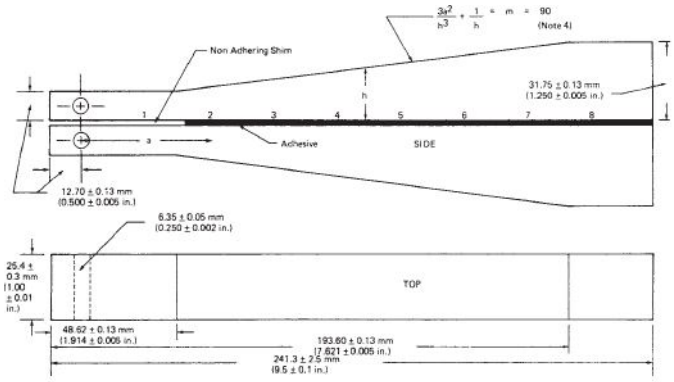

Figure 1.9: Contoured Double-Cantilever Beam Specimen[23]

Therefore, Eq. (1.10) allows one to determine the fracture energy of a test sample when the evolution of crack growth is known from Eq. (1.11), which is in turn fed by compliance values measured at given points during the test by unloading-reloading. The testing for fracture toughness of interface bonds obtained with conventional DCB specimens can require simultaneous measurements of critical load and crack length. The value of $d\Psi/da$ in (1.10) depends on the accuracy of the crack length measurements, which is generally a difficult task. The measurement of crack length can be avoided by contouring the DCB specimen, such that $d\Psi/da$ is a constant, and, in this case, the specimen in known as the contoured double cantilever beam (CDCB)(see Figure 1.9).

1.3.2 Mode II characterization

Fracture toughness under Mode II can be characterized with different popular tests: end-notched flexure (ENF), end-loaded split (ELS) and four-point end-notched flexure (4ENF). Between these, the ENF test is the most common for mode II fracture characterization of adhesively bonded joints and composites. The ENF is similar to DCB, although loading occurs by bending, induced by the loading cylinder at the specimen mid-length, while the edges are supported (Figure 1.10). The resulting load creates an

almost pure shear stress state at the crack tip, provided that the specimen is designed so that the adherends deform elastically.

However there are several difficulties, to be overcome in developing mode II tests, that cause a not good repeatability in G_{IIC} values. This issue mainly depends on unstably crack propagation and influence of friction caused by the relative sliding of two crack faces during the entire test. In fact a standardized fracture test for mode II does not exist. Since the beginning of 2009 a work item (WK22949) was initiated by the American Society for Testing and Materials (ASTM) with the scope to standardize a test method for mode II delaminations for UD fiber reinforced composites [25].

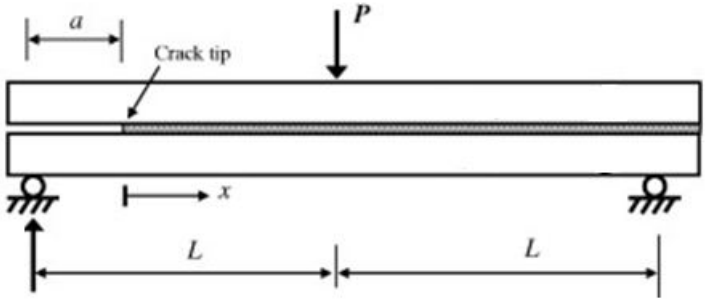

Figure 1.10: ENF test

1.3.3 Mixed-mode characterization

Although pure-mode testing is of fundamental interest, most structural applications of composite materials involve a combination of fracture modes, particularly Modes I and II. But, how these fracture modes combine to cause failure of the structure is not well established. Thus, there has long been interest in performing mixed-mode testing. Several mixed-mode test methods are presented and briefly discussed by J.H. Crews and J.R. Reeder [26, 27]. A major limitation of all of these test methods, however is the difficulty of determining the relative amounts of Mode I and Mode II fracture present for a given specimen configuration.

In the mid-1980s, Reeder and Crews developed at the NASA-Langley Research Center (Hampton, Va.) a much more suitable test method. They first published their work in a NASA Technical Memorandum in 1988, followed by a publication in the open journal literature in 1990. Refinements to the test fixture, essentially modifying it to the configuration standardized and in use today, were published in 1992. The governing standard, ASTM D6671, was first published in 2001 [28]. The corresponding Mixed Mode Bending (MMB) test fixture is shown in Fig. 1.11.

The concept is simple: the fixture simultaneously applies a direct combination of Mode I (Double Cantilever Beam) and Mode II (End-Notched Flexure) loadings. The hinges of the test specimen are clamped at the right end to both the fixture base and the loading beam. The left end of the specimen rests on a cylindrical support that is mounted in ball bearings so that it is free to rotate and, thus, not restrain lateral movement of the specimen. This support can be repositioned as required to achieve a desired support span length. The center bracket on the loading beam can be adjusted

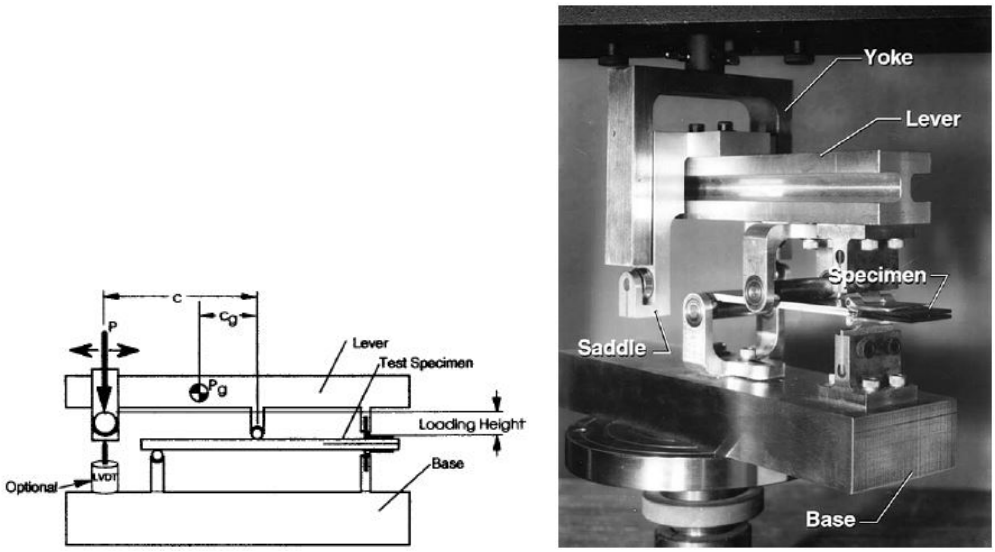

(a) (b)

Figure 1.11: Scheme (a) and fixture (b) of MMB test

to center the loading cylinder with respect to the support span. Then, by moving the saddle at the left end of the loading beam, various ratios of Mode I to Mode II can be induced in the test specimen. For example, if the saddle is positioned above the center-loading cylinder, pure Mode II is achieved. If the center-loading cylinder were positioned above the left support and the saddle moved to the left end of the beam, then pure Mode I could be achieved. Applied load versus load point deflection are recorded. Different values of interlaminar fracture toughness G_C, and mode mixture, $G_{II}/G_I + G_{II}$, are calculated using different critical loads reads from the load displacement curve. The critical loads, precisely defined in the standard, are however close to maximum applied load, when the crack starts growing.

The MMB test fixture is, today, the preferred method for quantifying the mixed-mode fracture toughness of composites, particularly now that ASTM D 6671 is available. The test specimen is simple and of a familiar form, and the test procedure is relatively straightforward. This test method has been successfully used to assess the toughness of adhesive joints.

1.4 Computational methods

An extensive use of adhesive joints or composite materials is permitted by the capability to simulate and predict the strength of these structures. So analytical methods are being progressively integrated or replaced by finite element analysis (FEA) for assess the resistance of complex structures in which delamination/debonding phenomena can occur.

1.4.1 Virtual crack closure technique (VCCT)

The energy release rates can be evaluated using the *virtual crack closure technique* (VCCT) proposed by Rybicki and Kanninen [8]. The VCCT is based on Irwin's assumption that when a crack extends by a small amount, the energy released in the process is equal to the work required to close the crack to its original length. The Mode I, Mode II, and Mode III energy release rates, G_I , G_{II} and G_{III} respectively, can then be computed from the nodal forces and displacements obtained from the solution of a finite element model. Indeed the VCCT derivates from the *crack closure method* (CCM) in which two-steps analysis in needed (see Figure 1.12).

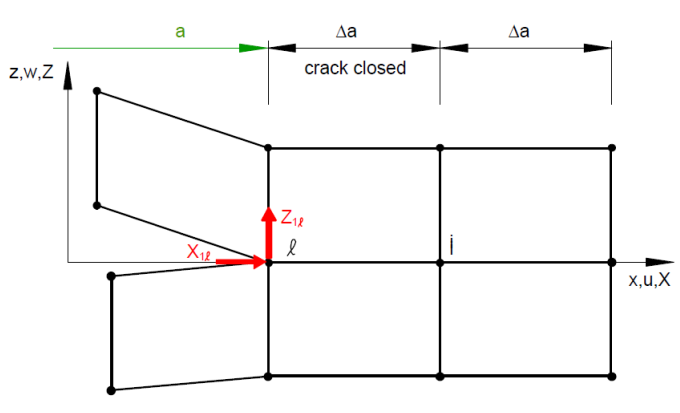

(a) First step

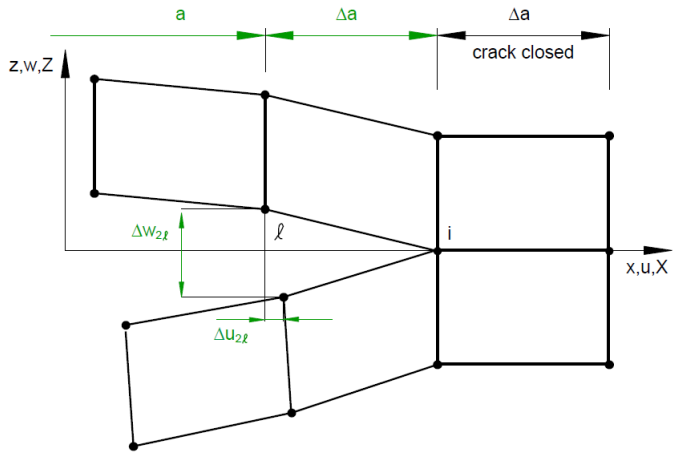

(b) Second step

Figure 1.12: Crack Closure Method

The energy ΔE released when the crack is extended by Δa from a to $a+\Delta a$ is identical to the energy required to close the crack between location l and i. Index "1"

denotes the first step depicted in Figure 1.12.a and index "2" the second step as shown in Figure 1.12.b. For a crack modeled with two-dimensional four nodes elements as shown in Figure 1.12 the work ΔE required to close the crack along one element side can be calculated as

$$\Delta E = \frac{1}{2}\left[X_{1l} \cdot \Delta u_{2l} + Z_{1l} \cdot \Delta w_{2l}\right] \tag{1.13}$$

where X_{1l} and Z_{1l} are the shear and opening forces at nodal point l to be closed and Δu_2 and Δw_2 are the differences in shear and opening nodal displacements at node l. The forces required to close the crack are identical to the forces acting on the upper and lower surfaces of the closed crack. The forces X_{1l} and Z_{1l} may be obtained from a first finite element analysis where the crack is closed. The displacements $\Delta u_2$and Δw_2 are obtained from a second finite element analysis where the crack has been extended to its full length $a+\Delta a$ as shown in Figure 1.12.b.

This approach is made computationally effective if the energy release rates is obtained from only one analysis. The additional assumption is that a crack extension of Δa from $a+\Delta a$ (node i) to $a+2\Delta a$ (node k) does not significantly alter the state at the crack tip (Figure 1.7).

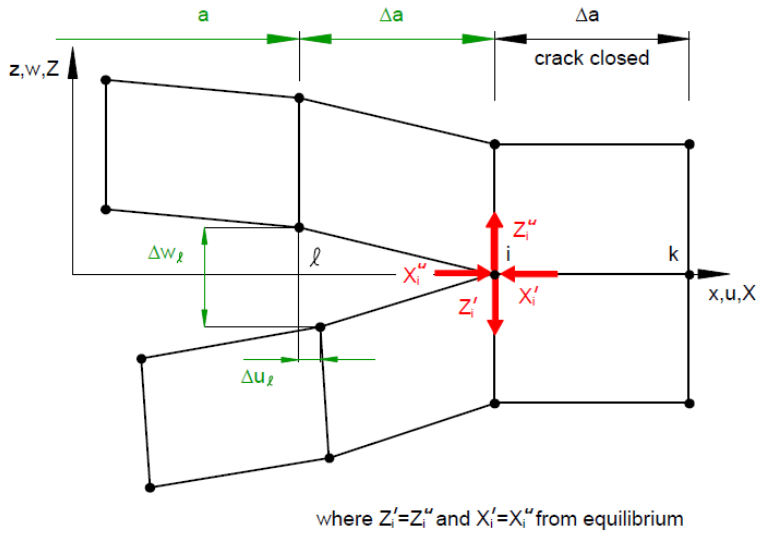

Figure 1.13: Modified Crack Closure Method

Therefore the displacements behind the crack tip at node i are approximately equal to the displacements behind the original crack tip at node l. Further, the energy ΔE released when the crack is extended by Δa from $a+\Delta a$ to $a+2\Delta a$ is identical to the energy required to close the crack between location i and k. For a crack modeled with two-dimensional, four-noded elements, as shown in Figure 1.13, the work ΔE required to close the crack along one element side therefore can be calculated as

$$\Delta E = \frac{1}{2}\left[X_i \cdot \Delta u_l + Z_i \cdot \Delta w_l\right] \tag{1.14}$$

where X_i and Z_i are the shear and opening forces at nodal point i and $\Delta u_l$and Δw_l are the shear and opening displacements at node l. Thus, forces and displacements required to calculate the energy ΔE to close the crack may be obtained from one single finite element analysis. The energy release rate $G{=}\Delta E/\Delta A$ (where A is the crack surface created) has to be separated into the individual mode components (G_I and G_{II}). The approach just presented for Two-Dimension finite element can be extended to Three-Dimensional cases in which the third dimension allows to calculate the distribution of the energy release rate along the delamination front and makes it possible to obtain G_{III}.

The virtual crack closure technique is implemented into several commercial finite element codes such as *Abaqus/Standard®*, *MD Nastran™*, *Marc™* and *ANSYS®*. For the automated delamination propagation analysis, the VCCT implementation in *Abaqus* requires the calculation of the energy release rate at the crack tip at the end of converged increment. Once the energy release rate exceeds the critical strain energy release rate, $G_{eq} \geq G_{eqC}$, the node at the crack tip is released in the following increment and so the crack propagates. It must be highlighted that G_{eqC} is based on the user-specified mixed-mode criterion ($G_{eqC} = f(G_{IC}, G_{IIC}, G_{IIIC})$) and the bond strength of the interface. For pure mode I, G_{eq} reduces to G_I and G_{eqC} is replaced by G_{IC} . Fracture analysis without crack propagation can also involve only the evaluation of energy release rate values, at a given crack length for a particular load. This involves that bonded region along the interface, should not debond under the application of load. In order to achieve this, the critical energy release rate are set at very high values.

Although valuable information concerning the onset and the stability of delamination can be obtained using the VCCT, its use in the simulation of delamination growth may require complex moving mesh techniques to advance the crack front when the local energy release rates reach a critical value. Furthermore, an initial delamination must be defined and, for certain geometries and load cases, the location of the delamination front might be difficult to determine.

1.4.2 The cohesive model

Some of the above difficulties explained at the end of the last paragraph can be overcome by using cohesive elements. The idea for the cohesive model is based on the consideration that infinite stresses at the crack tip are not realistic. Models to overcome this drawback have been introduced independentely by Dugdale [9] and Barenblatt [10]. Both authors divided the crack in two parts: one part of the crack surfaces, region I in Figure 1.14, is stress free, the other part, region II, is loaded by cohesive stresses that representing the material resistance to fracture.

In Dugdale's model the closure stress is the yield strength σ_y; in Barenblatt's model it represents the molecular force of cohesion and varies along the plastic zone (the stresses in the cohesive zone follow a prescribed distribution $\sigma(x)$, where x is the ligament coordinate). Most of the recently developed and proposed models are different from Barenblatt's model in that they define the traction acting on the ligament in dependency to the opening and not to the crack tip distance as Barenblatt did. Needleman was the first, who used the model for crack propagation analyses of ductile materials. More than ten years earlier, Hillerborg [11] already applied the cohesive model to brittle fracture of concrete using the finite element method for the first time, followed in the 80's by Petersson [12] and Carpinteri [13] amongst others. In between, the cohesive model has

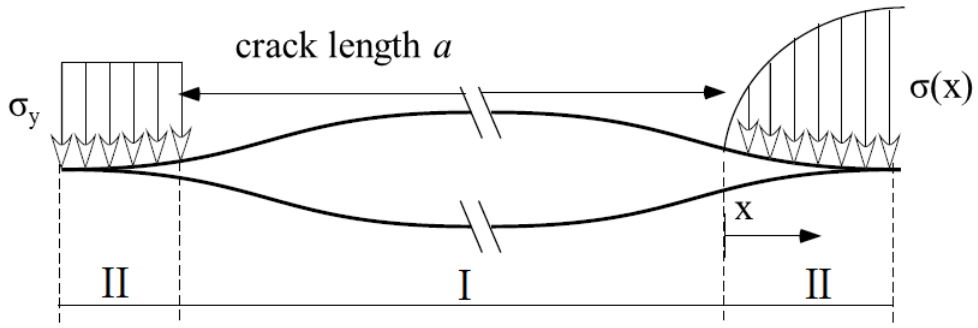

Figure 1.14: Dugdale (left) and Barenblatt (right) crack models

been applied to almost any kind of materials and to many different size and time scales from micro to macro and from impact to long term creep.

In FEM models the material separation and thus damage and failure of the structure is described by interface elements. Using this technique, the behavior of the material is split in two parts, the damage-free continuum with an arbitrary material law, and the cohesive interfaces between the continuum elements, which specify only the damage of the material. The interface elements open during loading and finally loose their stiffness such that the continuum elements are disconnected. For this reason the crack can propagate only along the element boundaries. If the crack propagation direction is not known in advance, the mesh generation has to make different crack paths possible. The central point of all cohesive zone models is the function that describes the interaction force between the two interfaces (crack faces). This law represents a real local material property that is independent of the external load. The so-called *cohesive law* or *separation law* is usually a relation between the boundary tractions σ and the separation $\delta_n = u_n^+ - u_n^-$ of the interfaces, i.e., the distance between the crack faces. Meanwhile, many proposal for cohesive laws exist in the literature, which differ according to various material and failure mechanism; for an overview see the review of Brocks et al. [14][15]. Some typical shapes are shown in Figure 1.15.

Initially, the stress increases with growing distance up to a maximum called the *cohesive strength* σ^0_{max} of the material. If the separation has reached a critical *decohesion length* δ_c, then the material is completely separated and no stress can be transmitted. Notice that the area under the stress-separation curve corresponds to the dissipated work during a material's separation - the specific fracture energy per surface area G_C as introduced by Griffith.

$$\Gamma = \int_0^{\delta_c} \sigma(\delta_n) d\delta_n = G_C \quad energy\ of\ separation \tag{1.15}$$

Thus, through (12) the relationship between cohesive zone model and classical fracture mechanics is established. The fracture process, as just described above, implies that the part modelled with cohesive elements is continuously under loading. In case of global unloading of the structure it is necessary to define a behavior of the cohesive elements under decreasing separation, which accounts for the irreversibility of the damage

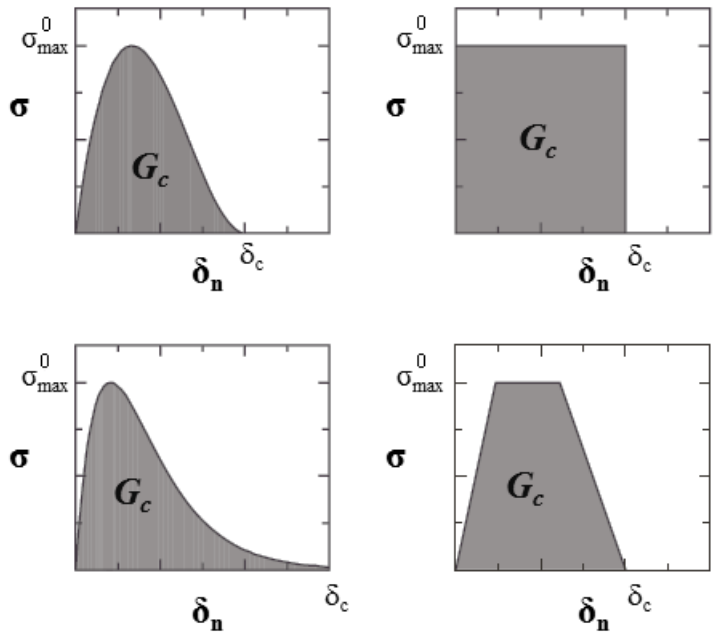

Figure 1.15: Typical forms of separation laws

process. Since damage evolution is a nonlinear process like inelastic deformation, the cohesive models are established in analogy to the principles of plasticity, but allowing for strain softening. The terms "loading" and "unloading" will be used in the sense of increasing or decreasing separation, respectively, as the tractions decrease also under increasing separation beyond maximum stress, σ_{max}. More generally, "unloading" is any change of the deformation direction by which the stress state removes from the limiting traction-separation curve. This definition also applies for shear separation. Two principle mechanisms depending on the material behavior have to be distinguished:

- **Ductile unloading** The mechanical work for producing damage is totally dissipated, the void growth and hence the inelastic separation are irreversible and any reduction of separation occurs purely elastically with unchanged elastic stiffness, as shown in Figure 1.16.a.

- **Cleavage unloading** The elastic stiffness of the material is reduced by damage, but the separation vanishes when the stresses decrease to zero, as shown in Figure 1.16.b.

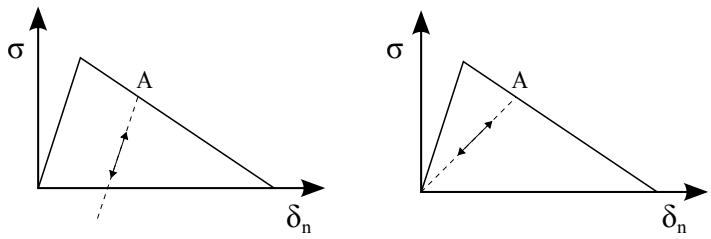

Figure 1.16: "Ductile" (a) and "Cleavage" (b) unloading behavior

Since the cohesive model is a phenomenological model, which can be used independently of the fracture mechanism, the two assumptions apply to different material behavior. The first one is valid only for ductile crack propagation. Brittle fracture, which is characterized by micro cracks, would not be modelled correctly with a permanent separation on unloading, since the micro cracks close entirely (without getting back their stiffness). In this case the second unloading mechanism should be used.

Cohesive zone model involves three important parameters: the critical separation δ_c, the cohesive strength σ_{max} and the cohesive energy Γ_0. It is usual to take $\Gamma_0$and $\sigma_{max}$to be the constitutive parameters in the research. The cohesive parameters of the traction separation law in each fracture mode should be determined for application of this method. Both experimental method and numerical method are used for determining the cohesive parameter. As above, the DCB test is used to obtain the opening Mode I fracture toughness G_{IC} of adhesives in bonded metal joints or fiber-reinforced composite materials. After determining the the opening fracture toughness G_{IC}, σ_{max} can be obtained by fitting the experimental force-opening curve with FEA results.

Chapter 2

Fatigue Crack Propagation

Fatigue fracture is one of the failure modes in engineering where crack initiates, propagates, and finally results in the failure of components under cyclic loading. It is widely spread in the fields of aerospace, transportation, machinery, and other industries, bringing on great economic loss and casualties every year. Therefore, it is extraordinary significant to avoid the occurrence of fatigue fracture. To do this, the factors influencing fatigue fracture have to be clear. In general, there are two approaches for fatigue lifetime prediction, which have been extensively used in the literature, namely, *stress-life* approach and *fatigue crack initiation/propagation* approach. In the stress-life approach, a series of tests under various loads are performed in order to obtain the plot of stress versus the number of cycles to failure, which is known as S-N curve or Wohler's curve. Theoretically speaking, at a fatigue threshold the structure has an infinite life. However, this is not the case for adhesively bonded joints and the threshold is usually specified at a certain number of cycles, for example, one million cycles. Instead in the second approach it is studied how the presence of a crack could reduce the life of a component or structure.

2.1 Theoretical framework

During fatigue of materials the following damage mechanism is observed. As a result of alternating micro-plastic deformations (dislocations, slip bands) first microcracks are formed on the surface or on microstructural inhomogeneities (inclusion, grain boundaries) in the interior. Only above a crack length of about 10 grain diameter do we call it a *crack*. Its behavior can now be described with methods of classical fracture mechanics. From a macroscopic view very small negligible plastic deformations occur and fatigue crack growth takes place in the K-controlled near-field, so that the LEFM is applicable (Figure 2.1). Many authors have neglected the crack initiation phase and based their lifetime analysis only on the crack propagation phase. The main reason for doing this is that the crack initiation phase is harder to deal with due to the difficulties associated with modelling the nucleation of a crack and the ability to monitor and detect the initiation phase.

Under alternating loads cracks may propagate stably although the stress intensity factor is far below the static fracture toughness. This phenomenon of subcritical crack propagation is called *fatigue crack growth.* Fatigue crack growth is the most common

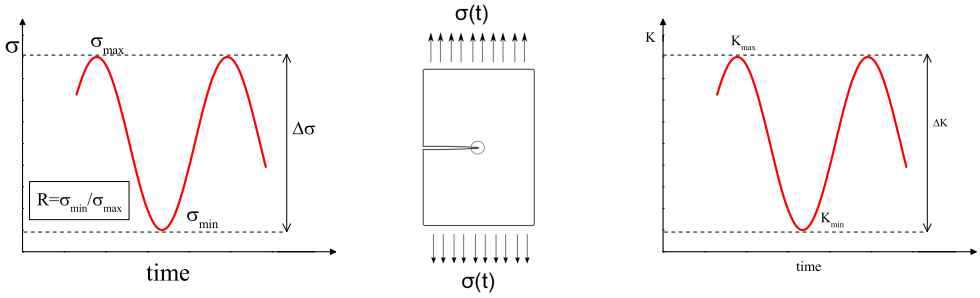

(a) (b) (c)

Figure 2.1: Relation between alternating load and stress intensity factors

cause of failure in mechanics, vehicles, aircraft and other constructions that are exposed to time-varying operating loads. Depending on their temporal course one can be distinguish between periodic (cyclic) or stochastic loads with constant or variable amplitude.

An important parameter in high-cycle fatigue is the rate of fatigue crack propagation that is determined by subjecting fatigue-cracked specimens, like the compact specimen used in fracture toughness testing, to constant-amplitude cyclic loading. The increase in crack length a is recorded along with the corresponding number of elapsed load cycles N during the test (see Figure 2.2).

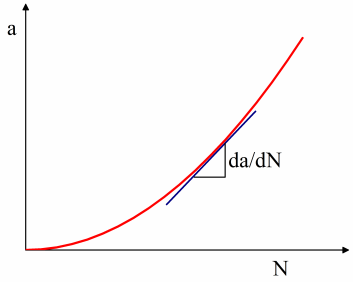

Figure 2.2: a - N trend

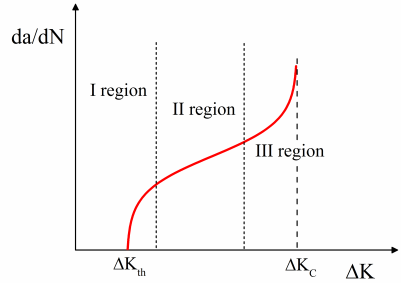

Figure 2.3: ΔK -da/dN trend

At cyclic loading both the external load, the stress distribution and the stress intensity factors are time-independent. In particular the stress intensity factor range is described by:

$$\Delta K = K_{max} - K_{min} = \Delta\sigma\sqrt{\pi a}\beta \tag{2.1}$$

where the $\Delta\sigma$ is the remote stress applied to the component and β depends on the crack length and the thickness of the component. The *crack growth velocity* or the *crack growth rate* is so defined as the ratio da/dN obtained by taking the derivative of the above crack length a - cycles N curve. Plotting the experimentally determined crack velocity da/dN on a double logarithmic scale as a function of cyclic stress intensity

factor ΔK, it can be obtained the *crack growth curve*. Its typical behavior is shown in figure 2.3. The fatigue crack propagation curve, which has a sigmoidal shape, has three different regions: (I) threshold region defined by fatigue threshold ΔK_{th} below which no crack growth takes place, (II) linear or steady state crack growth region, which can be well described by Paris' law [17, 18], and (III) fast or unstable crack growth region where catastrophic failure takes place when the fracture toughness $\Delta K_C = K_C(1 - R)$ is reached.

The Paris relation above mentioned has been extensively used in the literature to relate crack growth rate to the fracture parameter ΔK :

$$\frac{da}{dN} = C\Delta K^n \tag{2.2}$$

where C and n are empirical constants obtained by curve fitting of experimental data. The previous equation was modified and applied to fatigue delamination and debonding problems by Mostovoy and Ripling[19], using the strain energy release rate ΔG a*s* fracture parameter*,* to give:

$$\frac{da}{dN} = C\Delta G^n \tag{2.3}$$

The exponent n and the coefficient C depend on the material, temperature, stress ratio, R, and frequency [20, 21]. The behavior of the crack growth curve depends on the specific material and is influenced by manifold factors as micro structure, temperature, environment or R-ratio. With increasing R-ratio, the crack growth velocity da/dN and the threshold value ΔG_{th} commonly diminish.

An accurate and efficient prediction of fatigue crack growth allows to adopt the "*fail-safe design*" as design philosophy. So it is assumed that the component or structure may be safely operated even in the presence of some damage, that may grow up to a limit value before a structure replacement. In these structures a possible crack may grow in service, but will not reach critical size before its detection. Useful life is defined by a critical crack size (defined by the material toughness or other applicable criterion). Essential ingredients of these approaches are the knowledge of crack propagation as related with applied loading, and periodical inspections with a frequency ensuring that undetected damage in one inspection will not grow up to critical size before next inspection. So the progress of fatigue knowledge led to a *damage tolerant* approach where damage is considered unavoidable and measures are taken for its control along a component life cycle. This leads to weight savings but also to increased maintenance costs, particularly those related with periodical inspections. Actually a fail-safe design may not always possible and therefore it must be used the "*safe-life design*" approach. This design philosophy is instead based on the intention of avoiding fatigue crack initiation during the entire life time.

2.2 Mechanical characterizing fatigue crack propagation

As mentioned in the first chapter, debonding and delamination are quite similar process because they involve the separation of materials. The delamination occurs between two plies of a composite laminate and, once initiated, will grow under fatigue loading. During delamination growth, the structural loads may be redistributed such that another

delamination occurs in another location. The delamination may continue to grow and accumulate until a structural failure occurs, such as buckling or fiber failure. Additionally, the delamination may be arrested and the structure may maintain some integrity. Efforts to predict the delamination efforts and growth have focused on interlaminar fracture mechanics. The fracture mechanics prediction need the relation between strain energy relation rate G and delamination length a and Paris law parameters. For a initial delamination length, a strain energy relation rate values in known. From this value of G, the delamination growth rate , da/dN is obtained. For an incremental number of cycles, the increment in delamination length is determined. This gives a new value of G from the G-a relationship and a new value of da/dN is obtained. This continues until the delamination grows to a critical length, leading to a number of fatigue cycles to failure at the given load. This approach requires both computer modelling (FE analysis for obtaining G-a relationship) and experimental characterization under fatigue loading.

Delamination/debonding will grow under a combination of tension or peel, Mode I, and shear stresses, in plane (Mode II) and transverse (Mode III) shear, respectively. Test method have been developed for each of these modes along with some test that provide mixed-mode testing, such as the mixed-mode bending test. The more critical modes are mode I and mode II and these have received most attention in test development and material characterization. While most of the test-method developed has focused on static delamination growth, the importance on delamination fatigue has also been well covered by some researchers. The test specimens used to characterize delamination in fatigue are identical to those used for static characterization for all modes of fracture. In some instances when the delamination characterization is focused on threshold testing, the associated amplitudes may be small, particularly in mode II flexure tests. Therefore, it is often advisable to use thinner specimens than ones for the static tests so that amplitudes are higher. This, in turn, results in lower loads requiring appropriate load cells.

In [22] tests were conducted in load control mode and interrupted at complete separation of the adherends. Loads were applied with a sinusoidal wave at a fixed frequency (2-3 Hz). The length of the growing crack is monitored and the number of cycles (N) for each growth period was recorded. For computing the crack growth rate da/dN, the following equation is used (secant method):

$$\frac{da}{dN} = \frac{(a_{i+1} - a_i)}{(N_{i+1} - N_i)} \tag{2.4}$$

The corresponding values of the strain energy release rate were evaluated analytically using the expression 1.13. The slope and intercept obtained from the linear regression analysis were used to determine the exponent n and the coefficient C, from the Paris equation $da/dN = C\Delta G^n$. In order to monitor crack growth and measuring crack length as a function of number of cycles, several techniques have been used in the literature, for example, optical techniques such as video microscopic and magnification lenses, chirped fibre Bragg grating sensors, and ultrasonic technique. An other method consists in interrupting the test and loading up the specimen to the maximum force in order to keep the crack faces open and to measure the crack extension. The Double Cantilever Beam specimen has been widely used to measure the mode I interlaminar fracture toughness both statically and in fatigue. In the DCB specimen the initial crack is created placing at the mid-plane a non-adhesive insert, at one end prior to curing or consolidation. When the composites behavior has to be assessed, both 0°,

unidirectional and multidirectional layups can be used. However, if angle plies are used in a multidirectional lay-up these specimens may experience branching of the delamination away from the mid-plane through matrix crack in off-axis plies. If the delamination branches away from the mid-plane, a pure mode I will be not achived because of the coupling between extension and shear which may exists in the asymmetric sublaminates formed as the delamination grows.

In [22] the authors have proposed an approach for the prediction of fatigue crack propagation in a Tapered Single Lap Joint (Figure 2.4.b), made of relatively thick composite laminate adherends and bonded with an epoxy adhesive, using a crack growth law determined with DCB tests.

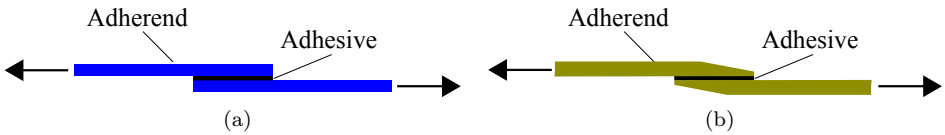

Figure 2.4: Single Lap Joints (a) Tapered Single Lap Joints (b)

The results were compared with experimental observations of the fatigue crack propagation during fatigue testing of some tapered single lap joints. It is very interesting to examine how a crack can propagate in a DCB with composite laminate adherends and subsequently how it reflects on the experimental data in a plot $\Delta G/\Delta G_{IC}$ versus da/dN.

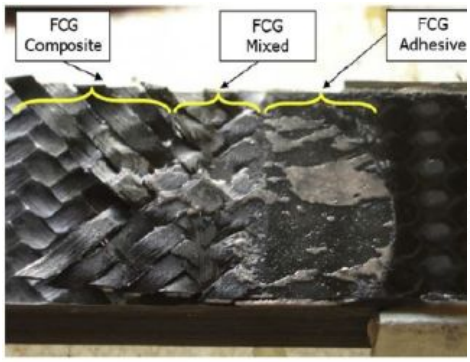

Figure 2.5: Fracture surface of an adherend after the FCG test [22]

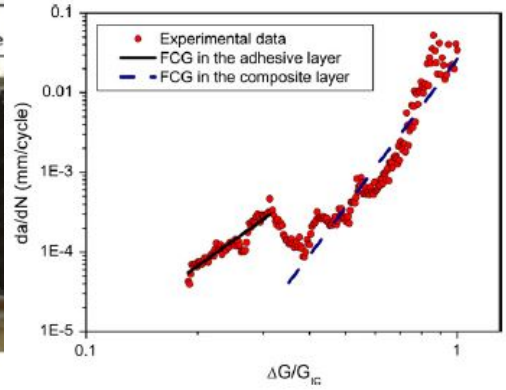

Figure 2.6: Results of the FCG test [22]

From the test results it clearly appears that the slope of the crack growth rate curve is not constant. Two distinct lines interpolating the experimental points can be identified by linear regression analysis. Fatigue crack propagation experiments on DCB specimens showed a complex crack propagation behaviour, with a crack path developing in the bondline and subsequently propagating in the adjacent layers. By visual inspection the fracture surface of the DCB specimens after testing (see Figure 2.5), it clearly appears that the first line of Figure 2.6 corresponds to FCG taking place at the interface between

the composite and the adhesive, and that the second line corresponds to cracks growing between the first (woven) and the second ply (unidirectional) of the composite laminate. So each region can be described with a Paris law. For predicting the fatigue crack growth of the tapered lap joint, the fatigue parameters (the exponent and the coefficient of the Paris law), corresponding to the crack propagation within the adhesive, have been used. This is a common approach to predict the fatigue behavior of defects in adhesive joints or composite parts using mode I fatigue parameter. In fact if full mixed-mode delamination characterization is not available the possibility of using the data from DCB test is an option. This is a conservative approach for delamination that have a high mode-II component because the mode II toughness of the composite is higher than the mode I.

For what concerns mode-II loading, there are several tests used to characterize fatigue delamination growth. These methods are mentioned in the previous chapter for the static characterization: ENF, ELS, 4ENF. These tests essentially use the same specimen type: it is the loading of this specimen that varies. For the ENF, the shear loading arises from three-point bending. The loading fixture uses rollers to support the specimen and to allow it to rotate freely. Delamination growth in this specimen is unstable and the fatigue delamination growth rate increases as the test progresses. For the 4ENF the specimen is placed in four-point bending with the delamination between the centre loading rollers, which are free to rotate about their centre line to allow for the asymmetric deflection of the specimen. The delamination growth is then stable and the fatigue delamination growth decreases as the fatigue test progresses. Delamination growth is also stable for certain delamination lengths with the ELS specimen, which is loaded as a cantilever beam.

Indeed the approach just described implies that a defect in the adhesive joint or in a composite part already exists. The other important approach for characterizing the fatigue delamination deals with the delamination initiation. Both methods are needed to accurately predict the structural integrity of a component. Many researchers focus their work in the first phase spent in the nucleation of a crack. This phase is not negligible since the fraction of life for crack initiation represents a significant part of the joint fatigue life. For example in single lap bonded joints (see a SLJ in Figure 2.4.a), this fraction can range from a minimum of about 20% up to more than 70% depending, mainly, on overlap length and stress level [37]. Similar results are available in the literature for bonded joints made from metallic or composite adherends [30, 32, 33, 36, 31]. These results clearly indicate that neglecting the nucleation phase and considering the fatigue life of the joint entirely spent in crack propagation, as done by some of the methodologies available for the life prediction of bonded joints, could result in too conservative assessment of the fatigue life of the joints.

Monitoring and detecting crack initiation has been performed in the literature using back-face strain. Back-face strain has extensively been used in the literature to monitor crack initiation in adhesively bonded joints [39, 40, 41, 42]. Zhang et al. [38] developed a back-face strain technique to detect fatigue crack initiation in SLJs. Because of its simple geometry, the single lap joint has been widely used to asses the mechanical behavior of adhesive joints. When a single lap joint is loaded with two parallel forces, a moments devolps, which causes the joint to rotate as shown in Figure 2.7.

The joint rotation produces a bending deformation in the adjoining beams. The deformation of the beam is the most severe ate the end of the overlap, where two strain gauges are placed on the “backface” of the beam. When a crack appears at one of the end,

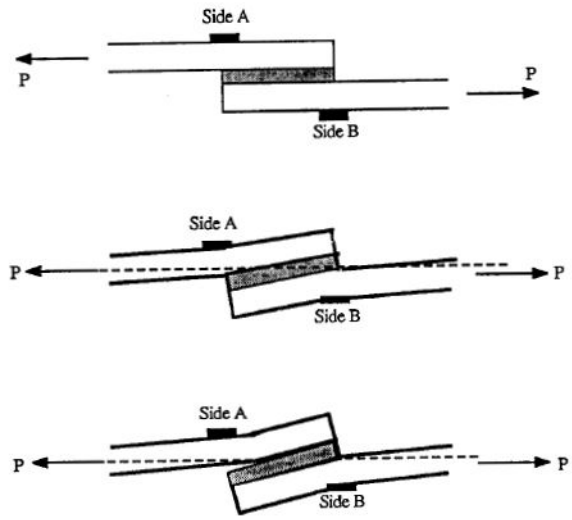

Figure 2.7: SLJ deformation during a fatigue test [38]

e.g., at side A, it relaxed the deformation of the beam locally, moving the location of the maximum strain to a point close to the crack tip. Consequently, the strain reading at the strain gauge placed at side A decreases as soon as the crack is initiated. The essence of the backface strain techniques is that downfall of the backface strain from one of the two gauges could be used as an indicator for fatigue crack initiation during fatigue laoding. From experimental measurements, it has been found that fatigue crack initiation lives at different stresses have greater proportion of the total fatigue life as the stress decreased. However, Crocombe et al. [43] investigated the technique in more detail and showed that the back face strain response was highly dependent on its location. The research concluded that ideally the SG position should be inside the overlap because here it will produce the largest change in back face strain with damage.

Ishii et al. [45] and Zeng and Sun [46] also used video-microscopy to monitor fatigue damage in adhesive joints.

Chirped fibre Bragg grating sensors have been used by Capell et al. [44] and embedded within GFRP substrates to monitor disbond initiation and growth in a GFRP/Al SLJ. It was found that disbond initiation and growth between the substrates during fatigue cycling caused peaks or dips in the reflection spectra from the chirped fibre Bragg grating sensor.

2.3 CZM for fatigue crack propagation

Numerical simulation offers nowadays outstanding possibilities for the prediction of the crack propagation process in debonding problems and has become an indispensable tool in performing this task. The mechanisms involved in both debonding and delamination are highly similar, as are the prediction methods developed to deal with them.

The Cohesive Zone Model has been receiving increasing attention in this direction. In the CZM approach the interfaces, along which delaminations are expected to grow, are

modelled using cohesive zone elements. These elements are not linear elastic, but follow a prescribed traction-displacement relation. Often some kind of damage parameter is used to progressively reduce the stiffness, simulating damage growth within the element. Thus the constitutive behavior of the cohesive element is generally defined as:

$$\begin{aligned} \sigma &= K^0\delta \quad if \quad 0 \leq \delta \leq \delta^0 \\ \sigma &= (1-D)K^0\delta \quad if \quad \delta^0 \leq \delta \leq \delta^c \\ \sigma &= 0 \quad if \quad \delta^c \leq \delta \end{aligned} \tag{2.5}$$

where δ is the current value of the relative displacement of the faces of the cohesive element, D is the damage parameter, δ^0 is the displacement at the onset of softening of the element, δ^c is the displacement at failure, K^0 is the stiffness and σ is the traction. Several attempts to establish the CZM approach to fatigue have been made.

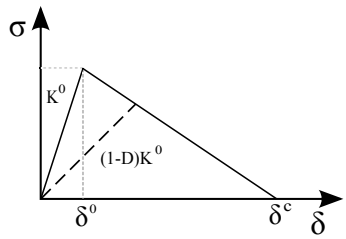

Figure 2.8: Bi-linear constitutive law

2.3.1 Low-cycle fatigue

According to Lemaitre et al. (1999), low-cycle fatigue occurs when the damage is localized in domains of stress concentrations but it can be measured and evaluated at the mesoscale. The number of cycles to failure is smaller than 10^4. Low-cycle fatigue models account for fatigue damage evolution on a cycle by cycle analysis defining, in the majority of the models, an evolution of the damage variables during the unloading path. Within the context of the cohesive zone model, there are several models that extend cohesive laws that were derived for monotonic loading into forms suitable for cyclic loading.

Foulk et al. [47] simulated the interface failure under cyclic loading by adding an unloading condition to softening CZM. Unloading and subsequent reloading follow the same path, and consequently the traction-separation behavior stabilizes without further progress in material separation. De Andrés et al. [48] took a similar approach, but added an unloading condition and a cycle dependent damage variable defined as:

$$D = \frac{\phi(\delta_{max})}{G_c} \tag{2.6}$$

where δ_{max}, $\Phi(\delta_{max})$, and G_C are the maximum attained separation, corresponding dissipated energy to δ_{max}, and fracture energy, respectively. D ranges from 0 to 1, with these limits referring to an uncracked solid and a fully formed new fracture surface.

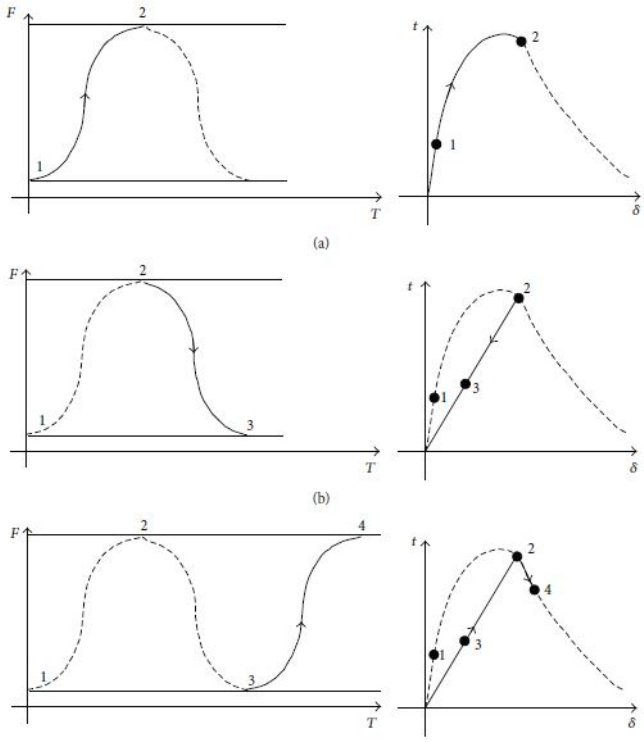

Figure 2.9: Schematic representation of the process of damage accumulation during cyclic loading [49]

A point on the cohesive zone at the crack tip is considered for CZM to account for accumulated damage process as depicted in Figure 2.9.

Suppose that the forward of the loading curve leads to the increasing separation of cohesive surfaces. Upon unloading, the cohesive zone cannot close completely due to plastic deformation of the surrounding materials. Then the damage locus is reached at the forward part of subsequent loading and further damage accumulates. After sufficient loading cycles, material in the cohesive zone will degenerate completely and form new fracture surfaces, predicating the propagation of the fatigue crack. The crack fronts of aluminum shafts subjected to axial loading have been predicted using this partial unloading-reloading configuration. However, in [48] the state of the specimen and thus the evolution of D was not an outcome of a cycle-by-cycle computation of FCG and an extrapolation scheme was used to obtain estimates of D in dependence of number of cycles. This allows the damage length to be evaluated at a limited set of cycle numbers, without the need to find the intermediate behavior following in detail every loading cycle. A cohesive law with an unloading-loading hysteresis behavior was introduced by Nguyen et al. [50] and Yang et al. [51]. Linear unloading combined with nonlinear reloading made it possible to take dissipative mechanism into account such as frictional interactions between asperities as well as crystallographic slip. Material degradation can accumulate below the limiting curve of the cohesive law for monotonic loading (the "damage locus") prior to failure due to the fact that unloading and reloading do not follow

the same path, but show a hysteresis and thus dissipated energy (see Figure 2.10).

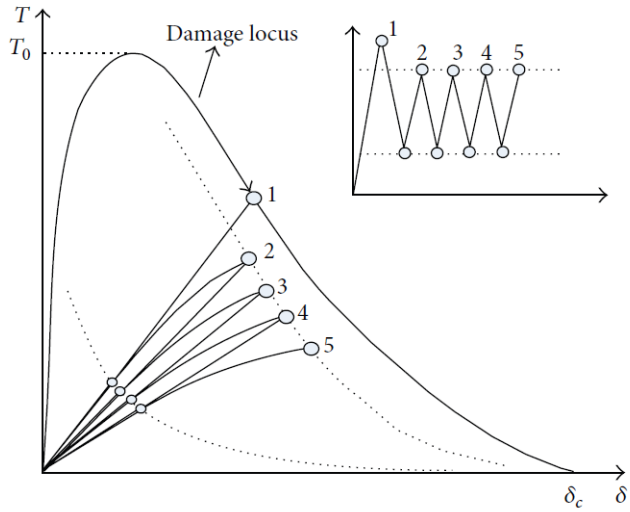

Figure 2.10: Cohesive law with accumulating damage under cyclic loading

The applied (global) loading range determines the upper and lower loading levels in the cohesive elements. Since damage evolution is a nonlinear process for inelastic deformation, CZM can be established in analogy to the principles of plasticity but allowing for strain softening. The well-known characteristics of typical elastic-plastic damage evolution laws include the following: (i) damage begins to accumulate once a deformation measure, accumulated or current, is greater than a critical magnitude; (ii) the increment of damage is related to the increment of deformation as weighted by the current load level; (iii) there exists an endurance limit which is a stress level below which cyclic loading can proceed infinitely without failure. Based on this consideration, Roe and Siegmund [52] proposed the evolution equation for damage of the cohesive zone under cyclic sub-critical loads. Its increment form is written as

$$\Delta D_c = \frac{\mid \Delta\delta \mid}{\delta_\Sigma} \left[\frac{T}{\sigma_{max}} - \frac{\sigma_f}{\sigma_{max,0}} \right] H\left(\delta_n - \delta_n^0\right) \tag{2.7}$$

with

$$\Delta D_c \geq 0, \tag{2.8}$$

where $\Delta\delta$ and T are the effective cohesive zone quantities, with H designating the Heaviside function. In the expression, two additional parameters are introduced, that is, the cohesive zone endurance limit σ_f and the accumulated cohesive length δ_Σ, which determines the amount of accumulated effective separation necessary to fail the cohesive zone. δ_Σ is a multiple of the cohesive length δ_n^0, which is the material separation across the crack surfaces in the cohesive zone corresponding to the cohesive strength under normal loading. The magnitude of the incremental damage is then dependent on the two additional material parameters and the proportional to the scaled and normalized incremental resultant separation, $\mid \Delta\delta \mid / \delta_\Sigma$, weighted by a measure of current traction

reduced by the endurance limit. Then the damage is translated as the degradation of the cohesive properties in the CZM constitutive relation by

$$\begin{aligned} \sigma_{max} &= \sigma^0_{max}(1-D) \\ \tau_{max} &= \tau^0_{max}(1-D) \end{aligned} \tag{2.9}$$

where σ_{max} and τ_{max} are the current cohesive normal and tangential strengths used to substitute the initial ones. The unloading and reloading path in the investigation follow a linear relationship with a slop equal to that of the current traction-separation curve at zero separation. In the current model, the accumulated damage has been accounted for explicitly and incrementally. In almost all of these references, the fatigue damage accumulation is accounted for in a cycle-by-cycle analysis. For high-cycle fatigue, where the number of cycles is larger than 10^6, a cycle-by-cycle analysis would be computationally intractable.

2.3.2 High-cycle fatigue

According to Lemaitre et al. (1999), high-cycle fatigue occurs when the damage is localized at the microscale as a few micro-cracks. Since a cycle-by-cycle analysis is impractical another strategy, called cycle-jump strategy, is usually adopted: damage evolution is extrapolated over a given number of cycles. In this way the computation of the whole load history is reduced to a certain number of cycles that are simulated blockwise each step. High-cycle fatigue models require the definition of the relation between the damage variable and the number of cycles as an input for the cycle-jump strategy (Figure 2.11). This means also that numerically applied loads and numerically computed displacements are envelopes of the cyclic curves.

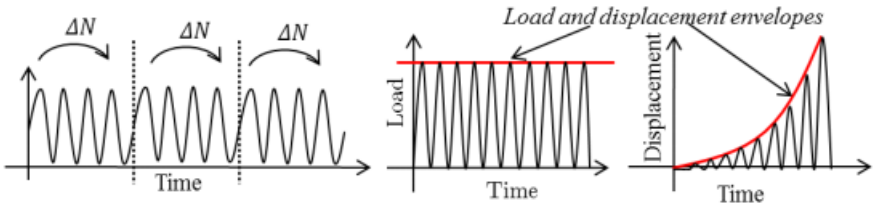

Figure 2.11: Cycle Jump strategy (left), load and displacement envelopes (centre and right)

The majority of the models relating the damage variable to the number of cycles use a phenomenological law established a priori and formulated as a function of the number of cycles. The damage evolution law is a function of several parameters that have to be adjusted to calibrate the numerical model with experimental results, usually by trial and error. An example of these models is the Peerling's law [53] used to predict fatigue in metals. Peerling's law has been adapted successfully to simulate high-cycle fatigue by means of an irreversible cohesive zone model (Robinson et al. [54]). In [54] it was proposed a damage parameter that was split into two parts: one for the static portion of delamination growth and one for the fatigue portion. Robinson et al. simulated the fatigue behavior by numerically applying a constant load equal to the maximum of the

fatigue load, and treating the damage parameter and displacement as dependent on pseudo-time, as represented by the number of cycles. The static damage can be written in terms of the displacement as:

$$D_s = \frac{\delta^c}{\delta_n} \cdot \frac{\delta - \delta^0}{\delta^c - \delta^0} \quad for \;\; \delta^0 < \delta < \delta^c \tag{2.10}$$

with D_s=*0* when δ is below δ^0 and D_s=*1* otherwise. The change in static damage between N cycles and N+ΔN can then be computed from the respective displacements and equation (2.25) as

$$\Delta D_s = \frac{\delta^0 \delta^c}{\delta^c - \delta^0} \left(\frac{1}{\delta(N)} - \frac{1}{\delta(n + \Delta N)} \right) \tag{2.11}$$

The fatigue damage is introduced in the following way, which was first proposed by Peerlings [53] following a modified version by Paas [55]

$$\dot{D}_f = \frac{\partial D_f}{\partial t} = A e^{\lambda D} \left(\frac{\delta}{\delta^c} \right)^{\beta} \frac{\dot{\delta(t)}}{\delta^c} \tag{2.12}$$

where β, λ and A are parameters which have to be determined so that the resulting crack growth is in agreement with the experimentally determined Paris law and δ/δ^c is a normalized displacement. Using this damage rate, fatigue damage can occur when the initial damage is zero and thus a crack can grow even in an initially undamaged interface. The fatigue damage after a number of cycles ΔN has elapsed can be found by integrating the fatigue damage rate over the respective number of cycles. This integration is performed numerically. A constant μ with $0 \leq \mu \leq 1$ is found, so that

$$\Delta D_f = \int_N^{N+\Delta N} \frac{A}{1+\beta} e^{\lambda D(N)} \left(\frac{\delta_n(N)}{\delta_c} \right) dN = \Delta N \frac{\partial D_f(D_\mu, \delta_\mu)}{\partial N}, \tag{2.13}$$

$$\begin{aligned} D_\mu &= (1-\mu) D(N) + \mu D(N + \Delta N) \\ \delta_\mu &= (1-\mu) \delta(N) + \mu \delta(N + \Delta N) \end{aligned} \tag{2.14}$$

A value for μ of 0.7 was used. Combining equations (2.28) and (2.29), the damage evolution with respect to a cycle jump ΔN can thus be expressed as

$$D(N + \Delta N) = D(N) + \Delta D_s + \Delta D_f \tag{2.15}$$

This implicit formulation for $D(N + \Delta N)$ is approximated using a Newton-Raphson algorithm.

In the model proposed by Robinson et al. a new set of parameters has to be determined for each mode-mix ratio in a manner similar to the way Blanco et al. [56] related the Paris parameters C and n to the mode-mix. Tumino and Cappello [57] modified this model by relating the model parameters A and β with the mode-mix. Robinson et al. [54], Muñoz et al. [58], and Tumino and Cappello [57] all present comparisons between predictions produced with (derivatives of) the model proposed in [54] and experimental data. In each case the same dataset is used [60] and good agreement is shown. However this dataset was also used to find the required input parameters of the model. Thus the

demonstrated agreement between the model and the experimental data is tautological. Until the model is compared to a new dataset it cannot be considered to be validated.

A different split parameter was proposed by Harper and Hallet [59]. In this model the static component of the damage parameter is defined as:

$$D_s(\delta) = \frac{\delta - \delta^0}{\delta^c - \delta^0} \tag{2.16}$$

For the fatigue component, the model of Blanco et al. [56] is used to predict the delamination growth rate. From this growth rate the matching fatigue damage zone size and fatigue damage growth rate are calculated. The fatigue component of the damage parameter follows from the fatigue damage growth rate. Such a linkage between CZM and fracture mechanics was originally proposed by Turon et al. [61]. The SERR required as input for the Blanco model is calculated by integrating the traction–displacement curve of the cohesive element. Essentially, the model proposed by Harper and Hallet provides a more complex method of calculating the SERR, but is otherwise not much different from the model proposed by Blanco et al. Harper and Hallet present a comparison between their model and experimental data reported by Asp et al. [60]. However this data was also used to find the empirical parameters in the Blanco model (and thus in the Harper– Hallet model). Therefore this comparison cannot be regarded as a validation of the Harper–Hallet model, and one must conclude a comparison with new experimental data remains necessary.

Khoramishad et al. [62] proposed a damage parameter based on the maximum strain, according to:

$$\frac{\Delta D}{\Delta N} = \begin{cases} \zeta \left(\varepsilon_{max} - \varepsilon_{th}\right)^{\kappa} & \varepsilon_{max} > \varepsilon_{th} \\ 0 & \varepsilon_{max} \leq \varepsilon_{th} \end{cases} \tag{2.17}$$

$$\varepsilon_{max} = \frac{\varepsilon_n}{2} + \sqrt{\left(\frac{\varepsilon_n}{2}\right)^2 + \left(\frac{\varepsilon_s}{2}\right)^2} \tag{2.18}$$

where ϵ_{max} is the maximum principal strain in the cohesive element, ϵ_{th} is the threshold strain, below which no fatigue damage occurs, ϵ_n is the normal component of the strain, ϵ_s is the shear component of the strain, ζ and κ are material constants. The parameters ζ, κ *and* ϵ_{th} need to be calibrated against the experimental tests. The fatigue damage was modelled by degrading the bi-linear traction–separation response. As shown in Figure **??**, the fatigue damage variable was used to determine the degraded traction–separation response whereas the static damage parameter was utilized to define the material status within that traction– separation response.

Khoramishad et al. produced a load-life diagram and predicted the back-face strain at the point where a strain gauge was applied during the experiments. The experimental and numerical results showed good agreement.

2.3.3 Concluding remarks on the CZM

The CZM approach suffers from the same shortcomings, i.e. a lack of grounding in an understanding of the physics underlying the delamination process. This is seen both in the cohesive relation itself and in the damage parameter formulations. The loci of initiation and propagation are usually determined by means of a phenomenological criterion based on the pure modes I and II values. Summarizing, to correctly define the

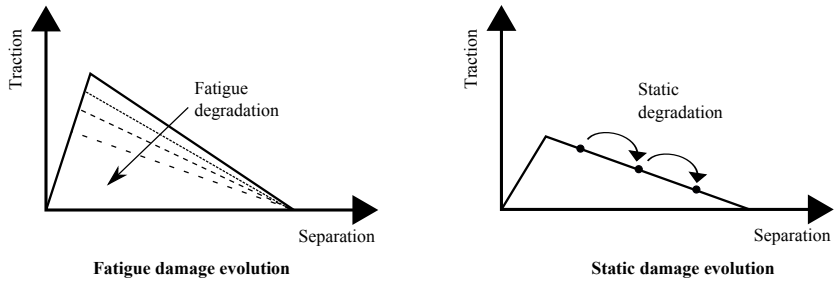

Figure 2.12: Fatigue and static degradation of cohesive element properties

cohesive zone a number of parameters need to be determined. Of these parameters only the values of G_{IC} are determined experimentally, the others are chosen based on numerical considerations. Even the G_C values may be treated as fitting parameters however. The damage parameter likewise requires a number of empirically determined parameters of which the physical significance is not completely clear. The main advantages of the CZM approach are that it avoids the need for re-meshing along a pre-defined crack path, and can include the initiation phase in the model [58, 63, 62]. In the papers discussed above the delamination size was always one-dimensional, implying a straight delamination front. The advantageous behavior of the CZM would be more visible in the investigation of delamination growth that is non-uniform along the delamination front.

In this context, this Phd thesis presents the developments of the model proposed by Moroni and Pirondi [65, 66].

Chapter 3

Development of a CZM for two-dimensional fatigue debonding of adhesive joints

In this chapter, the fatigue delamination/debonding of composite assemblies under Mode I, Mode II and mixed-Mode I/II loading conditions is simulated by the cohesive zone model proposed by Moroni and Pirondi [65, 66, 67]. The method has been validated using the Virtual Crack Closure Technique (VCCT) embedded in the software Abaqus.

3.1 Model theory

3.1.1 Cohesive law accounting for fatigue damage

The model presented in [65, 66, 67] started from the framework proposed by Turon et al. [61]. In the approach presented by Turon, the evolution of the damage variable associated with cyclic loading is derived from a Fracture Mechanics description of the fatigue crack growth rate. Therefore, the proposed model links fracture mechanics to damage mechanics. Considering a representative surface element (RSE) (represented in the simulation by a cohesive element section) with a nominal surface equal to A_e, the accumulated damage can be related to the damage area due to micro voids or crack (A_d) (see Figure 3.1) according to Lemaitre [35]:

$$D = \frac{A_d}{A_e} \tag{3.1}$$

In Turon et al. D is a related to the ratio between the energy dissipated during the damage process and the critical energy release rate, G_c. Instead in this work, D acts directly on stiffness, like in Lemaitre.

Referring to a mode I loading case, when the opening is relatively small the cohesive element behaves linearly; this happens until a given value of displacement, δ_{22}^0 (or equivalently until a certain value of stress σ_{22max}^0). This initial step is characterized by a stiffness K_{22}^0, that remains constant until δ_{22}^0. Beyond this limit the stiffness is

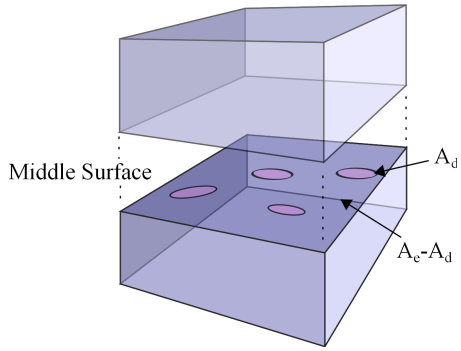

Figure 3.1: Nominal and Damaged Area in a Representative Surface Element

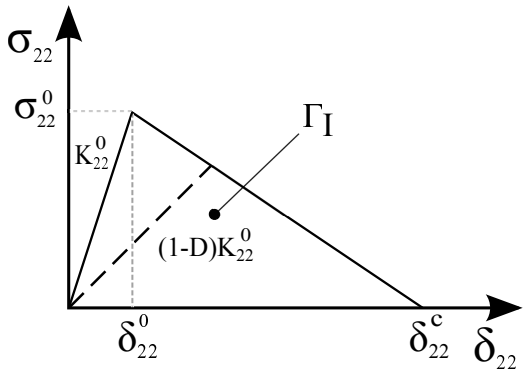

Figure 3.2: Traction separation law in Mode I loading

progressively reduced by D, until the final fracture in δ_{22}^c where the two surfaces are completely separated. Between δ_{22}^0 and δ_{22}^c the stiffness K_{22} can be computed as

$$K_{22} = K_{22,0}\,(1 - D) \tag{3.2}$$

As mentioned in the first chapter, the area Γ_1 underling the cohesive law is the energy to make the defect grow of an area equal to the element cross-section and it is therefore representative of the fracture toughness, G_{IC}.

$$\Gamma_I = \int_0^{\delta_c} \sigma_{22} d\delta_{22} \tag{3.3}$$

In the monotonic case, the damage variable D can be written as a function of the opening (δ_{22}) and of the damage initiation and critical opening (respectively $\delta_{22,0}$ and $\delta_{22,c}$):

$$D = \frac{\delta_{22,c}\,(\delta_{22} - \delta_{22,0})}{\delta_{22}\,(\delta_{22,c} - \delta_{22,0})} \tag{3.4}$$

When the element is unloaded, the damage cannot be healed, therefore, looking at Figure 3.2, the unloading and subsequent loadings will follow the dashed line, until a

further damage is attained. This simple model is able to describe the monotonic damage in case of mode I loading.

Considering the entire cohesive layer, the crack extension (A) can be computed as the sum of damaged areas of all the cohesive elements (A_d) [61]:

$$A = \Sigma A_d \tag{3.5}$$

When the fatigue damage is considered, from the previous equation, the crack growth (dA) can be written as a function of the increment of the damage area of all the cohesive elements (dA_d), therefore:

$$dA = \Sigma dA_d \tag{3.6}$$

However the damage increment would not concern the whole cohesive layer, but it will be concentrated in a relatively small process zone close to the crack tip, A_{CZ}. In order to estimate the size of ACZ, analytical relationships can be found in the literature (Harper and Hallett, 2008 [68]), where the size per unit thickness is defined as the distance from the crack tip to the point where σ^0_{22max} is attained. In this work, different definition and evaluation method are proposed: A_{CZ} corresponds to the sum of the nominal sections of the cohesive elements where the difference in opening between the maximum and minimum load of the fatigue cycle, $\Delta\delta_{22} = \delta_{22,max} - \delta_{22,min}$, is higher than a threshold value $\Delta\delta^{th}_{22}$. The value $\Delta\delta^{th}_{22}$ is supposed to be the highest value of $\Delta\delta_{22}$ in the cohesive layer when ΔG in the simulation equals ΔG_{th} experimentally obtained by FCG tests. It has to be underlined that in this way FCG may take place even at $\delta_{22,max} \leq \delta_{22,0}$, which is a condition that should be accounted for since $\delta_{22,0}$ results from the calibration of cohesive zone on fracture tests and may not be representative of a threshold for FCG. The process zone size A_{CZ} has therefore to be evaluated by finite element analysis while performing the FCG simulation but, on the other hand, does not need to be assumed from a theoretical model. The Eq. (3.6) can be therefore rewritten as

$$dA = \sum_{i \epsilon A_{CZ}} dA^i_d \tag{3.7}$$

where only the elements lying in the process zone, A_{CZ}, are considered. In order to represent the crack growth due to fatigue (dA/dN), the local damage of the cohesive elements (D) has to be related to the number of cycles (N). This is done using the equation

$$\frac{dD}{dN} = \frac{dD}{dA_d}\frac{dA_d}{dN} \tag{3.8}$$

The fist part of Eq. 3.8 can be easily obtained deriving Eq. (3.1). Therefore

$$\frac{dD}{dA_d} = \frac{1}{A_e} \tag{3.9}$$

The process to obtain the second part is quite more complicated: the derivative of Eq. (3.7) with respect to the number of cycles is

$$\frac{dA}{dN} = \sum_{i \epsilon A_{CZ}} \frac{dA^i_d}{dN} \tag{3.10}$$

At this point an assumption is introduced: the increment of damage per cycle is supposed to be the same for all the elements lying in the process zone. Therefore the value dA_d/dN is assumed to be the average value of the damaged area growth rate dA_d^i/dN for all of the elements in the process zone.

Hence the crack growth rate can be rewritten as [61]

$$\frac{dA}{dN} = \sum_{i \epsilon A_{CZ}} \frac{dA_d^i}{dN} = n_{CZ} \frac{dA_d}{dN} \tag{3.11}$$

where n_{cz} is the A_{CZ}. n_{cz} can be written as the ratio between the process zone extension (A_{CZ}) and the nominal cross section area (A_e) leading to the equation

$$\frac{dA}{dN} = \frac{A_{CZ}}{A_e} \frac{dA_d}{dN} \tag{3.12}$$

The second part of Eq. (3.8) can be therefore written as:

$$\frac{dA_d}{dN} = \frac{dA}{dN} \frac{A_e}{A_{CZ}} \tag{3.13}$$

The crack growth rate can be finally expressed as a function of the applied strain energy release rate, in the simplest version using Eq. (2.3)

$$\frac{dD}{dN} = \frac{1}{A_{CZ}} C \Delta G^n \tag{3.14}$$

3.1.2 Strain energy release rate computation

In the previous section, a relationship between the applied strain energy release rate and the increase of damage in the cohesive zone was defined. In order to simulate the fatigue crack growth, it is therefore required a general method to calculate the value of the strain energy release rate as a function of crack length. In order to simulate the fatigue crack growth, it is therefore required a general method to calculate the value of the strain energy release rate as a function of crack length. The most common methods for the strain energy release rate evaluation by using the finite element method are the contour integral (J) and the Virtual Crack Closure Technique (VCCT)(see Section 1.4.1). This two methods are usually available in finite element software, but VCCT is intended in general as alternative to using cohesive elements and, additionally, the software used in this work (Abaqus®) did not output the contour integral for an integration path including cohesive element. In order to compute the *J-integral*, a path surrounding the crack has to be selected. Considering for example the crack in Figure 3.3, the path, Π, is displayed by the dashed line and it is represented by all the top and bottom nodes of the cohesive elements.

According to the expression (1.8) given in Section 1.2.2, the strain energy density, W, the traction vector, $\overrightarrow{T}$, and the derivative of the displacement field with respect to x_1 are needed to compute *J-integral.* Expression (1.8) in a 2D plane stress case become

$$\begin{aligned} J = \int_\Pi \left(W dx_2 - \overrightarrow{T} \frac{\partial \overrightarrow{u}}{\partial x} ds \right) = \int_\Pi \tfrac{1}{2} (\sigma_{12}\varepsilon_{12} + \sigma_{22} d\varepsilon_{22}) dx_2 \\ - \int_\Pi (\sigma_{22} n_1 + \sigma_{12} n_2) \frac{\partial u_1}{\partial x_1} ds - \int_\Pi (\sigma_{22} n_1 + \sigma_{12} n_2) \frac{\partial u_1}{\partial x_1} ds \end{aligned} \tag{3.15}$$

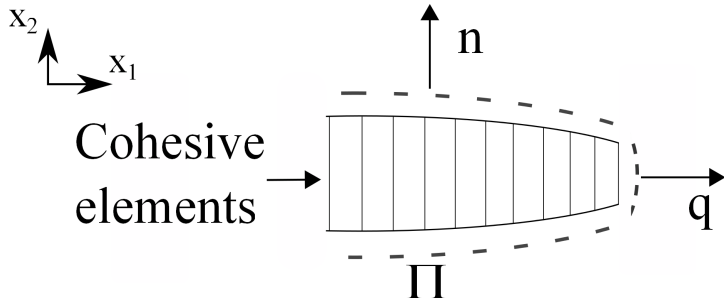

Figure 3.3: *J-integral*

where n_k is the outward unit normal vector to integration path and s is the path coordinate. Following a rectangular path around the cohesive element and considering that its vertical part (along x_2 direction) is faraway from the crack tip, the equation (3.15) can be simplified in that way:

$$J = \int_{\Pi} \left(-\sigma_{12} \frac{\partial u_1}{\partial x_1} - \sigma_{22} \frac{\partial u_2}{\partial x_1} \right) ds \tag{3.16}$$

Extracting the opening/sliding and the stresses in the cohesive elements at the beginning of the increment, the strain energy release rate is then computed. An interesting feature of this approach is that the mode I and the mode II component of the J-integral can be obtained by integrating separately the second or the first components of the integral in Eq. (3.16), respectively. This method can be easily implemented for a two-dimensional problem, since there is only one possible path. In the case of three dimensional problem the implementation is more difficult since several paths can be identified along the crack width, and moreover their definition is rather troublesome, especially when dealing with irregular meshes.

3.2 Finite element implementation *Abaqus®*

3.2.1 User subroutines

The theoretical framework described in the previous section and the strain energy release rate calculation procedure are implemented using the suitable Fortran subroutines in the commercial software Abaqus®. User-subroutines allow users to adapt ABAQUS to their particular analysis requirements. In particular the USDFLD subroutine is used to modify the cohesive element stiffness by means of a field variable that accounts for damage, while the URDFIL subroutine is used to get the result in terms of stresses, displacements and energies. Figure 3.4 shows the basic flow of data, actions from the start of an ABAQUS/Standard analysis to the end of a step. User subroutine USDFLD is typically used when complex material behavior needs to be modeled; some material properties in ABAQUS/Standard can be defined as functions of field variables, f_i. ABAQUS/Standard allows the f_i to be defined as functions of solution data, such as stress or strain, at the material points. The values of the solution data provided are from the beginning of the current increment; subroutine USDFLD must use the ABAQUS utility routine *GETVRM* to access this material point data. The flow diagram in Figure 3.4 shows

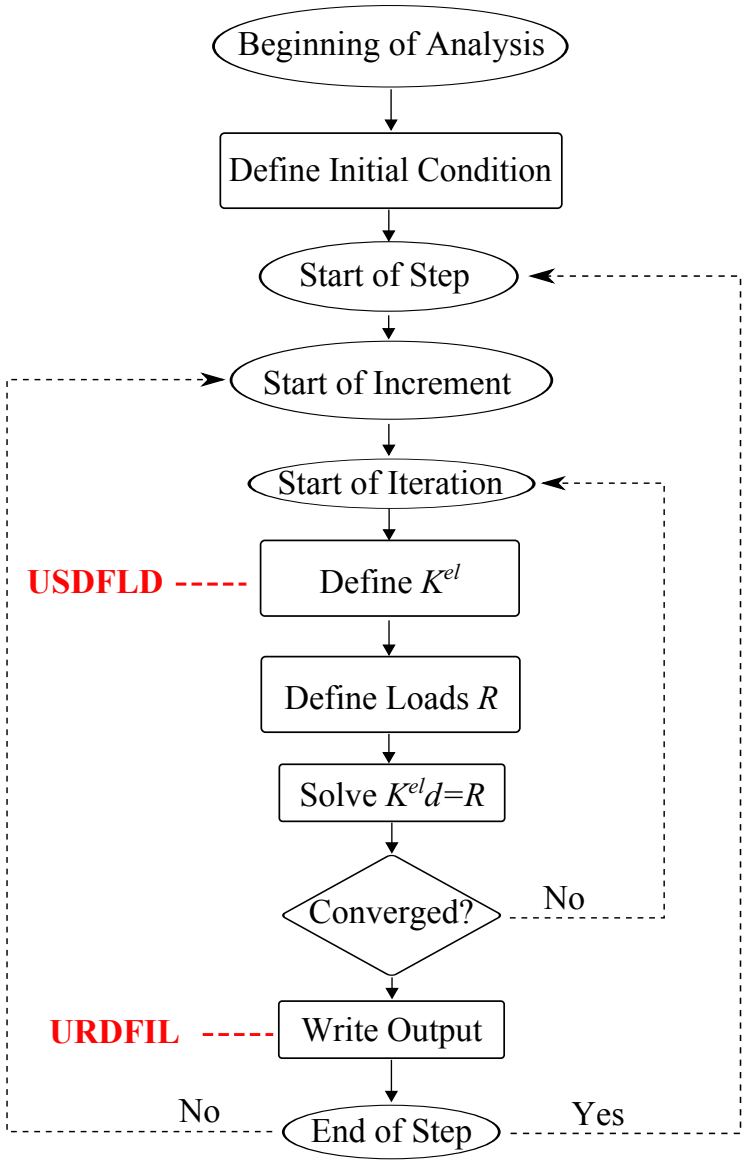

Figure 3.4: Global Flow in Abaqus/Standard

that the USDFLD is called at the start of the increment for defining the properties of the cohesive elements. Subroutine URDFIL is used to read the results (*.fil*) file at the end of an increment. Subroutine URDFIL must call the utility routine *DBFILE* to read records from the results file. Results are extracted from the results file, stored in COMMON blocks, and passed into the subroutine USDFLD.

The fatigue analysis is carried out as a simple static analysis, divided in a certain number of increments. Each increment corresponds to a given number of cycles. Assuming that the fatigue cycle load varies from a maximum value P_{max} to a minimum value P_{min}, the analysis is carried out applying to the model the maximum load P_{max}.

The load ratio is defined as the ratio between the minimum and maximum load applied

$$R = \frac{P_{max}}{P_{min}} \tag{3.17}$$

The strain energy release rate amplitude is therefore

$$\Delta G = (1 - R^2) G_{max} \tag{3.18}$$

This latter is compared with the strain energy release rate threshold ΔG_{th}. If $\Delta G > \Delta G_{th}$ the analysis starts (or it continues is the increment is not the first) otherwise the analysis is stopped. The flow diagram in Figure 3.5 shows the operations done within each increment.

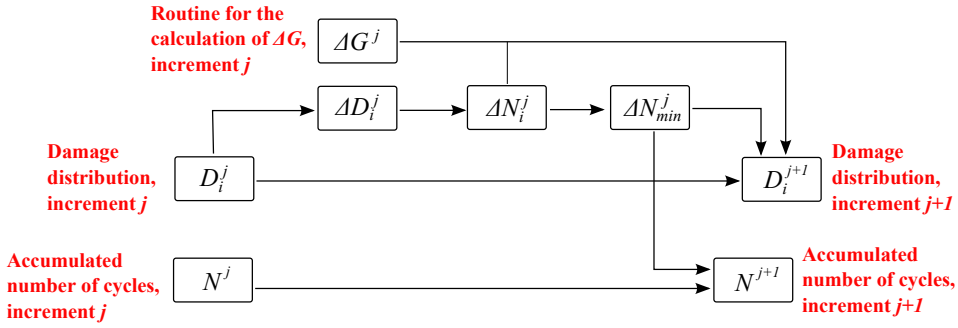

Figure 3.5: Flow diagram of the automatic procedure for the crack growth rate prediction

At the beginning of the increment j the number of cycles (N_j) and the damage variable for each of the *i-th* element (D_i^j) are known. Now for each element the maximum possible damage change within the increment (ΔD_i^j) is computed. If ΔD_{max} is the maximum allowable variation in a single increment (it is a user defined value and it is used in order to ensure a smooth enough crack growth) ΔD_i^j is calculated as follow:

$$\begin{aligned} \Delta D_i^j &= \Delta D_{max} \qquad if \quad 1 - D_i^j > \Delta D_{max} \\ \Delta D_i^j &= \text{1-}D_i^n \qquad if \quad 1 - D_i^j < \Delta D_{max} \end{aligned} \tag{3.19}$$

In other words, ΔD_i^j is the minimum between the $\Delta D_{max}$and the amount needed for D to reach the unity. Therefore, for each element, the amount of number of cycles ΔN_i^j to produce ΔD_i^j is calculated by integrating Eq. (3.14) using the ΔG evaluated within the URDFIL. The strain energy release rate is computed through the (3.16) along a rectangular path extracting stresses and displacement of cohesive elements at the end of the current increment. After that, the routine searches for the minimum value among the calculated ΔN_i^j within the cohesive zone. This value, ΔN_{min}^j, is assumed to be the number of cycles of the increment, ΔN^j. Finally, the number of cycle is updated (N^{j+1}), and using Eq. (3.14) this time to calculate the ΔD_i^j corresponding to ΔN^j the new damage distribution ΔD_i^{j+1} is determined for all the elements belonging to the process zone. It is worth to underline that the procedure is fully automated, i.e. the simulation is performed in a unique run without stops.

3.2.2 FE modelling

For simulating the crack propagation in a bonded joint with the model just described in details, the FE model must contain the adherends and the interface layer where the crack has to increase its length. In Figure 3.6 a typical specimen geometry is shown; depending on how loads and boundary conditions are set, different loading condition can be obtained.

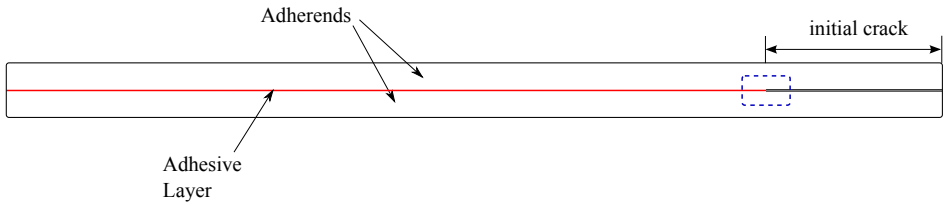

(a) Schematic representation

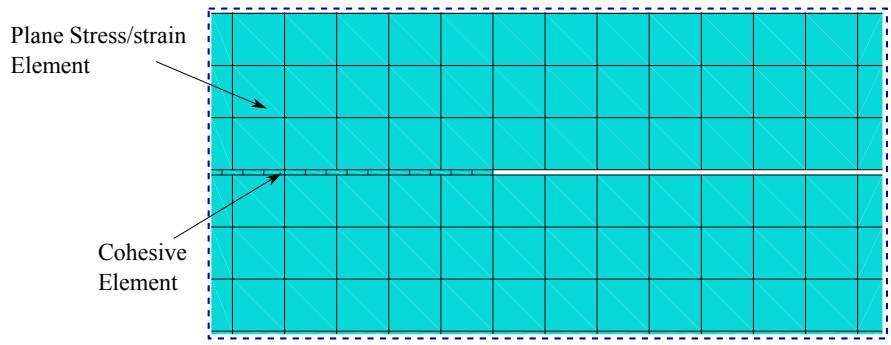

(b) Magnification of rectangular window of Figure 3.6 (b)

Figure 3.6: FE Model of an adhesively bonded joint

For this type of simulation in two-dimension, plane stress elements are used for the adherends while 2D cohesive elements are used to model the adhesive layer. Plane stress elements can be used when the thickness of a body or domain is small relative to its lateral (in-plane) dimensions. The stresses are functions of planar coordinates alone, and the out-of-plane normal and shear stresses are equal to zero. Plane stress elements must be defined in the X–Y plane, and all loading and deformation are also restricted to this plane. Instead plane strain elements can be used when it can be assumed that the strains in a loaded body or domain are functions of planar coordinates alone and the out-of-plane normal and shear strains are equal to zero. Plane strain elements must be defined in the X–Y plane, and all loading and deformation are also restricted to this plane. This modeling method is generally used for bodies that are very thick relative to their lateral dimensions.

The cohesive zone must be discretized with a single layer of cohesive elements through the thickness. Since the cohesive zone represents an adhesive material with a finite thickness, the continuum macroscopic properties of this material are used directly for modeling the constitutive response of the cohesive zone. For debonding/delamination problem cohesive elements have to be connected with adjacent components; if the two neighboring parts do not have matched meshes, such as when the discretization level

in the cohesive layer is finer than the discretization level in the surrounding structures, the top and/or bottom surfaces of the cohesive layer can be tied to the surrounding structures using a tie constraint (see Figure 3.7).

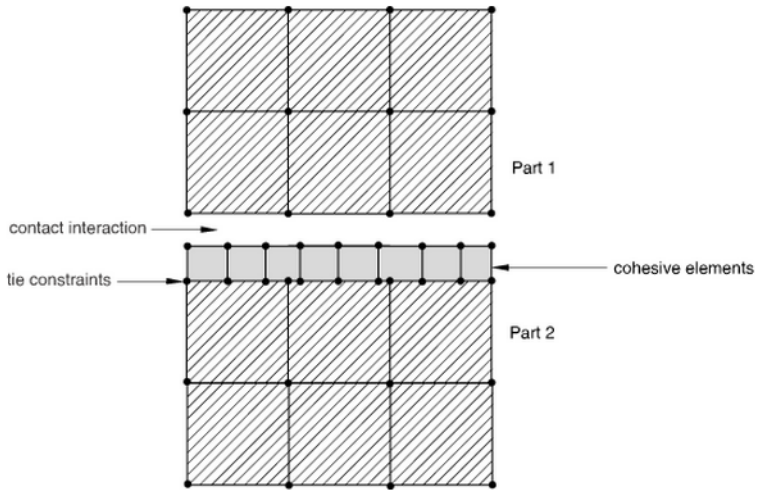

Figure 3.7: Independent meshes with tie constraints [71]

Generally for describing the constitutive behavior of the cohesive elements, the following features are needed:

- the initial stiffness (E_c) that relates the nominal stresses to the nominal strains across the interface. For taking into account the traction separation law that relates stress and displacements, the stiffness of the interface must be considered ($K_c = E_c/t_a$ with t_a the initial thickness of the layer);
- damage initiation condition that refers to the beginning of degradation of the response of a material point. The process of degradation begins when the stresses and/or strains satisfy certain damage initiation criteria that one specifies. Several damage initiation criteria are available in *Abaqus®;*
- damage evolution law that describes the rate at which the material stiffness is degraded once the corresponding initiation criterion is reached. Normally damage evolution can be defined based on the energy that is dissipated as a result of the damage process, also called the fracture energy. The user specifies the fracture energy as a material property and choose either a linear or an exponential softening behavior. *Abaqus®* ensures that the area under the linear or the exponential damaged response is equal to the fracture energy. The dependence of the fracture energy on the mode mix can be specified either directly in tabular form or by using analytical forms provided in *Abaqus®*.

In the model described in this thesis, damage initiation and its evolution are directly implemented in USDFLD and URDFIL subroutines. The damage values (D_i^j) evaluated at the end of increment j, are used in the following increment as field variable in USDFLD routine to reduce the stiffness of the cohesive elements lying in the process zone. The dependance of the stiffness on damage is defined in tabular form (see Figure 3.8).

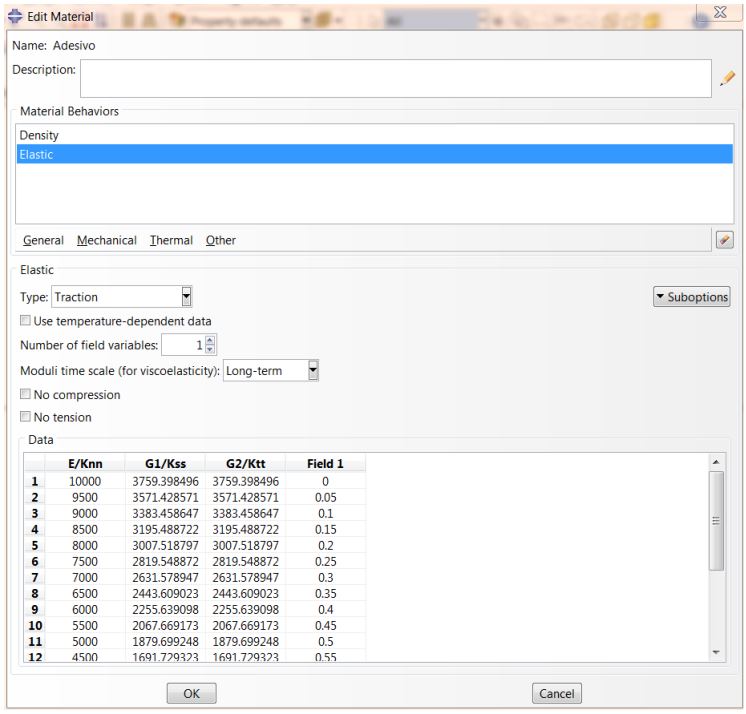

Figure 3.8: *Abaqus* windows to define the dependance of element stiffness (E) on the Damage (*Field 1*)

3.3 Mixed mode loading

With the aim to extend the model to mixed-mode I/II conditions, a mixed mode cohesive law has to be defined.This is done according to the scheme shown in Figure 3.6 from the knowledge of the pure mode I and pure mode II cohesive laws (the index *22*, refers to opening or mode I direction, index *12* refers to sliding or mode II direction).

First of all the mixed mode equivalent opening has to be defined. This is done using the relationship

$$\delta_{eq} = \sqrt{\left(\frac{\delta_{22} + \mid \delta_{22} \mid}{2}\right)^2 + (\delta_{12})^2} \tag{3.20}$$

In case of pure mode I this equation gives as δ_{eq}, the value of δ_{22} in case of positive δ_{22}, while it gives 0 in case of negative δ_{22}. This is done since it is supposed that compression stresses do not lead to the damage of the adhesive layer. Of course δ_{22}assumes only positive values if crack surface compenetration is properly prevented in the model. Moreover the mixed mode cohesive law is defined in terms of the initial stiffness (K^0_{eq}), damage initiation equivalent opening (δ^0_m) and critical equivalent opening (δ^c_m).

The equivalent initial stiffness is obtained by equating the equivalent strain energy (U_{EQ}) to the total strain energy (U_{TOT}), which in turn is equal to the sum of the strain energy in mode I (U_{22}) and in mode II (U_{12})

$$U_{EQ} = U_{TOT} = U_{22} + U_{12} = \frac{1}{2} \left(\delta_{22} + \mid \delta_{22} \mid\right)^2 \cdot K_{22}^0 + \frac{1}{2} \delta_{12}^2 \cdot K_{12}^0 \tag{3.21}$$

where K_{22}^0 and K_{12}^0 represent the initial stiffnesses of the mode I and mode II cohesive laws, respectively.

A further relationship is needed to define damage initiation: this is done using a the quadratic failure criterion (Ungsuwarungsru and Knauss, [69])

$$\left(\frac{\sigma_{22}}{\sigma_{22max}^0}\right)^2 + \left(\frac{\sigma_{12}}{\sigma_{12max}^0}\right)^2 = 1 \tag{3.22}$$

The last relationship needed, regards the definition of the critical equivalent opening. Since the area underlying the cohesive law is representative of the critical strain energy release rate, using the Kenane and Benzeggagh (KB) theory [70] the area underlying the mixed mode equivalent cohesive law (Γ_{eq}) can be computed as

$$\Gamma_{eq} = \Gamma_I + (\Gamma_{II} - \Gamma_I) \cdot MM^{\eta} \tag{3.23}$$

where Γ_I and Γ_{II} are the areas underling the mode I and mode II cohesive laws, respectively, η is a mixed mode coefficient depending on the adhesive and MM is the mixed mode ratio defined as a function of the mode I and mode II strain energy release rates as follows:

$$MM = \frac{G_{II}}{G_I + G_{II}} \tag{3.24}$$

The KB mixed mode fatigue crack propagation model [70] is the first considered, since it is the most general law that can be found in the literature. The fatigue crack growth rate is given by Eq. (2.3) where this time C and n are functions of the mixed mode ratio MM:

$$n = n_I + (n_{II} - n_I) \cdot MM^{n_n} \tag{3.25}$$

$$\ln C = \ln C_{II} + (\ln C_I - \ln C_{II}) \left(1 - MM\right)^{n_C} \tag{3.26}$$

and n_I, C_I and n_{II}, C_{II} are, respectively, the parameters of the Paris law in mode I and mode II and n_n, n_C are material parameters.

3.4 *FCG* simulations

The fatigue delamination model, above described, has been tested on various joint geometries characterized by varying mixed mode ratios, in order to verify accuracy, robustness and performance in terms of computational time. In particular, pure on mode I, mode II and mixed-mode loaded cracks in composite assemblies have been simulated. The results obtained have been compared VCCT fatigue simulations provided by Andrea Bernasconi and Azhar Jamil from the "Politecnico di Milano", Milano, Italy. These results were jointly published in [73].

3.4.1 VCCT for *FCG* simulation in *Abaqus®*

VCCT (see Section 1.4.1) is well implemented in *Abaqus®* for both two and three dimensions. In a two dimensional problem, the crack is represented as a one-dimensional discontinuity formed by a line of nodes with the bulk material located on both sides of the discontinuity, as seen in Figure 3.9. The bulk material is modelled in the form of two distinct parts joined together by means of a contact pair all along the discontinuity, having either of the coinciding edges to be a master surface and the other to be a slave surface. The nodes on the discontinuity share the same coordinates and play an important role in the definition of pre-cracked region, the crack front and the crack path.

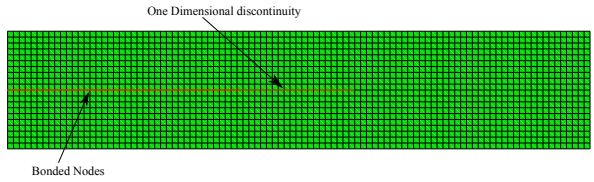

(a) Undeformed shape with initial crack

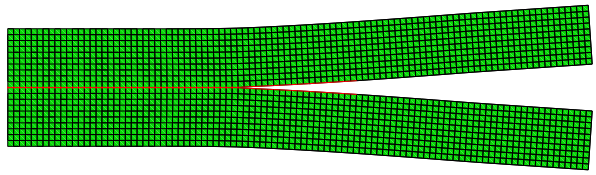

(b) Deformed shape with initial crack

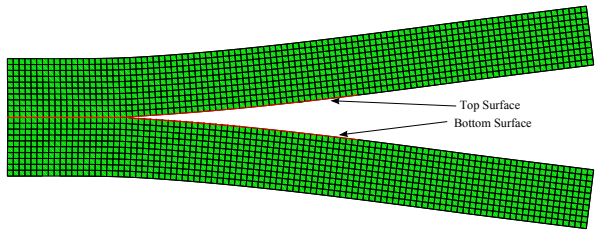

(c) Deformed shape with crack length increased

Figure 3.9: VCCT implementation in *Abaqus®*

The nodes on the discontinuity, which are not bonded and free to move away from each other, represent the pre-crack region, whereas, the nodes which are bonded and

stick to each other, referred as bonded nodes, define the crack propagation path and the point of transition of bonded and unbounded nodes forms the crack front. It is possible to define a completely bonded interface; however at least single node has to be kept unbounded for the identification of the crack front. Normal surface behaviour is specified for the contact pair with pressure-overclosure=HARD and the initial conditions of the contact pair are set to bonded, over the bonded nodes by means of the following lines inserted in the input file before the definition of the step

*INITIAL CONDITIONS, TYPE =CONTACT
<Slave Surface>, <Master Surface>, <Bonded Node Set>

A structured mesh with an aspect ratio of 1 is preferred in the meshing of the region forming the crack path and is done in such a way that the nodes on the contact edge of one side of the bulk material are exactly having the same coordinates to the nodes on the contact edge of the other side of the bulk material along the crack path. The loading cycle is represented by means of *AMPLITUDE term, which may be periodic, tabular etc. depending on loading history, R ratio etc. In the present study a sinusoidal loading history was implemented and the corresponding parameters were defined. In the definition of the step, at the end of every increment, the strain energy release rates are calculated using the *DEBOND command which is used to specify that crack propagation may occur between two surfaces that are initially partially bonded. This is done by inserting the following lines in the Step module

*DEBOND, SLAVE=<Slave Surface>, MASTER=<Master Surface>

This is followed by the definition of the criterion, using *FRACTURE CRITERION command, which governs the fracture of the bonded region by releasing the bonded nodes and letting the crack propagate along the crack path. For the case of static crack propagation this criterion is set to TYPE = VCCT by inserting the following lines

*FRACTURE CRITERION, TYPE=VCCT
<GIc>, <GIIc>, <GIIIc>, <eta>

in which the second line denotes the material parameters.

For the case of fatigue crack propagation Eq. (2.3) is followed by setting this criterion to TYPE = FATIGUE, in the direct cyclic step, and the following lines are inserted in the input file

*FRACTURE CRITERION, TYPE=FATIGUE
<c1>, <c2>, <c3>, <c4>, <r1>, <r2>,
<GIc>, <GIIc>, <GIIIc>, <eta>

in which <c1>, <c2>, represents the fatigue crack onset parameters, <c3>, <c4> represent the Paris parameters of the fatigue crack propagation, <r1>, represents the definitions of the threshold regions of the Paris curve which is given by (r1 = G_{thresh}/G_c), <r2> represents the definition of the unstable region of the Paris curve and is given by (r2 = G_{pl}/G_c) , and rest of the parameters signify the material parameters. The advancement of the crack is determined by applying the Paris Law, which is based of the total strain energy release rate G_{TOT} in a direct cyclic analysis.

Direct cyclic analysis, as implemented in *Abaqus®*, is a quasi-static analysis which utilizes a combination of Fourier series and time integration of the nonlinear material by iteratively utilizing the modified Newton method, with the elastic stiffness matrix at the beginning of the analysis step serving as the Jacobian, for obtaining the stabilized

response of an elastic-plastic structure subjected to constant amplitude cyclic loading. It effectively provides the cyclic response of the structure directly by neglecting the pre-stability loading cycles of a transient analysis which are numerically quite expensive. The workflow of the procedure is described in Figure 3.10. The method is based on the

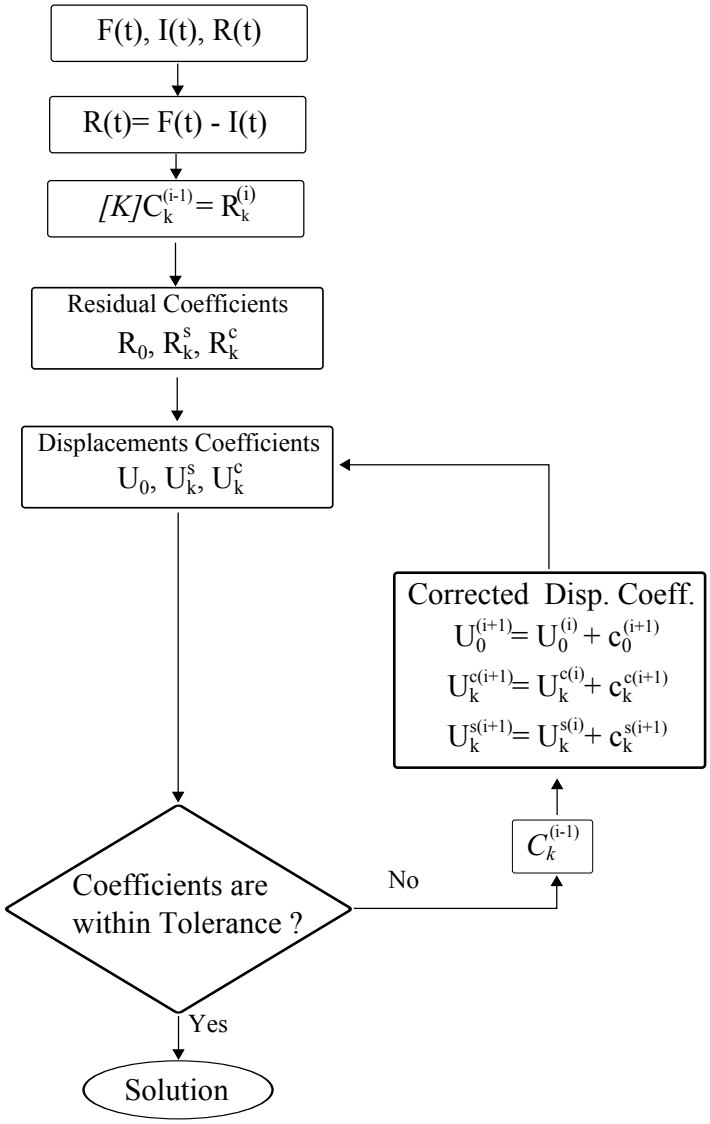

Figure 3.10: Direct Cyclic Algorithm

development of a displacement function *F(t)* which describes the structural response at all moments of time t, in a loading cycle, within a given time period T. This function is represented in the following way

$$U(t) = U_0 + \Sigma_{k=1}^{n} \left[U_k^s \sin k\omega t + U_k^c \cos k\omega t\right] \tag{3.27}$$

where, n represents the number of terms in the Fourier series, ω is the angular

frequency, and U_0, U_k^s, U_k^c are the coefficients of displacement corresponding to each degree of freedom.

The residual vectors are of the same form as the displacement function and are represented by

$$R\,(t) = R_0 + \Sigma_{k=1}^{n}\,[R_k^s \sin k\omega t + R_k^c \cos k\omega t] \tag{3.28}$$

Where R_0, R_k^s and R_k^c have the same correspondence with the displacement coefficients U_0, U_k^s and U_k^c respectively and this vector *R(t)* is tracked for each instance of time in the loading cycle by using element to element calculations. The integration of this function *R(t)* over the entire cycle yield the following Fourier coefficients.

$$\begin{aligned} R_0 &= \tfrac{2}{T}\int_0^T R\,(t)\,dt \\ R_k^s &= \tfrac{2}{T}\int_0^T R\,(t)\sin k\omega t\,dt \\ R_k^c &= \tfrac{2}{T}\int_0^T R\,(t)\cos k\omega t\,dt \end{aligned} \tag{3.29}$$

These coefficients correspond to the displacement coefficients and are then compared with the tolerances defined in the step to achieve convergence. If the tolerance is met convergence is achieved and the solution is obtained for that loading cycle. However, when these residuals are larger than the tolerance parameters then correction parameter c_k is evaluated in which corrections to the displacement coefficients c_0, c_k^s and c_k^c are made in the following way

$$\begin{aligned} U_0^{(i+1)} &= U_0^{(i)} + c_0^{(i+1)} \\ U_k^{s(i+1)} &= U_k^{s(i)} + c_k^{s(i+1)} \\ U_k^{c(i+1)} &= U_k^{c(i)} + c_k^{c(i+1)} \end{aligned} \tag{3.30}$$

The updated displacement coefficients are used in the next iteration to obtain displacements at each instant in time. This process is repeated until convergence is obtained. Each pass through the complete load cycle can therefore be thought of as a single iteration of the solution to the nonlinear problem. The general syntax of the direct cyclic analysis pertaining to fatigue may be represented as

*DIRECT CYCLIC, FATIGUE
I_0, T_S, F_i, F_{max}, ΔF, i_{max},
N_{min}, N_{max}, N_{TOT}

where, I_0 represents the initial time increment size and if unspecified a default value equal to 0.1 times the single loading cycle period is assumed, T_S is the time of single loading cycle, the next two blank value are respectively minimum and maximum time increment allowed which are generally kept unspecified and a default of 10^{-5} times T_S for the first parameter (Minimum time increment allowed) and a default of 0.1 times T_S, for the second parameter (Maximum time increment allowed) unless the CETOL or DELTMAX parameter is specified. F_i represents the initial number of terms in the Fourier series with a default of 11; F_{max} represents the maximum number of terms in the Fourier series having a default value of 25; ΔF represents the increment in the number of terms in Fourier series with a default of 5 and i_{max} represents the maximum number of

iterations having 200 as the default value. The second line comprises of minimum N_{min} and maximum increment N_{max} in number of cycles over which damage is extrapolated forward. The default value of N_{min} and N_{TOT} are 100 and 1000 respectively. N_{TOT} represents the total number of cycles allowed in a step, which if skipped is assigned by default a value of $(1+N_{max}/2)$.

3.4.2 Comparison of cohesive zone and VCCT on fatigue debonding

The CZ model has been validated by means of the well-established Virtual Crack Closure Technique. In particular the following geometries have been simulated with both method:

- Double Cantilever Beam (DCB) geometry to test pure mode I loading
- End Loaded Split (ELS) geometry to test pure mode II loading
- Mixed Mode End Loaded Split (MMELS) geometry to test mixed mode I/II loading

Additionally, a Single-Lap Joint (SLJ) has been modelled as a representative case of real joint geometry. The propagation of the crack in the SLJ was allowed only on one side to simplify the comparison of the models results. All the specimen geometries are schematically described in Figure 3.11, while in Table 3.1 the applied load and the specimens dimensions are summarized.

The elastic properties of composite laminate are taken from Bernasconi et al. [22] (see Table 3.2) while the cohesive law and FCG behaviour is taken from Turon et al. [61] (see Table 3.3). In all the simulation a load ratio R = 0.05 is assumed.

The element type and mesh size are reported in Table 3.4, which represent a good balance between convergence on strain release rate and computational cost. Other parameters to be set, specific of each FCG model, are:

- a maximum damage increment, $\Delta D_{max} = 0.2$ has been used for CZ [65]
- a number of Fourier series terms 49 and a time increment 0.001 have been set for VCCT except for SLJ where the time increment was set to 0.01 due to finer mesh.

The choice of a very small time increment in the VCCT solution has followed from a convergence study. Indeed, a strong influence of time integration points was observed on the results obtained by VCCT and different values of SERR were obtained when the time integration points were varied from 10 to 1000. As a result of these variations in SERR, there were significant differences in the estimation in the number of cycles due to the presence of high values of the exponent in the Paris Law. Therefore, 1000 time integration points with an initial time increment of 0.001 were used to evaluate accurate results which however, increased the computational time drastically.

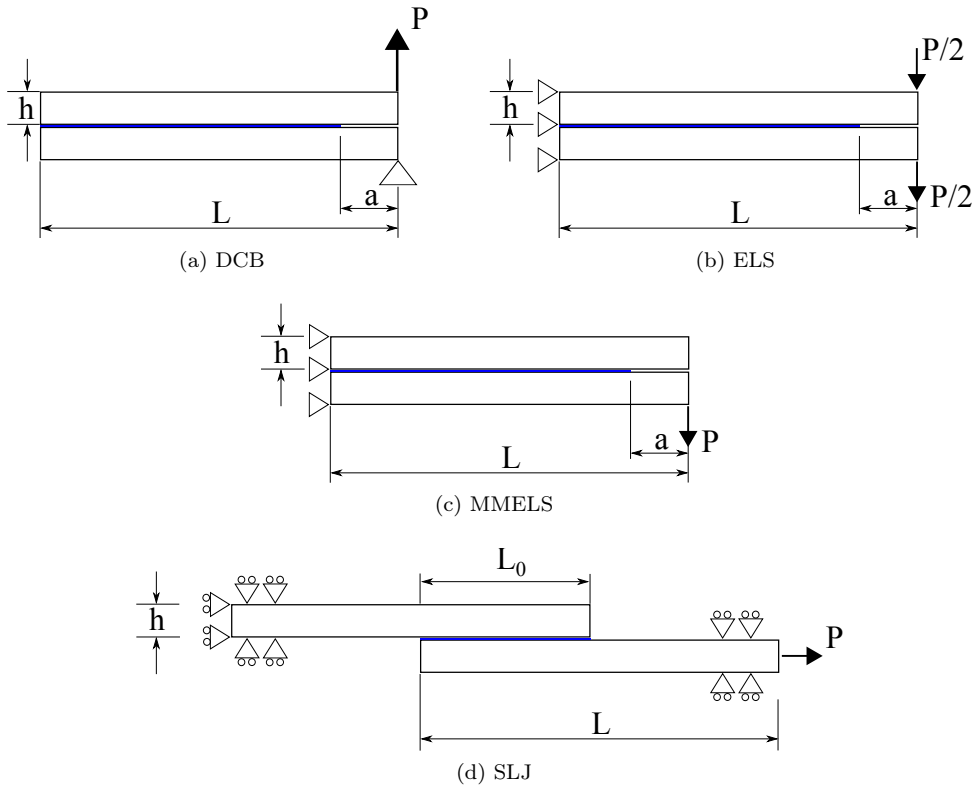

(a) DCB

(b) ELS

(c) MMELS

(d) SLJ

Figure 3.11: Specimen geometries

	DCB	ELS	MMELS	SLJ
$P\,[N/mm]$	10	20	15	200
$a_0\,[mm]$	20	20	20	/
$h\,[mm]$	5	5	5	10.56
$L\,[mm]$	175	175	175	285.8
$L_0\,[mm]$	/	/	/	110.8

Table 3.1: Specimens dimension and applied load

Parameter	Value
$E_{11}\,[MPa]$	54000
$E_{22}\,[MPa]$	8000
ν_{12}	0.25
$G_{12}\,[MPa]$	2750

Table 3.2: Engineering constants of the woven plies

Parameter	Mode I	Mode II
$\Gamma_0\,[N/mm]$	0.266	1.002
$\sigma_{max}\,[MPa]$	30	30
$\delta^0\,[mm]$	0.003	0.003
$\delta^c\,[mm]$	0.0173	0.066
C	0.0616	4.23
n	5.4	4.5
Parameter		Value
η		2.6
n_n		1.85
n_C		0.35

Table 3.3: Cohesive zone parameters and FCG behavior for Mode I, Mode II, and Mixed-Mode

	Composite laminate		**Cohesive Zone**	
	Element type	Size	Element type	Size
DCB	4-node bilinear plane stress quadrilateral, reduced integration	0.5 mm	4-node two-dimensional cohesive element	0.2 mm
ELS	4-node bilinear plane stress quadrilateral, reduced integration	0.5 mm	4-node two-dimensional cohesive element	0.5 mm
MMELS	4-node bilinear plane stress quadrilateral, reduced integration	0.5 mm	4-node two-dimensional cohesive element	0.2 mm
SLJ	4-node bilinear plane stress quadrilateral	0.1 mm (next to cohesive elements)	4-node two-dimensional cohesive element	0.1 mm

Table 3.4: Element types and mesh sizes

An initial crack length of 0.1 mm (1 element) has been specified for the SLJ when simulated using VCCT, while no initial crack length was needed in the case of CZM. The increment in crack length is fixed in the case of VCCT, i.e. equal to element size along the delamination/debonding interface (0.1mm for the SLJ, 0.5mm elsewhere), while in the case of CZ it comes as a result of in the increment in damage ΔD, therefore it is not generally constant as ΔD may vary from increment to increment according to Eq. (3.19). However, the average increment in crack length in the case of CZ model ranged from 0.1 to 0.5mm in the various cases simulated in this work.

The two methods are compared with respect to:

1. agreement with each other;

2. agreement with numerical integration of Equation (2.2);

3. calculation time

Concerning the second point, the numerical integration was done using ΔG as a function of crack length coming from the FE simulations. As ΔG is known by FE analysis, the trapezoidal rule (i.e. using the mean ΔG over the increment) was used. In this way, a closer estimate of the number of cycles at failure should be obtained with respect to both the CZ and VCCT, where for numerical reasons the ΔG at the beginning of the increment is used. As Equation (2.2) represents the best fit of experimental data, the level of agreement between the number of cycles output by the models and the numerical integration of Eq. (2.2) represents also the level of agreement between experimental data and the simulations. Regarding the third point, it is the time the analyst has to wait for the crack to reach the knee of the *a-N* diagram, that is close to fracture. In the cases studied here this means a crack length of 40 mm for all the geometries except SLJ, for which the analyses have stopped at 40mm of crack length even though still far from fracture. Only the outputs strictly necessary for each model were required, in order to minimize time spent in storing data. The PC used for calculations is an Athlon X2 Dual Core 2GHz CPU, with 2Gb RAM and 200Gb HD (7200rpm, 8Mb cache).

3.5 Results

3.5.1 Mode I loading

The crack growth in a cracked DCB specimen is simulated with cohesive zone model. Every increment correspond to a ΔN^jas described in 3.2.1. The joint deformed shape and damage distribution of cohesive elements near the crack tip is reported in Figure 3.12 and 3.13 for two different crack length.

Figure 3.14.a shows the values of G_I obtained by CZ, VCCT and J-integral (stationary crack). The three sets show a very good correspondence with each other as expected, with only some small oscillation in the strain energy release rate calculated using the subroutine in the case of CZ.

The main result in terms of crack length versus number of cycles is shown in Figure 3.14.b, where a very little difference, of about 2.5%, is evident. Another very little difference is the gradient in *a-N* trend while approaching G_{Ic}, which is much steeper (almost discontinous) in the case of VCCT. In the automated model presented, it is considered that locally some element could be in a critical stress condition with respect to the cohesive law; so in addition to the fatigue damage, eventually a static damage is determined using expression (3.4). To about a crack length of 30 mm (at knee of the diagram in Figure 3.14.b).

Both CZ and VCCT yielded a higher number of cycles with respect to the numerical integration of Eq. (2.3), with a difference 2.3% in the case of CZ and 1.8% in the case of VCCT which is acceptable in engineering terms.

3.5.2 Mode II loading

Figure 3.15.a shows the values of G_{II} obtained by CZ, VCCT and J-integral (stationary crack). The three sets show a very good correspondence with each other especially until 80 mm of crack length, while for longer cracks the CZ - G_{II} is slightly lower than

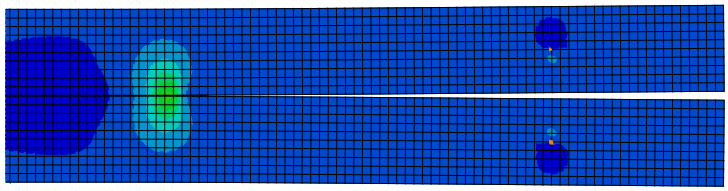

(a) Deformed shape of DCB joint

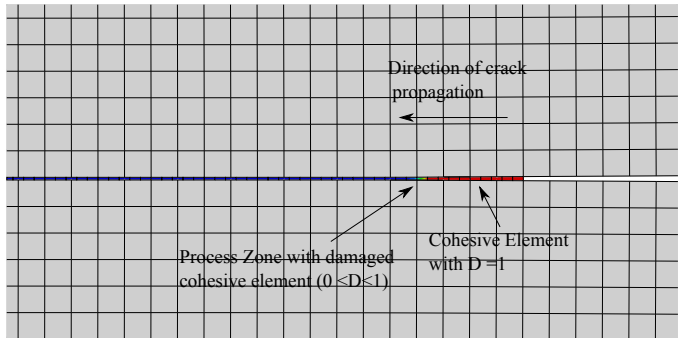

(b) Damage distribution near the crack tip

Figure 3.12: Fatigue simulation at *increment 25*

the VCCT one and the J-integral lies in between. The main result in terms of crack length vs. number of cycles is shown in 3.15.b, where a difference of about 11% comes out. The number of cycles at failure was obtained also by integrating Eq. (2.3) using the trapezoidal rule and the ΔG as a function of crack length coming from the FE simulations. Both CZ and VCCT yielded a higher number of cycles with respect to the numerical integration of Eq. (2.3), with a negligible difference both in the case of CZ and VCCT.

3.5.3 Mixed-Mode I/II loading

Figure 3.16.a shows the values of G_I and G_{II} obtained by CZ and VCCT. The values obtained with the two methods show a very good correspondence with each other in the case of the Mode I component, as for the DCB geometry. Under Mode II the agreement is good especially until 50 mm of crack length alike the ELS, while for longer cracks the CZ- GII is lower than the VCCT one. The main result in terms of crack length vs. number of cycles is shown in Figure 3.16.b, where a very little difference of about 4% comes out. The number of cycles at failure was obtained also by integrating Eq. (2.3) using the trapezoidal rule and the ΔG as a function of crack length coming from the FE simulations. Both in the case of CZ and VCCT the numerical integration of Eq. (2.3) yielded a lower number of cycles, with a difference 5.5% in the case of CZ and 8.3% in

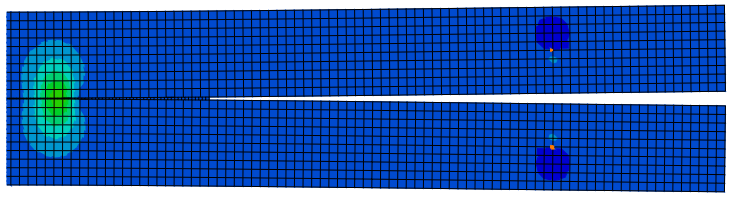

(a) Deformed shape of DCB joint

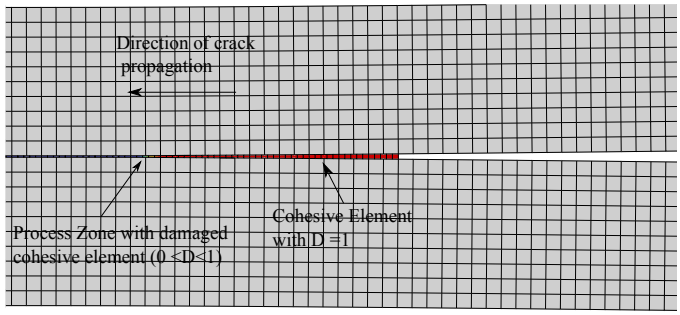

(b) Damage distribution near the crack tip

Figure 3.13: Fatigue simulation at *increment 88*

the case of VCCT which may be still acceptable in engineering terms.

3.5.4 Single-lap joint

Figure 3.17.a shows the values of G_I and G_{II} obtained by CZ and VCCT. The values obtained with the two methods show a good correspondence with each other in the case of both mode components in the first millimeters of propagation, while at longer cracks the CZ values are lower than the VCCT ones. A higher difference is noticed in the case of the Mode II component, someway similarly to Mode II and Mixed-Mode I/II loading. However, in those cases the difference in the number of cycles between the two models to failure was affected to a limited extent, while in the case of SLJ the discrepancy is much higher (see Figure 3.17.b). This discrepancy however, is due especially to the fact that VCCT at present does not allow to modify the coefficient (C) and exponent (n) of Eq. (2.3) according to the mixed-mode ratio *MM* (see Equations. (3.24)-(3.26), Kenane and Benzeggagh, [70]) as CZ instead does. In the case of SLJ, the MM ratio increases steeply in the first 5mm of propagation and then becomes almost stationary (ranges between 0.55 and 0.56, Figure 3.20), and the VCCT simulation has been performed in this case using the stationary MM value. If the mixed-mode ratio *MM* versus the crack length is plotted for both approaches, a similar trend is obtained (see Figure 3.18). In VCCT case the actual mixed-mode ratio is evaluated considering the strain energy release rates in

Mode I and Mode II obtained from the simulations. Both in the case of CZ and VCCT the numerical integration of Eq. (2.3) yielded a lower number of cycles, with a difference (after 48mm of crack propagation) of 2.6% in the case of CZ and 1.1% in the case of VCCT which is absolutely acceptable in engineering terms.

3.6 Calculation time

The calculation times are reported in Table 3.5. The CZ results on average two-order of magnitude quicker than VCCT, with calculation times of the order of minutes instead of hours. In the case of SLJ, the increase in calculation time is related to the finer mesh, but the time required by VCCT is becoming so important that high performance computing may be needed if the model complexity would increase further. The origin of this large difference in performance between the in-house CZ subroutine and the built-in VCCT, both run using the Abaqus solver, can be at least partly found in the Direct Cyclic procedure that is associated with VCCT in Abaqus. Indeed, this procedure requires quite a large number of iterations to satisfy convergence on ΔG value. On the other hand, relaxing the convergence on ΔG may affect the number of cycles to failure in a hardly predictable way.

	DCB	ELS	MMELS	SLJ
CZ	9.1	4.6	4.5	21.4
VCCT	676.2	688.6	727.5	2796.8

Table 3.5: Computational time for both method (time is reported in *minutes*)

3.7 Conclusions

The comparison of the performances of the cohesive zone model and the Virtual Crack Closure Technique (VCCT) embedded in the software Abaqus on mode I, mode II and mixed-mode I/II loaded cracks in composite assemblies yielded the following results:

- the two models agree on each other to within 4% except in the case of SLJ, where VCCT at present does not allow to modify the coefficient (C) and exponent (n) of Eq. (2.3) according to the mixed-mode ratio MM as CZ instead does. Therefore, the rapid increase of MM in the first millimeters of propagation generates a large discrepancy between the two models. In this sense the CZ model offers an additional feature with respect to Abaqus VCCT.

- while the modeling effort is a bit higher (need of introducing a layer of cohesive elements), the CZ model results of easier use (no need to identify the proper number of Fourier terms and time increment to represent cyclic loading). At the same time, it results more efficient as the computation is lower of about two orders of magnitude, even though the origin of this large difference in performance can be at least partly found in the Direct Cyclic procedure that is associated with VCCT in Abaqus.

It is interesting to plot the behavior of a cohesive element during the fatigue simulation in terms of stress and opening (see Figures 3.19.a - 3.19.b). The approach described and its implementation allow cohesive elements to have stresses and opening within the traction separation law defined as input; but sometimes, during the fatigue simulation, the cohesive elements can be in *stress-opening* condition that does not respect the cohesive law. This is due to the fact that static and fatigue damage were assigned within the subroutine at the beginning of an increment. But at the end of the increment, the stresses coming out from the convergence of the whole structure can be a little higher than softening part of cohesive law.

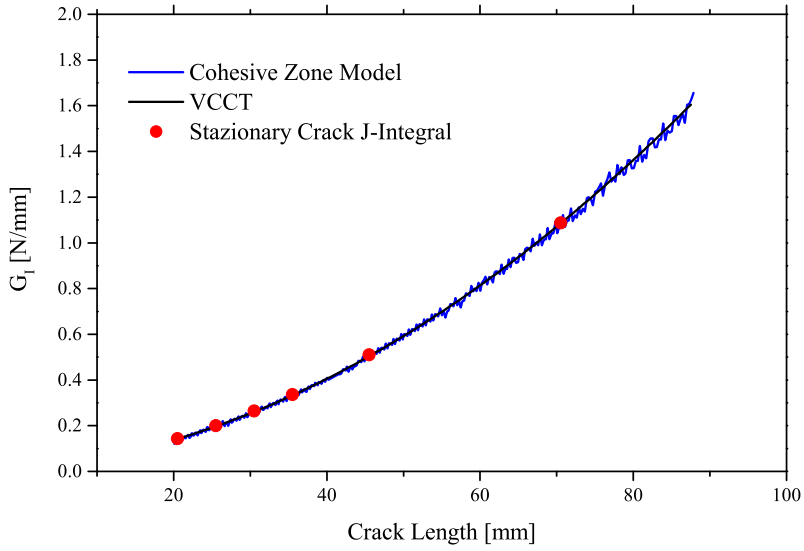

(a) Comparison of a – G_I values

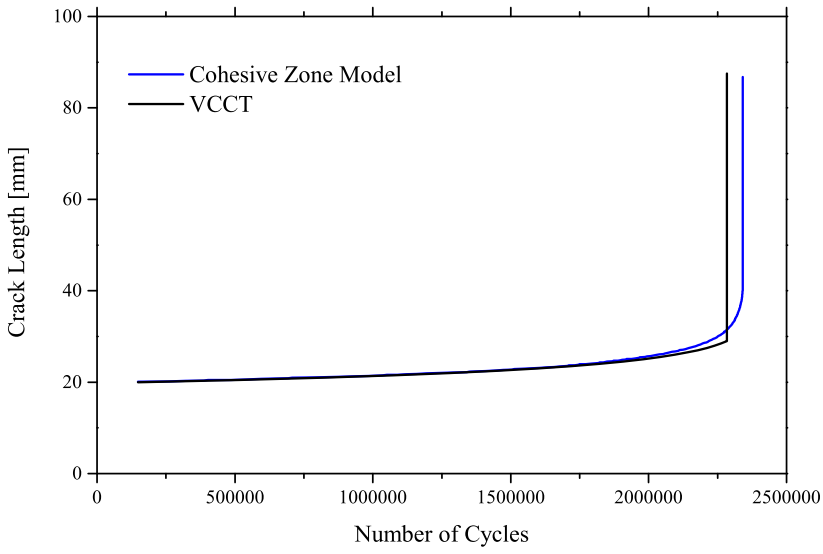

(b) Comparison of a - N values

Figure 3.14: CZM 2D results compared with VCCT 2D ones

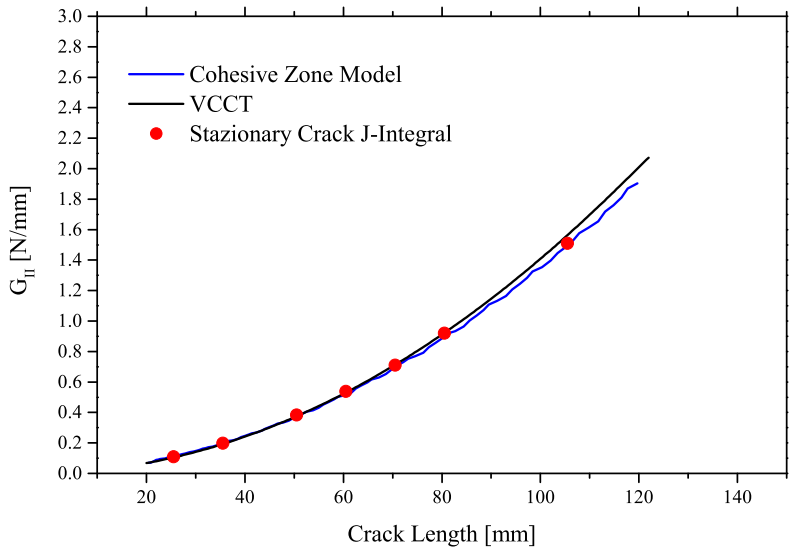

(a) Comparison of a – G_{II} values

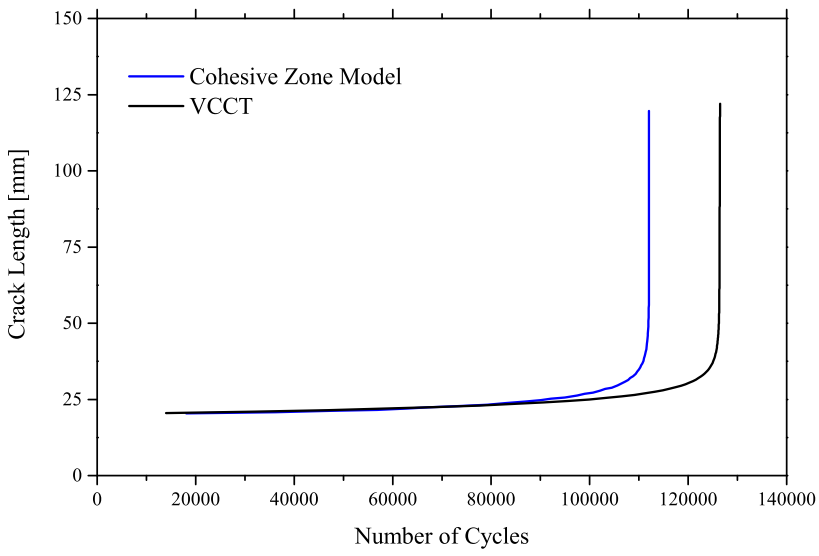

(b) Comparison of a - N values

Figure 3.15: CZM 2D results compared with VCCT 2D

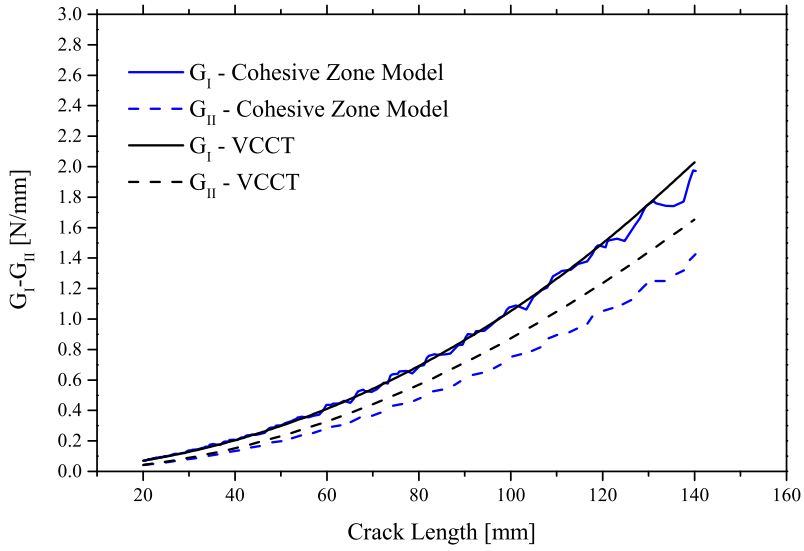

(a) Comparison of a – G_I /G_{II} values

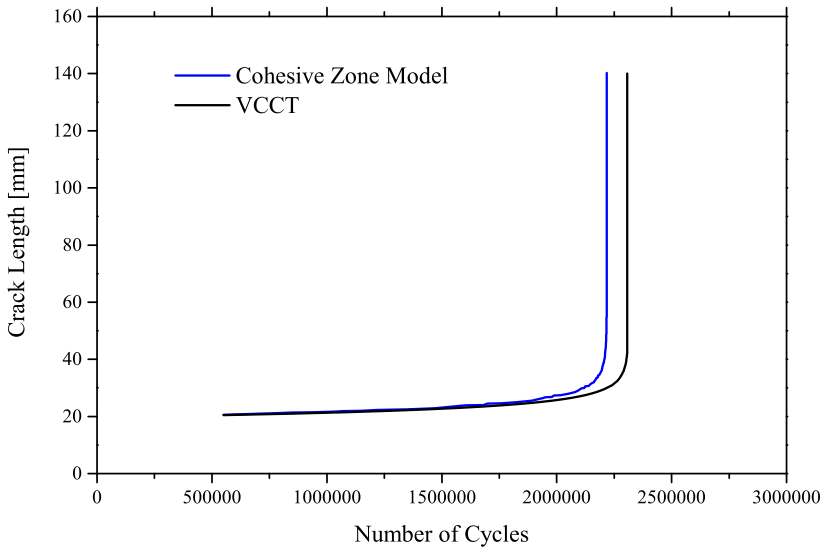

(b) Comparison of a - N values

Figure 3.16: CZM 2D results compared with VCCT 2D

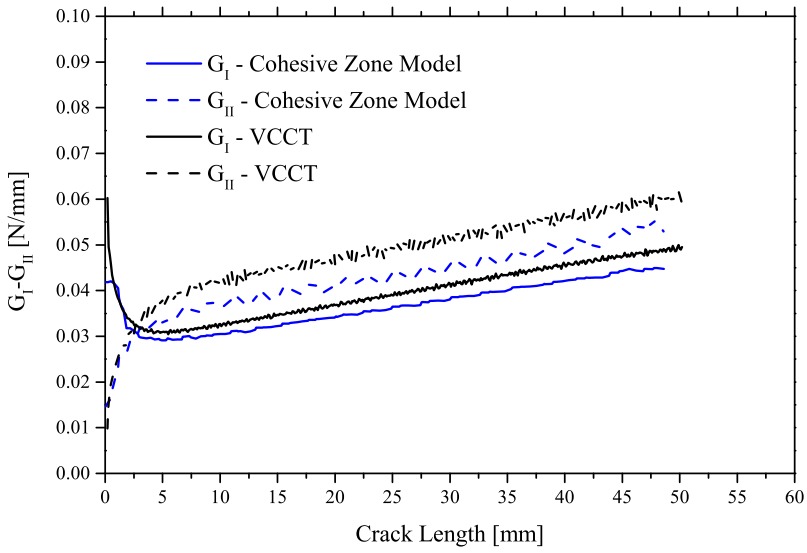

(a) Comparison of a – G_I /G_{II} values

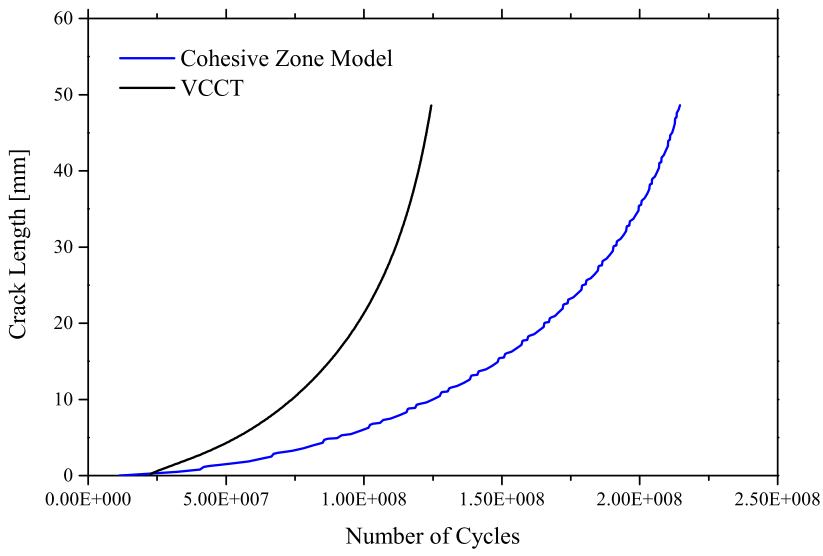

(b) Comparison of a - N values

Figure 3.17: CZM 2D results compared with VCCT 2D ones

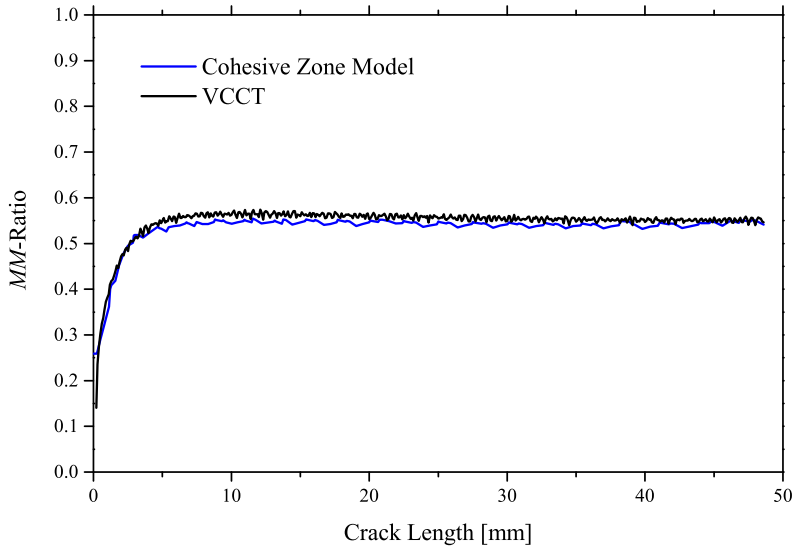

Figure 3.18: Comparison of *MM* ratio obtained by CZM and VCCT in the case of SLJ

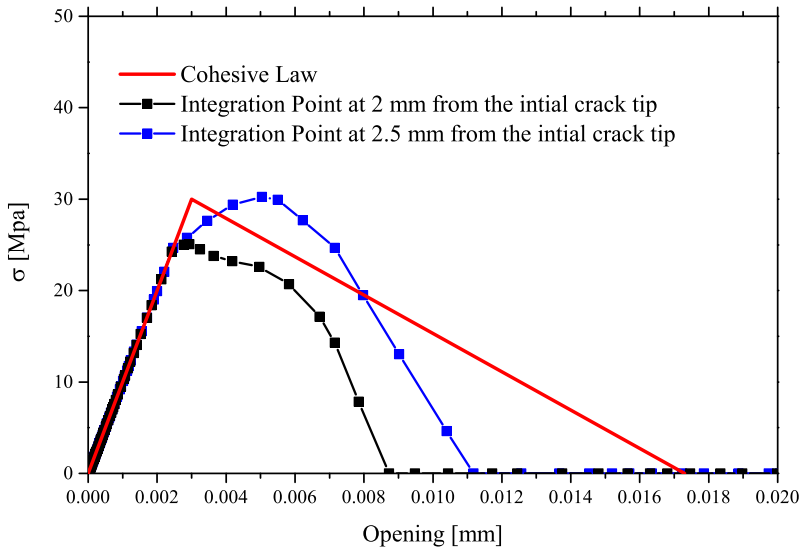

(a) Fatigue Degradation ($\Delta D_{max} = 0.1$)

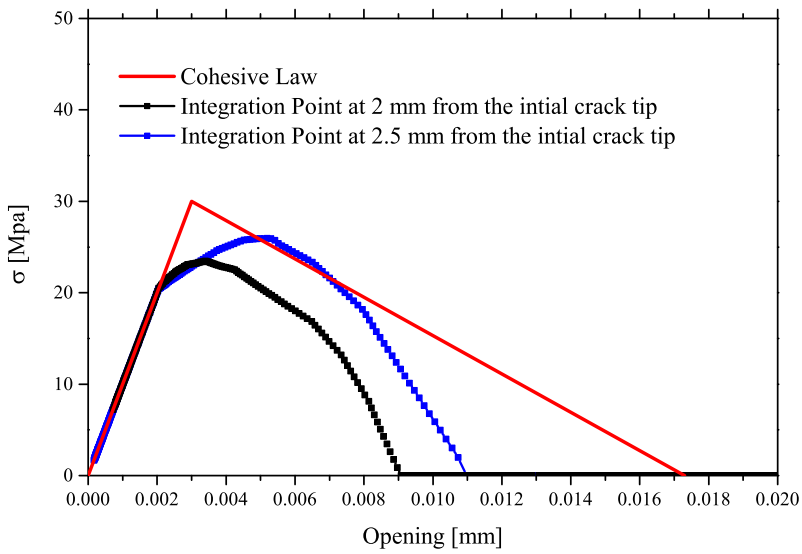

(b) Fatigue Degradation ($\Delta D_{max} = 0.01$)

Figure 3.19: *Stress-Opening* values during the fatigue simulation for two different Integration Point

Chapter 4

Development of CZM for three-dimensional fatigue debonding of adhesive joints with planar cracks

4.1 Model implementation in 3D problems

The approach presented has been easily implemented for a two-dimensional problem, since there is only one possible path. In the case of three dimensional problems, the implementation is more difficult since several paths can be identified along the crack width, and moreover their definition is rather troublesome, especially when dealing with irregular meshes. A three-dimensional version has been implemented for the case of planar crack geometries and regular cohesive mesh, for which Eq. 3.16 is evaluated on several parallel contours in order to obtain J-integral along the crack front.

Precisely the model is separated in slices (Figure 4.1), where every slice corresponds to a row of cohesive elements in the direction of crack propagation. The *COH3D8* element, used to mesh the cohesive zone, has eight nodes and four integration point as shown in Figure 4.2. So the routine, for each cohesive element lying on the same path, extracts stresses and openings in all integration point; but for evaluating the J-integral, the routine uses averaged value (stresses and displacements) in the centroid.

The flow diagram, shown in Figure 3.5, is still representative of the model approach; the routine calculates for each integration point the number of cycles ΔN_i^j to produce ΔD_i^j integrating Eq. (3.14) and searches for the minimum value among the calculated ΔN_i^j within all the path of the cohesive zone. This value, ΔN_{min}^j, is assumed to be the number of cycles of the increment, ΔN^j. The updated damage distribution is determined similarly to the procedure described in the previous chapter.

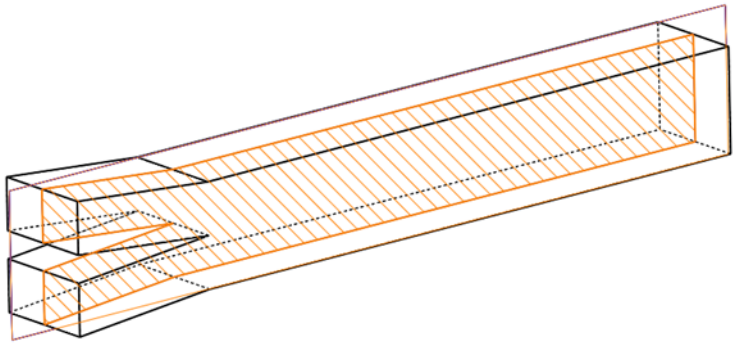

Figure 4.1: Contour evaluation ("path") in a 3D specimen

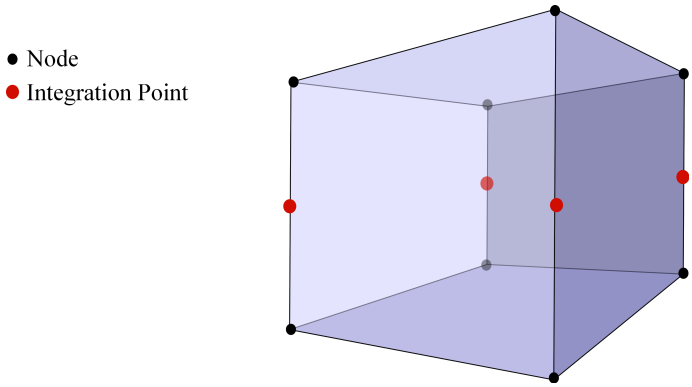

Figure 4.2: *COH3D8* element

4.2 Finite elements model

The CZM fatigue debonding model was tested on various joint geometries characterized by different mixed mode ratios, in order to verify accuracy, robustness and performance in terms of computational time. In particular, pure mode I loading was simulated with a Double Cantilever Beam (DCB) geometry, pure mode II loading with an End Loaded Split (ELS) geometry and mixed mode I/II loading with a Mixed Mode End Loaded Split (MMELS) geometry and a Single Lap Joint (see Figure 3.11). The applied force and the specimens dimensions are given in Table 4.1.

In order to investigate the model sensitivity to material behavior, two kind of materials were simulated, one representing an elastic, isotropic aluminum alloy ($E = 70$GPa; $\nu = 0.3$) and another one an elastic, orthotropic composite laminate (see. Table 3.2). In all the simulations a load ratio R = 0 is assumed. The adherend were meshed with 3D *Continuum Shell* elements. From a modeling point of view continuum shell elements look like three-dimensional continuum solids, but their kinematic and constitutive behavior is similar to conventional shell elements. For example, conventional shell elements have displacement and rotational degrees of freedom, while continuum solid elements

	Aluminum Joints			Composite Joints		
	DCB	ELS	MMELS	DCB	ELS	MMELS
$P\,[N/mm]$	10	25	20	10	20	15
$a_0\,[mm]$	20	20	20	20	20	20
$h\,[mm]$	5	5	5	5	5	5
$L\,[mm]$	175	175	175	175	175	175
$b^*\,[mm]$	20	20	20	20	20	20

* b: specimens width

Table 4.1: Specimens dimension and applied load

and continuum shell elements have only displacement degrees of freedom. Continuum shell elements allow for: thickness tapering, a more accurate contact modeling than conventional shells (they take into account two-sided contact and thickness changes) and stacking (they capture more accurately the through-thickness response for composite laminate structures). All specimen geometries have been modelled as a cmbination of two bonded cantilever beams in the "Assembly Module". In order to achieve this, a single cantilever beam was modelled in the "Part Module" and was partitioned for the definition of the loading point. Further the material properties were defined and this part was assigned a composite stack by using the *Composite Layup* option for Continuum Shell elements in the "Property Module". In this option local coordinate systems are also defined for assigning the shell normal and the ply orientations. The final composite can be viewed by "Ply-stack plot" sub-option in the "Query information" "Property Module" (see Figure 4.3).

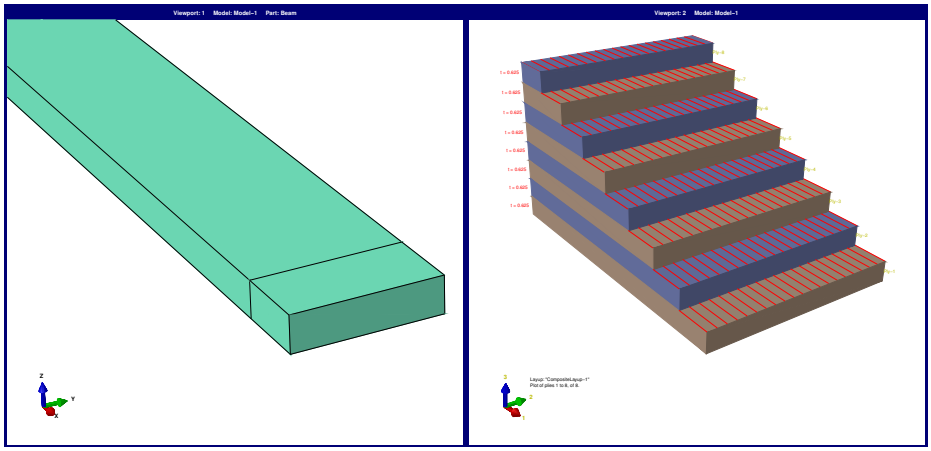

Figure 4.3: *Composite Layup* definition

A structured sweep mesh of continuum shell elements *SC8R* with an element size of 1 *mm* was introduced with single element in thickness. During the definition of the sweep mesh the element normal should be carefully selected in such a way that the direction of the element normal coincides with the direction of the element normal declared in the *Composite Layup* section in the "Property Module". Therefore, the normals, for both the parts forming a joint, are directed away from each other from the interface.

The cohesive elements were kinematically tied to the two delaminating halves. The cohesive element size was 0.5 *mm* (CZM). The continuum shell and cohesive element dimensions have been chosen in order to keep computational time within a reasonable value. The maximum damage increment was taken $\Delta D_{max} = 0.2$, based on the sensitivity analysis done in [65].

4.3 Results

The 3D model performance is compared with the 2D version concerning the value of G as a function of crack length. Due to crack front bowing (Figure 4.4), the average G (or G_I, G_{II}) and crack length along the crack front were considered for the comparison with the 2D model. In the case of elastic, isotropic material parts, analytical solutions for G (Mode I [16], Mode II [74] and Mixed/Mode I/II [75]) were also introduced in the comparison; while in the case of the elastic, orthotropic composite only the value of G obtained by VCCT simulations, made by our colleagues from Politecnico di Milano (see section 3.4), were considered. Additionally, Eq. (2.3) is integrated numerically using the G versus crack length coming from the analysis instead of taking directly the output number of cycles. The reason is that, as the CZM process zone needs some time to get to a steady state while VCCT does not, the G calculated by CZM may be rather different in the first millimeters of propagation yielding a different number of cycles. For this reason, a comparison with experiments is foreseen as a further validation step, while at the moment the paper focuses on the comparison of numerical results of the two model after the transient phase of process zone formation.

In Figure 4.4, the crack front, at a generic increment of a fatigue simulation in the case of Mode I Loading, is depicted. It can be noticed both fully damaged element ($D = 1$) and damaged element ($0 < D < 1$) that forms the process zone, A_{CZ}. In the Figure 4.4 one of the two adherends is hidden to see the damage distribution of the cohesive zone.

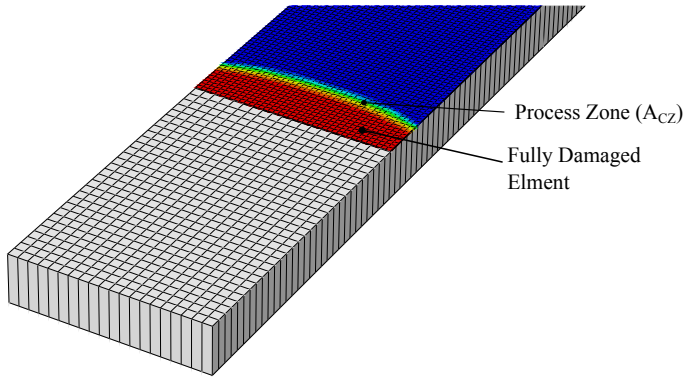

Figure 4.4: Crack front during a fatigue simulation

Regarding the calculation time, the time the analyst has to wait for the crack to reach the knee of the a–N diagram, that is close to fracture, was monitored. In the cases examined, this means a crack length of 30mm for all the geometries except SLJ, for which the analyzes were stopped at 10mm of crack length even though still far from

fracture. Only the outputs strictly necessary for each model were required, in order to minimize time spent in storing data. The PC used for calculations for CZM was an Intel1 CoreTM I, 2630QM 2 GHz CPU, with 6GB RAM and 579 Gb HD (7200 rpm, 6MB cache), while for VCCT it was an Intel1 XeonTM E5645 (Nehalem, 1 core) 2.4 GHz CPU, with 48GB RAM and 900 Gb HD (10 k rpm, 12.3MB cache).

4.3.1 Mode I loading

In the case of aluminum joints, the four models show the same overall trend and an overall good correspondence with each other of the SERR plot (see Figure 4.5.a); in general the VCCT yields slightly lower values than the two CZM and analytical model. Moreover both the CZMs show a quite different trend in the first millimeter, where the process zone is under development. The average difference between the VCCT and the CZMs is about 5% on the 21-29 mm crack length span, while the difference is in the order of 2% whit respect to the analytic solution. As a consequence, the crack growth predictions given by the CZMs are rather similar to that given by the analytical model (Figure 4.5.b). Due to the differences shown in the SERR plot, the VCCT model gives a slight under-prediction of the crack growth rate with respect to the CZMs and analytical model. It is believed that further mesh refinement can get the two models closer to each other.

Moving to the analysis of composite joints, the presence of an anisotropic behavior of the adherends increases the difference between the three models. In particular, for the strain energy release rate evaluation, the trends of the CZMs are more scattered (Figure 4.6.a): this in due to the combination of adherends anisotropy and stepwise element deletion.

However a good agreement can be noticed for the three plots, although the CZM - 3D curve is slightly lower that the other (differences in the order of 12%). These differences produce a significant under prediction of the crack growth rate in the case of CZM - 3D with respect to the CZM - 2D and VCCT (Figure 4.6.b).

4.3.2 Mode II loading

Figure 4.7.a shows the values of G_{II} obtained by CZMs, VCCT and the analytical mode in the case of aluminum substrates. Again as in the case of DCB, the four sets show a good overall correspondence with each other.

Some differences concern the CZM - 2D, that gives a trend slightly lower than the other models, and the VCCT, whose trend is rather jagged: probably this is related to a non-uniform (one row of elements per time of increment) crack front propagation that has been recorded in the simulation.

The main result in terms of crack length vs. number of cycles is shown instead in Fig. 4.7.b, where a difference comes out lower than mode I (18% at 39-mm crack length), and also in this case a further mesh refinement can get the two models closer to each other.

In Figure 4.8 the crack front during a ELS fatigue simulation is shown. It can be seen how the front appears stighter than the one of a DCB fatigue simulation.

In the case of composite adherend the three modes analyzed are again in good agreement between each other. Concerning the strain energy release rate plot (Figure 4.9.a), the CZM - 3D trend is quite lower than the other; however the differences are, in the average, lower than 7%. In terms of crack length vs. number of cycles prediction (Figure

4.9.b), this produce similar results for CZM - 2D and VCCT, while the CZM - 3D yields a higher fatigue life with respect to the others (about 55 % for a propagation from 22 to 36 *mm*). The strain energy release rate plot of mode II composite joints appear less scattered with respect to the mode I composite joints: this is due to the lower stress concentration in the ELS joints (respect to the DCB), which produce smaller changes of the stress fields when one or more elements change from "undamaged" to "damaged".

4.3.3 Mixed-Mode I/II loading

Fig. 4.10.a shows the values of G_{TOT} ($G_{TOT} = G_I + G_{II}$) obtained again by CZMs, VCCT and analytical model for the aluminum joint. The values obtained with the four methods in this case highlight a little bit the differences found for the single modes: the CZM - 3D trend is almost superimposed to the VCCT trend (1 % average difference from 21 to 30 *mm* crack length), while the analytical solution gives a slight overestimation and CZM - 2D a slight underestimation with respect to the previous ones. The mode separation *(G_I* and *G_{II})* is shown in Figure 4.10.b only for CZM - 3D and VCCT - 3D. The values obtained with the two methods in this case highlight a little bit the differences found for the single modes (see previous paragraphs).

These differences become larger in the crack length vs. number of cycles plot (Figure 4.11.a), where again CZM - 3D and VCCT give similar results, while analytical solution and the CZM - 2D give respectively higher and lower crack growth rate. Figure 4.11.b shows the variation of the mixed mode ratio(MM) during the propagation.

In the case of composite joints the three models give quite different results: although the trends of the total strain energy release rate ($G_{TOT} = G_I + G_{II}$) are similar (Figure 4.12.a), the mode separation produces differences of the mixed mode ratio in order of 30 % (Figure 4.13.b), and this, in turn, produces significant differences in terms of crack length vs. number of cycles prediction (Figure 4.13.a). This phenomenon, still under investigation, is thought to be produced by the material anisotropy.

4.3.4 Mixed-Mode I/II loading

Figures 4.14.a - 4.14.b show the values of G_I and G_{II} obtained by CZM and VCCT. Concerning the comparison of the single modes, the values are closer to each other than in the case of MMELS, except the first 3 mm, necessary to establish a steady state process zone in CZM. After this, the total G is the same and so also the mixed-mode ratio (2.5% average difference from 3- to 10 *mm* crack length). With these premises, the crack length vs. number of cycles in Fig. 4.15.a, skipping the first millimeter of propagation, the values are practically coincident (4.5% difference at 10 *mm* crack length).

Regarding the composite assemblies Fig. 4.16 shows the distribution of G_I, G_{II} and G_{III} along crack front. It is clear that values are unevenly distributed probably due to the development of an asymmetrical crack front. It is also evident that where G_I, G_{II} values drop, a comparable G_{III} shows up. Since Mode III should be concentrated in correspondence of the surfaces, the occurrence of non-negligible G_{III} at some points in the interior is peculiar. Regarding the crack front in the CZM simulation, it appears symmetric at any increment; since SERR is an output unavailable in CZM model, in Figure 4.17 the damage distribution and stress condition along the front are shown.

Keeping in mind that this results may affect the comparison with CZM, the values of G_I and G_{II} obtained by CZM and VCCT are reported in Fig. 4.18.b. The two sets show quite a good correspondence anyway with each other concerning G_{II}, being CZM in

this case higher than VCCT after about 5mm of crack growth. The Mode I component instead, results lower than VCCT more markedly than in the case of DCB, and differently from the case of MMELS, which is probably related to the uneven distribution shown in Fig. 4.16. The very low values in the case of CZM at the beginning are related instead to the absence of an initial crack and, therefore, the necessity of some millimeters of crack growth for the process zone to develop. Oscillations visible afterwards are instead related to the relatively coarse mesh used to keep calculation time within affordable limits. As already said in the case of MMELS, a general statement whether CZM under- or overpredict the strain energy release rate outcoming from VCCT cannot be drawn, unless further investigations, especially concerning mesh size effects, are done. Skipping the first five millimeters where the cohesive process zone develops, the crack length vs. number of cycles is shown in Fig. 4.19.b. Given the differences shown in Fig. 4.18 in the values of G_I and G_{II} between the two models, a sensible difference in the elapsed number of cycles for a given crack growth obviously turns out.

4.4 Calculation time

The calculation times are reported in Tab. 4.2. The CZM results on average two-order of magnitude quicker than VCCT, with calculation times of the order of minutes instead of hours. In the case of SLJ, the increase in calculation time is related to the finer mesh, but the time required by VCCT is becoming so important that high performance computing may be needed if the model complexity would increase further.

	DCB	ELS	MMELS	SLJ
CZM	186	54	90	57
VCCT	1012	86	229	1015

Table 4.2: Calculation time of VCCT and CZM (time is reported in *minutes*)

4.5 Conclusions

The comparison of the performances of the cohesive zone model presented in [76] and the Virtual Crack Closure Technique (VCCT) embedded in the software Abaqus on mode I, mode II and mixed-mode I/II loaded cracks in composite assemblies yielded the following results:

- the two models are in good agreement concerning Mode I and Mode II conditions and also under Mixed-Mode I/II loading concerning the total $G_{TOT} = G_I + G_{II}$. However, as the crack growth rate (Eq. 2.3) is strongly dependent on ΔG, even a limited difference causes a sensible difference in the elapsed number of cycles for a given crack growth. Since the element size is a compromise between the computation time and a simulation with sufficient detail, by just decreasing it a better agreement would be found. Hence, a general statement whether CZM under- or overpredict the strain energy release rate outcoming from VCCT cannot be drawn, unless further investigations, especially concerning mesh size effects, are done.

- while the modeling effort is a bit higher (need of introducing a layer of cohesive elements), CZM results of easier use (no need to identify the proper number of Fourier terms and time increment to represent cyclic loading). At the same time, it results more efficient as the computation is 1-2 order of magnitude faster, even though run on a less powerful PC. As mentioned in the previous chapter, Direct Cyclic procedure is computationally more expensive than the in-house CZ subroutine.

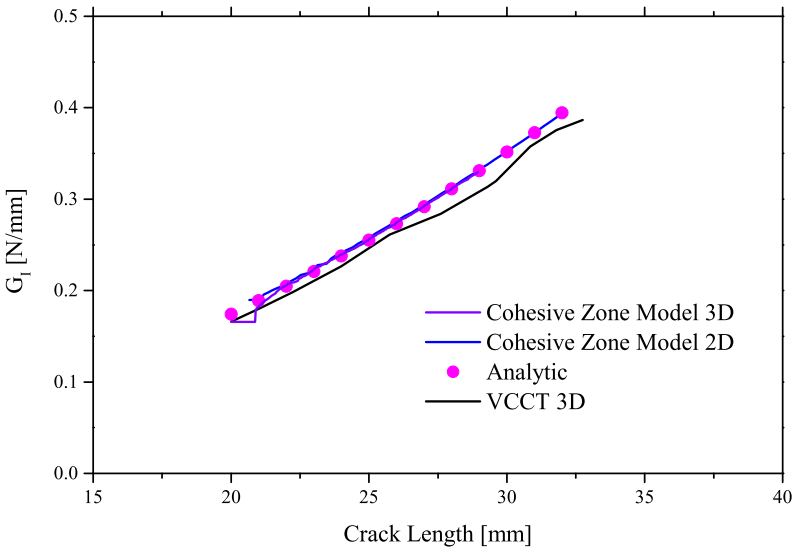

(a) Comparison of a – G_I values

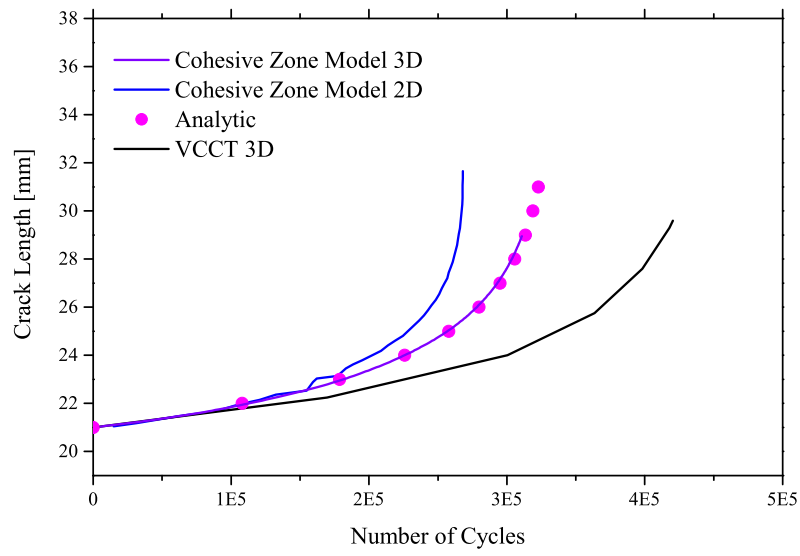

(b) Comparison of a - N values

Figure 4.5: CZM 3D results compared with CZM 2D, VCCT 3D and analyitic ones (DCB, isotropic material)

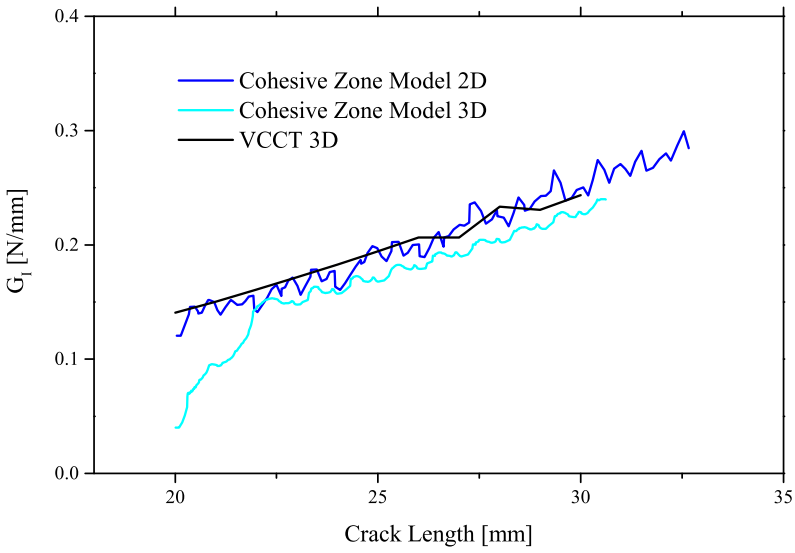

(a) Comparison of a – G_I values

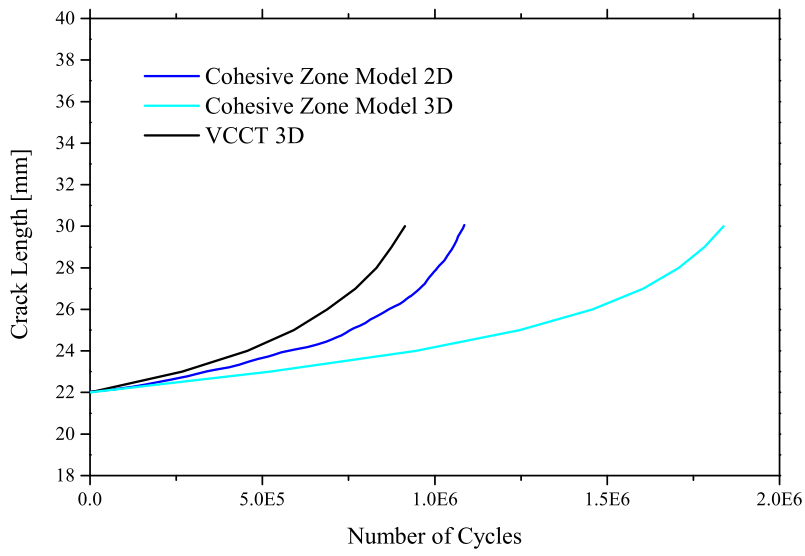

(b) Comparison of a - N values

Figure 4.6: CZM 3D results compared with CZM 2D, VCCT 3D and analyitic ones (DCB, orthotropic material)

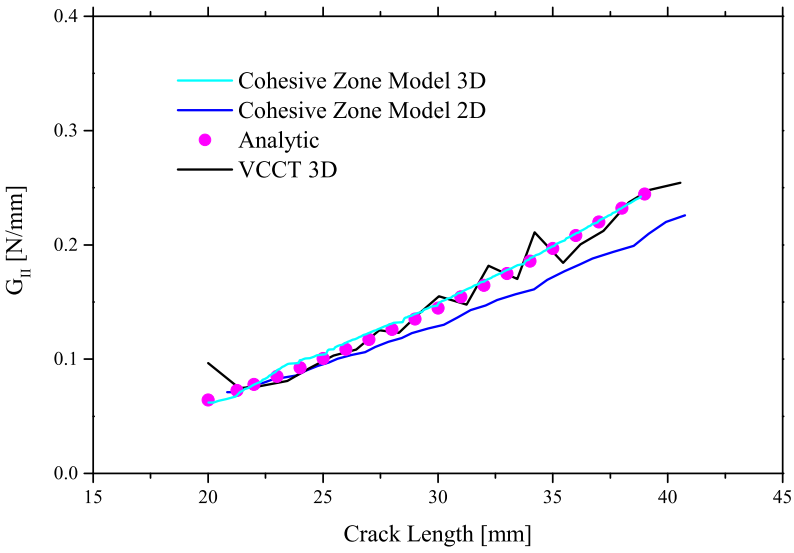

(a) Comparison of a – G_{II} values

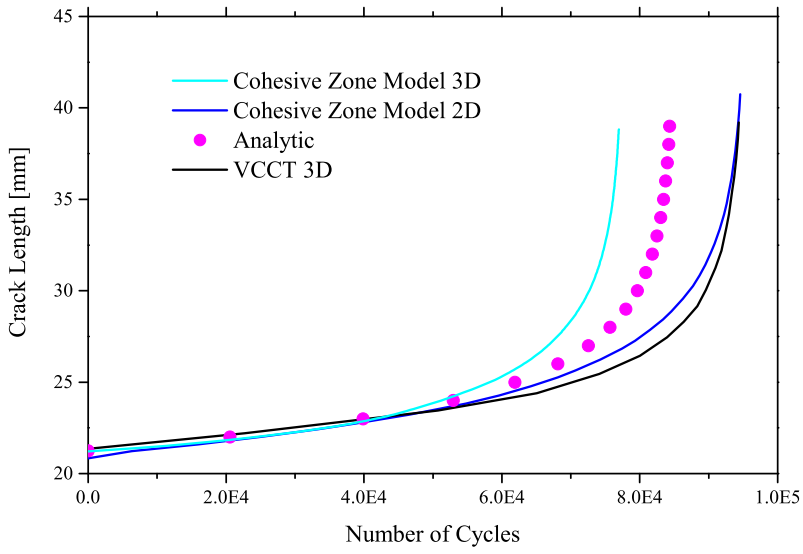

(b) Comparison of a - N values

Figure 4.7: CZM 3D results compared with CZM 2D, VCCT 3D and analytic ones (ELS, isotropic material)

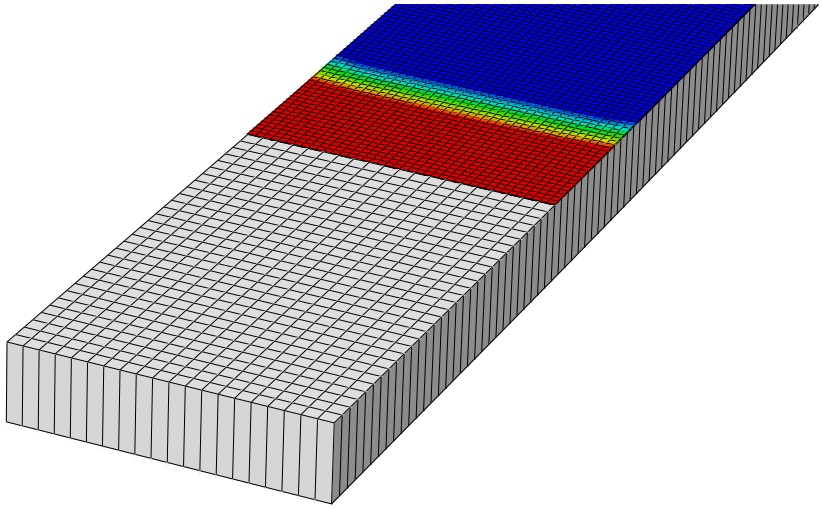

Figure 4.8: Crack front during an ELS fatigue simulation

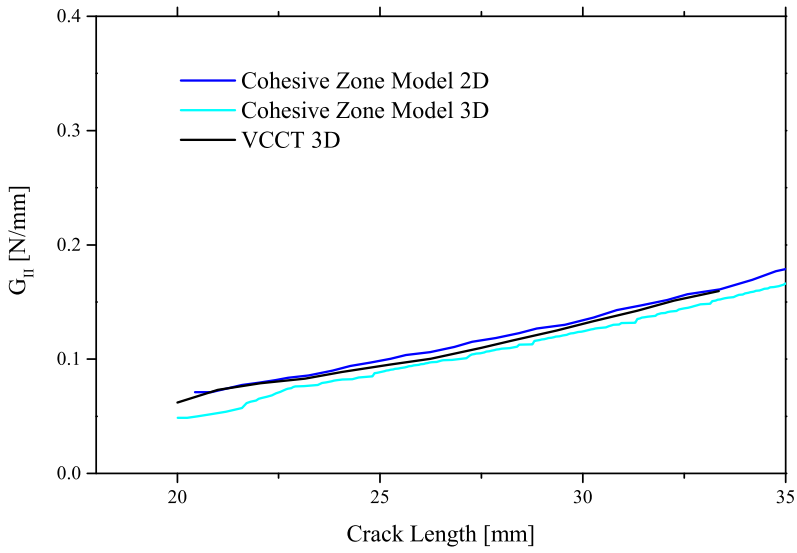

(a) Comparison of a - G_{II} values

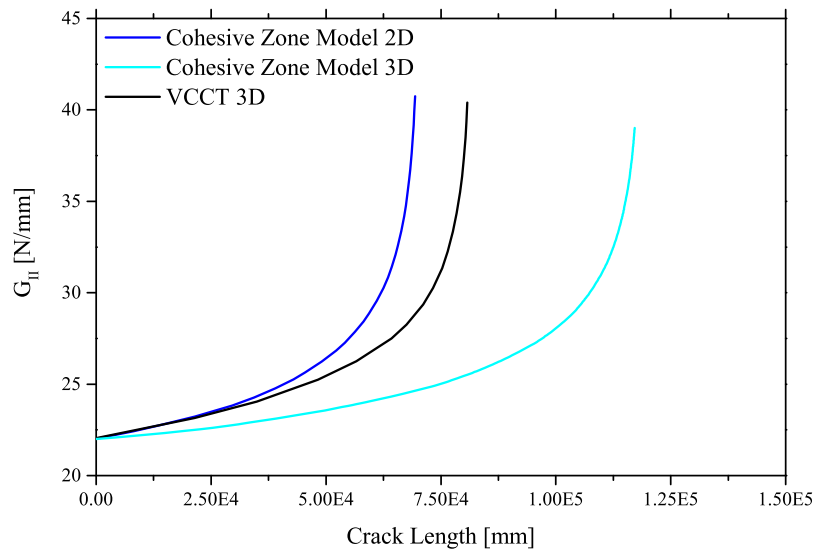

(b) Comparison of a - N values

Figure 4.9: CZM 3D results compared with CZM 2D, VCCT 3D and analyitic ones (ELS, orthotropic material)

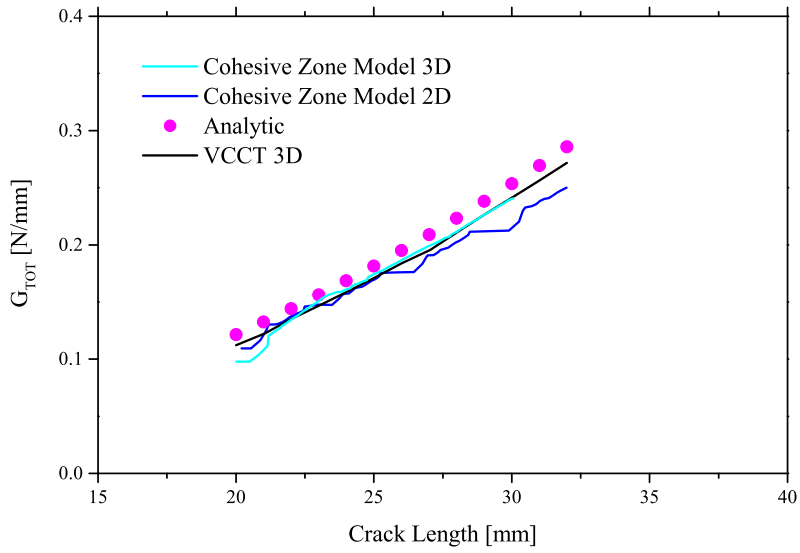

(a) Comparison of a – G_{TOT} values

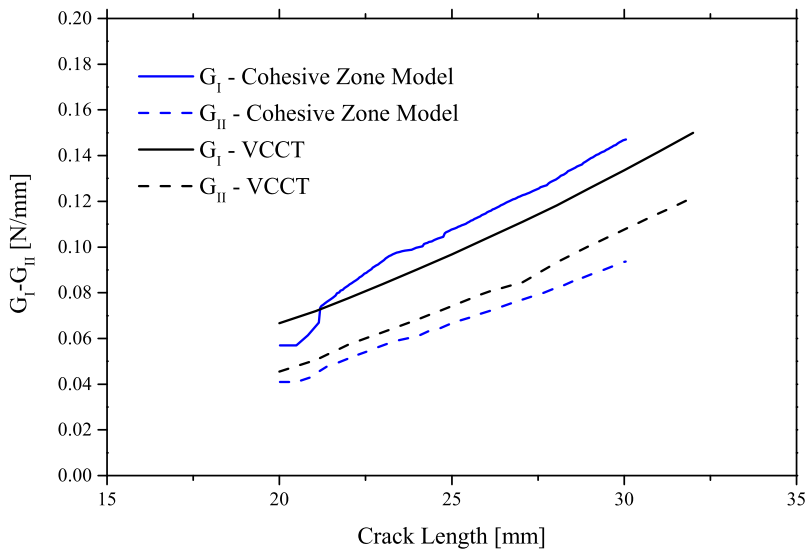

(b) Comparison of a – G_I /G_{II} values

Figure 4.10: Comparison of G_I , G_{II} *and* G_{TOT} trends (MMELS, isotropic material)

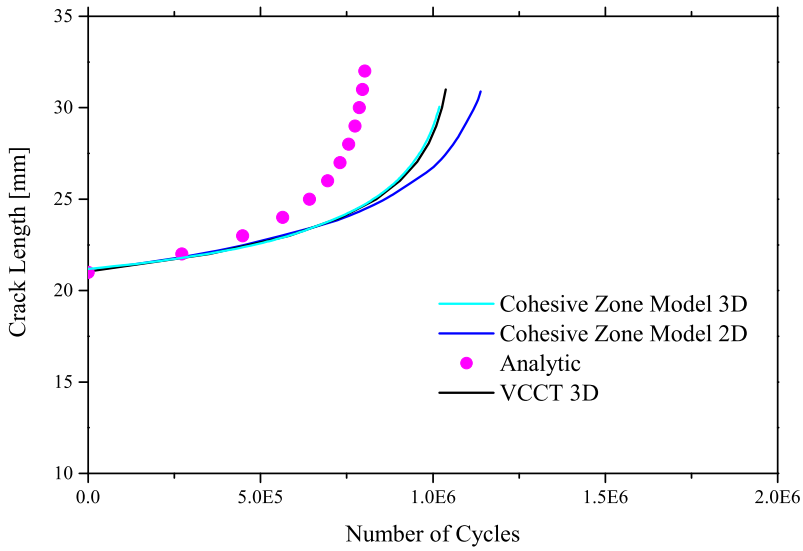

(a) Comparison of a – N values

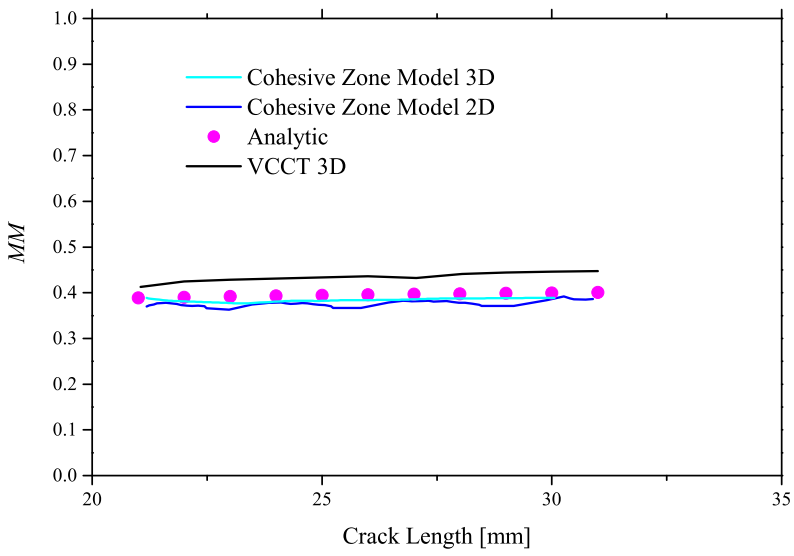

(b) Comparison of a – MM values

Figure 4.11: Comparison of N *and* MM trends (MMELS, isotropic material)

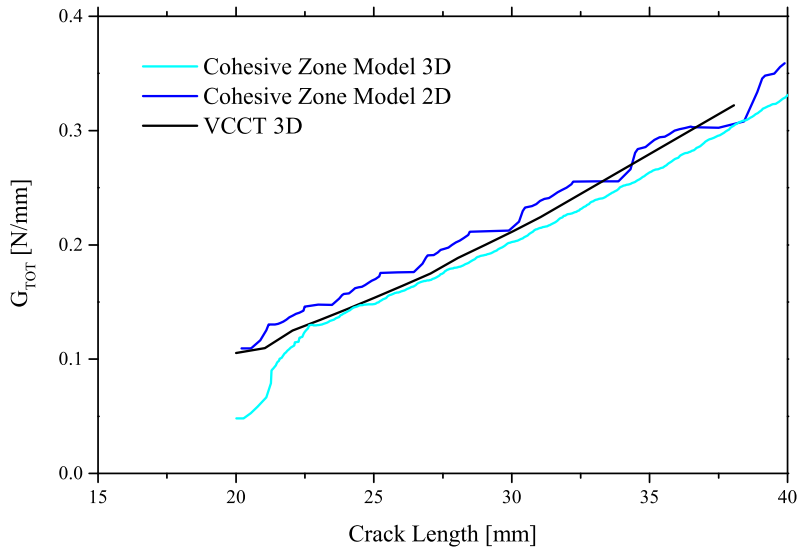

(a) Comparison of a – G_{TOT} values

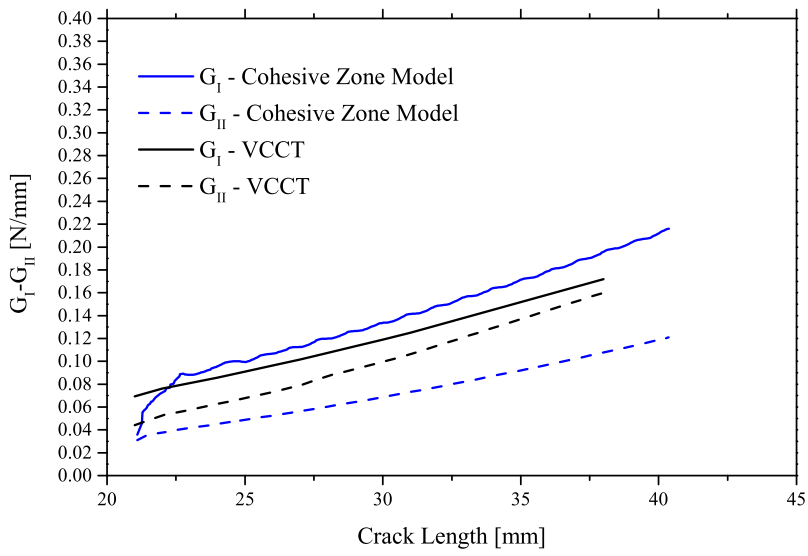

(b) Comparison of a – G_I /G_{II} values

Figure 4.12: Comparison of G_I , G_{II} *and* G_{TOT} trends (MMELS, orthotropic material)

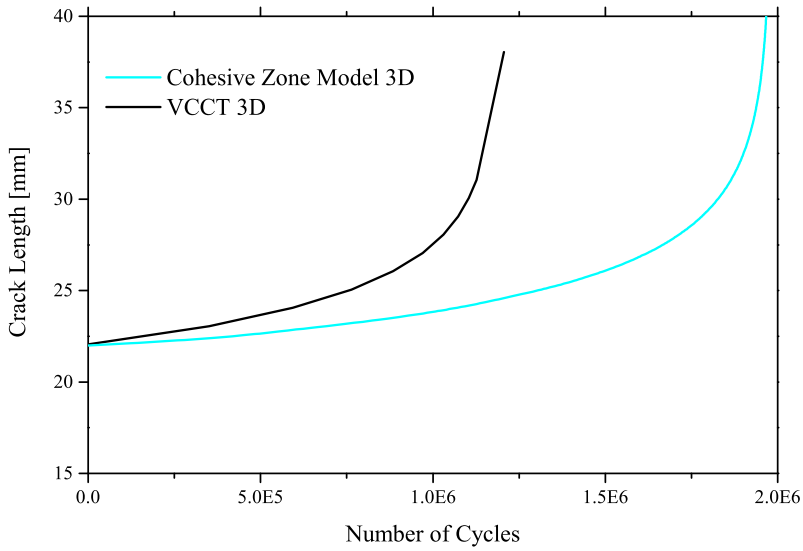

(a) Comparison of a – N values

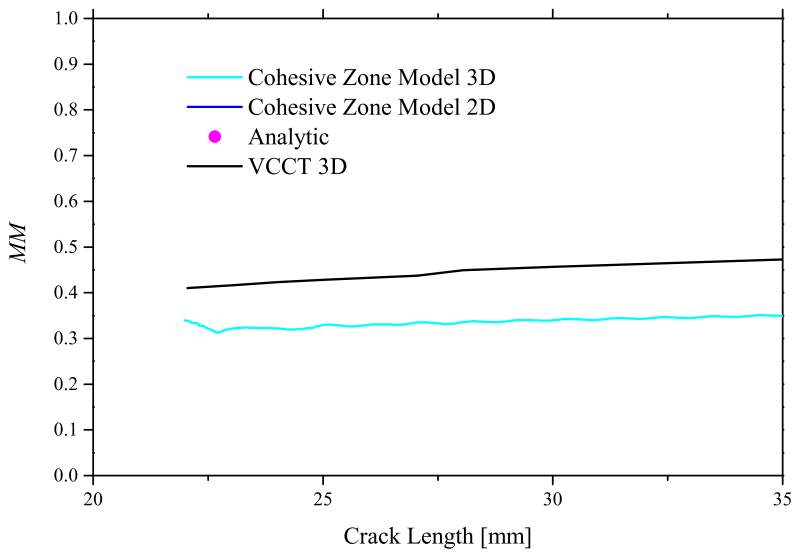

(b) Comparison of a – MM values

Figure 4.13: Comparison of N *and* MM trends (MMELS, orthotropic material)

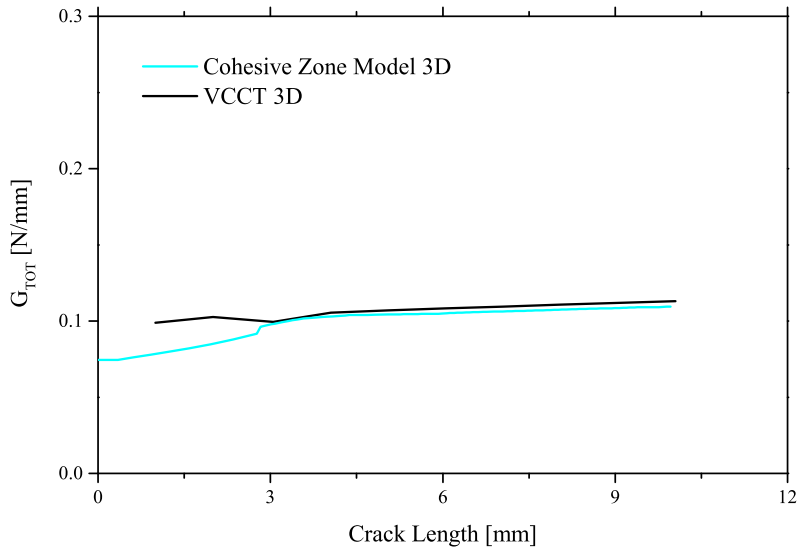

(a) Comparison of a – G_{TOT} values

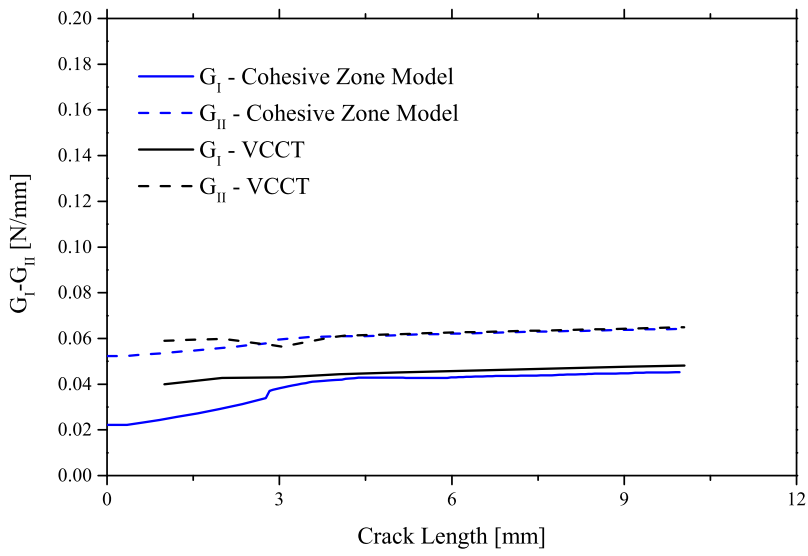

(b) Comparison of a – G_I /G_{II} values

Figure 4.14: Comparison of G_I , G_{II} *and* G_{TOT} trends (SLJ, isotropic material)

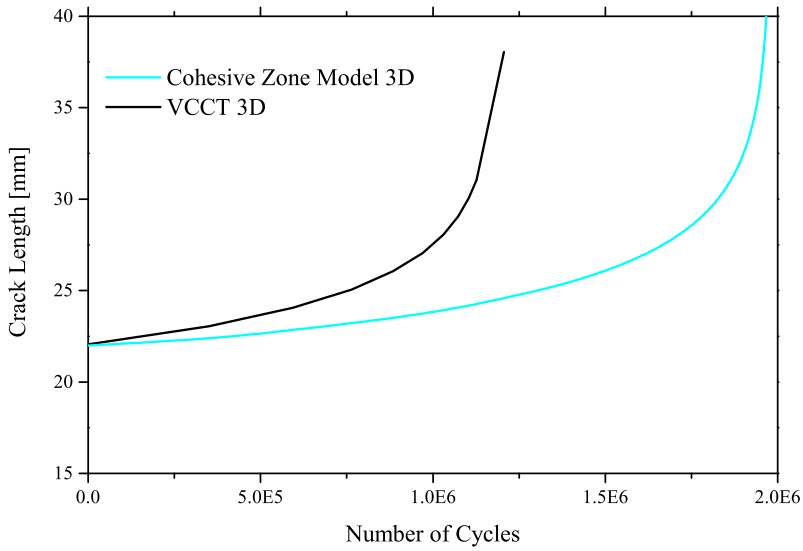

(a) Comparison of a – N values

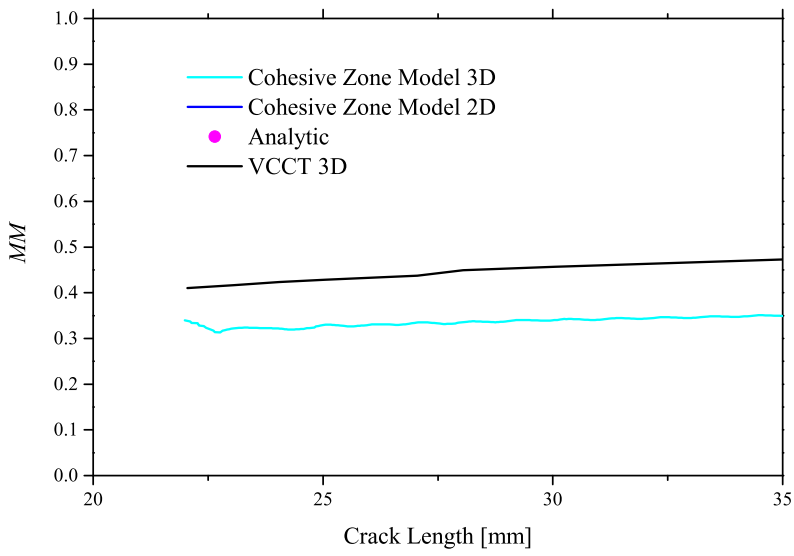

(b) Comparison of a – MM values

Figure 4.15: Comparison of N and MM ratio trends (SLJ, isotropic material)

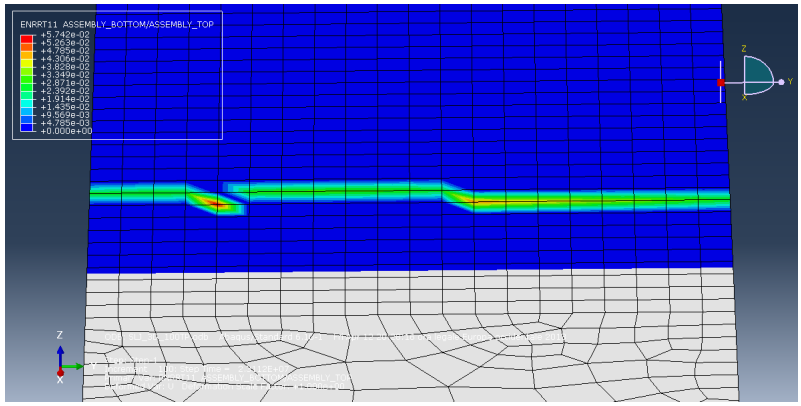

(a) G_I distribution

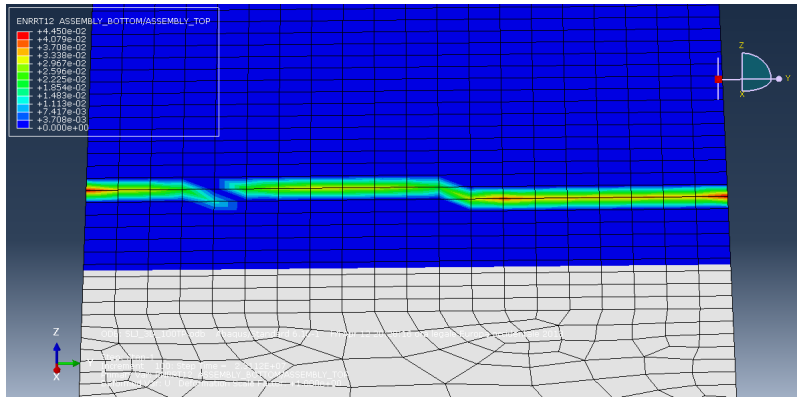

(b) G_{II} distribution

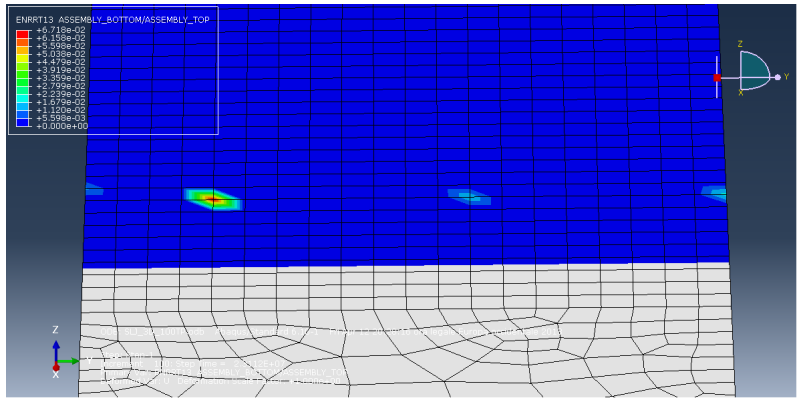

(c) G_{III} distribution

Figure 4.16: Example of G_I, G_{II} and G_{III} distribution along the crack front in thr VCCT simulations [77]

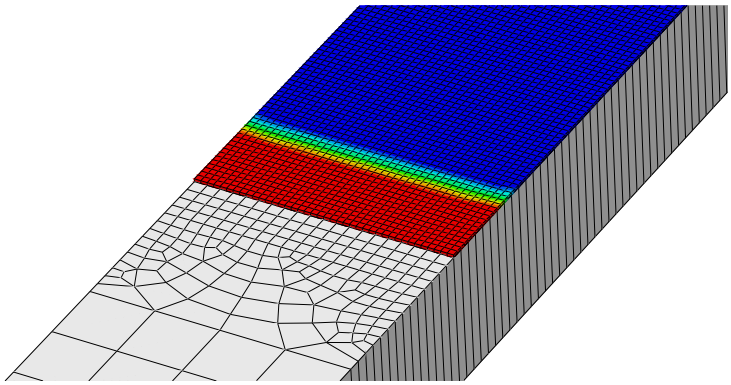

(a) Damage distribution in Cohesive Zone

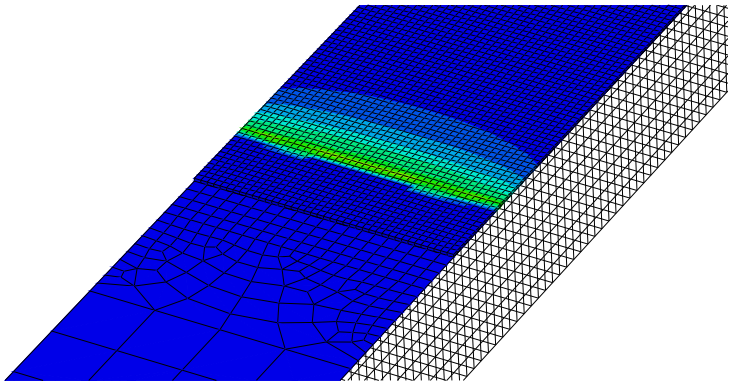

(b) Opening stress (s_{33}) distribution in Cohesive Zone

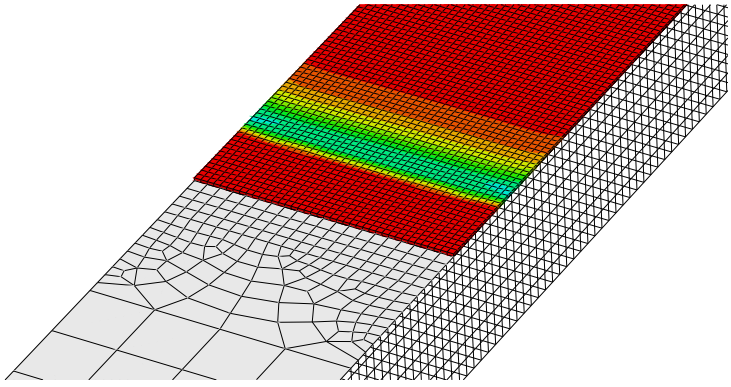

(c) In-plane shear stress (s_{13}) distribution in Cohesive Zone

Figure 4.17: Crack front in CZM - 3D fatigue simulations

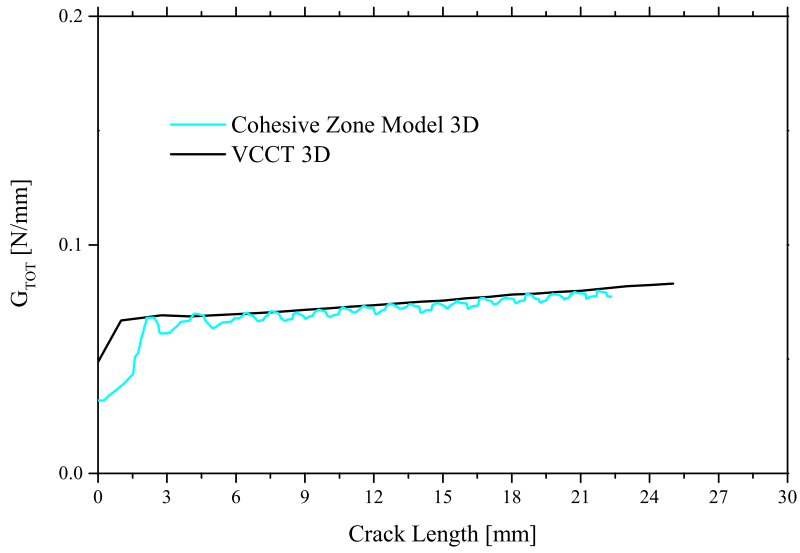

(a) Comparison of a – G_{TOT} values

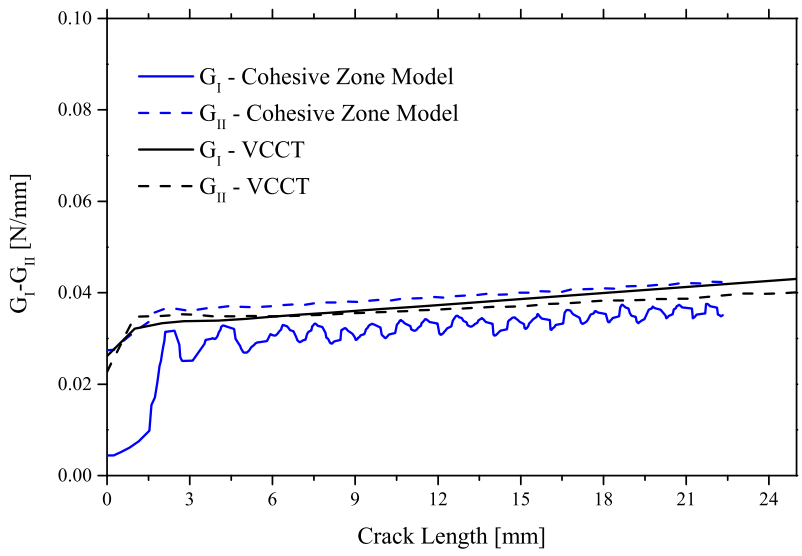

(b) Comparison of a – G_I /G_{II} values

Figure 4.18: Comparison of G_I , G_{II} *and* G_{TOT} trends (SLJ, orthotropic material)

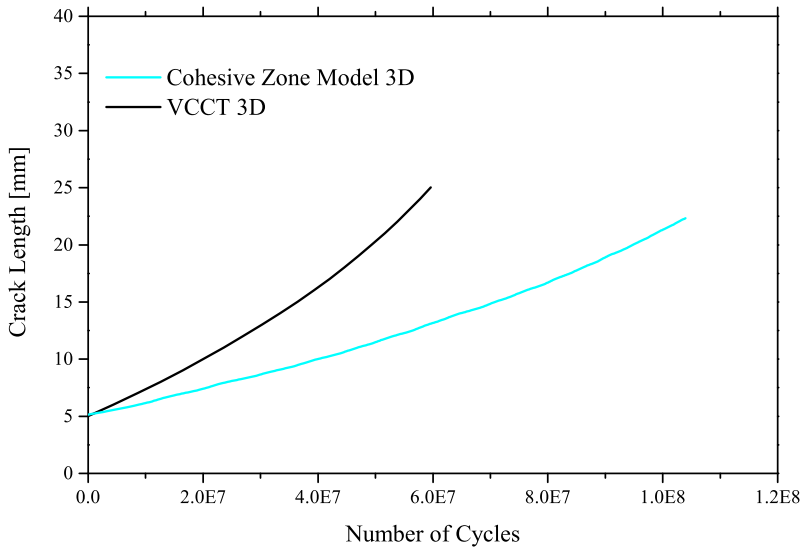

(a) Comparison of a – N values

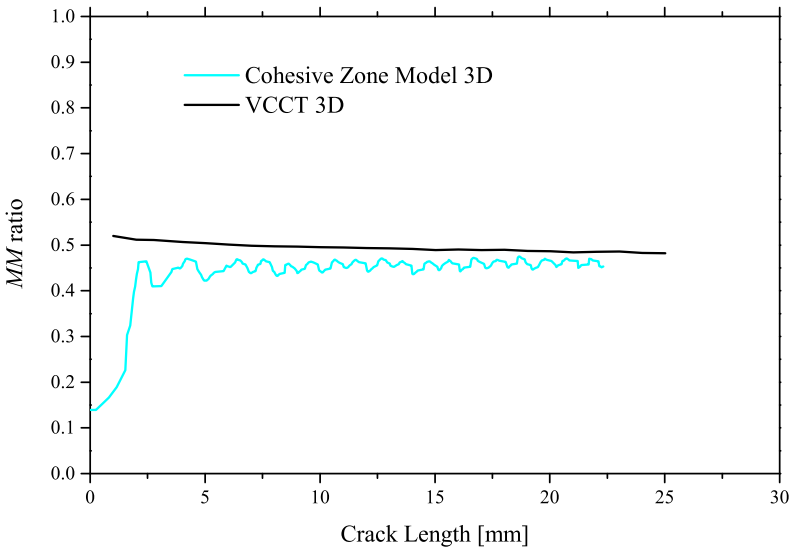

(b) Comparison of a – MM values

Figure 4.19: Comparison of N and MM ratio trends (SLJ, orthotropic material)

Chapter 5

Development of CZM for three-dimensional fatigue debonding of adhesive joints with general shape cracks

5.1 Crack front identification

In Chapter 3 a model of the cohesive zone able to correctly simulate the propagation of fatigue defects in two dimensional geometry was described. The procedure has been implemented in the finite element solver (*Abaqus*) by programming the appropriate software-embedded subroutines. Part of the procedure targets the calculation of the strain energy release rate, G, which is necessary to calculate the growth of the defect. The procedure has been also extended to 3D geometries, where G could be evaluated by the contour-integral on parallel slices along the crack front.

However the two models described are able to simulate and predict the joint life only in case the crack is almost straight during all the fatigue simulation. For that reason it was possible to validate the CZM - 3D using averaged SERR value along the front. In fact if the initial crack front is not straight, the CZ models are not able to simulate the propagation. Therefore a new CZM approach capable of managing crack propagation without caring of the front form or its evolution was needed. In the 3D model presented in the previous chapter, it has been assumed that each slice presents a straight local crack front during the fatigue simulation. Consequently the path perpendicular to the crack front, along which the J-integral must be computed, corresponds to a row of cohesive elements. In order to generalize the model, it is necessary that the routine at each increment identifies the correct shape of the crack (see Figure 5.1) and the direction perpendicular to the delamination front in each node. The flow diagram (shown in Figure 3.5) to evaluate the damage distribution at each increment was still implemented in the new model, but integrated to find the crack shape.

Inspired by Xie and Biggers [78] who proposed a procedure to allow the determination of the actual shape of the delamination front within the VCCT, the routine looks for integration points having at the same time:

- $D < 1$;
- at least one surrounding point with $D = 1$

The segments that separate the points with $D < 1$ from the points with $D = 1$define the crack front (see Figure 5.2). Through the perpendicular lines n_1 and n_2 respectively to the segments, *1* and *2*, the direction of the local crack propagation is identified (the vector n in Figure 5.2). Once the front is defined, at each point the strain energy release rate is evaluated through the J-integral (where also Mode III can be taken into account) along the direction of propagation. However, further clarifications will be given in the reminder.

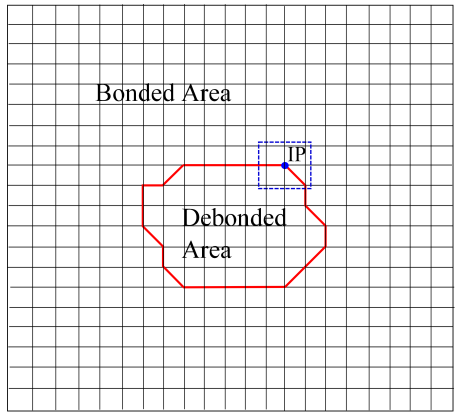

Figure 5.1: Crack front of generic shape

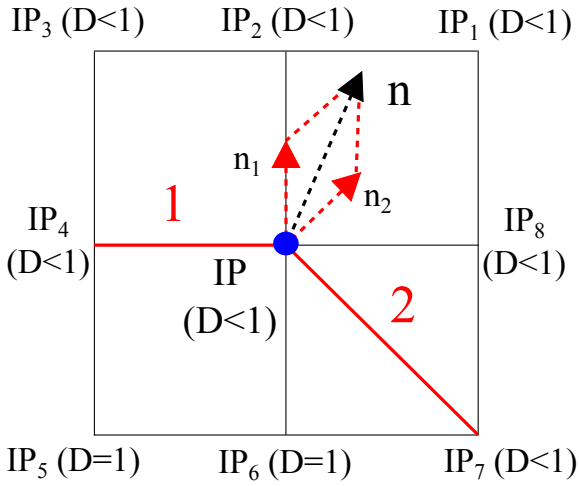

Figure 5.2: Identification of local crack front at integration point IP

In the 3D CZ model presented in the previous chapter the J-integral was evaluated using stress and strain extracted at integration point; this was possible because the path perpendicular to the front that was assumed straight at each incrment. In this model

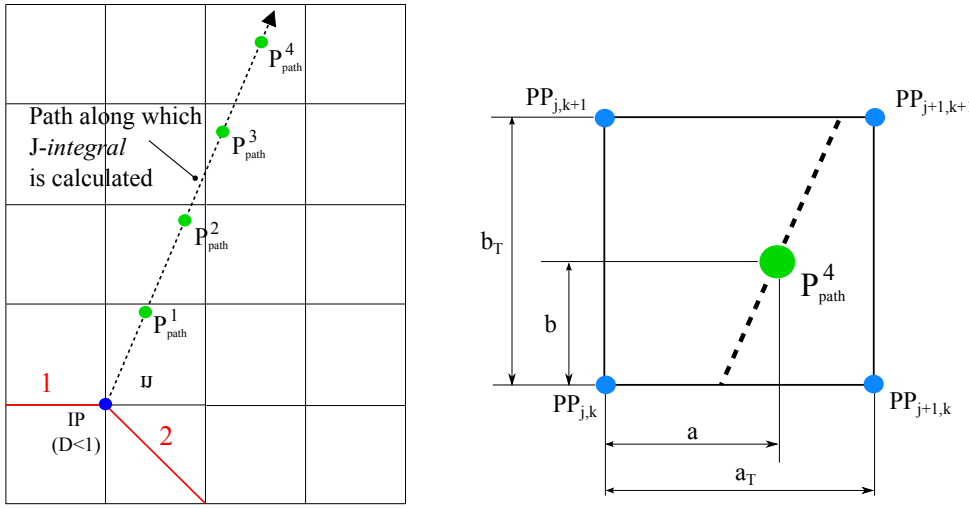

Figure 5.3: Path for evaluating the J-integral (left) and the bi-linear interpolation

a condition as the one described in picture at right of Figure 5.3 can now be managed. In fact the J-integral was evaluated using stresses and opening probed in P^r_{path}; in turn their stress conditions depend on their surrounding integration points.

Therefore, using the bi-linear interpolation, for any variable in P^r_{path}, q, it can be written:

$$q = (1-v)\cdot(1-u)\cdot q_{j,k} + v\cdot(1-u)\cdot q_{j+1,k} + v\cdot u\cdot q_{j+1,k+1} + (1-v)\cdot u\cdot q_{j,k+1} \quad (5.1)$$

where $v = a/a_T$, $u = b/b_T$, j *and* k are subscripts referred to four surrounding integration points (see Figure 5.3).

With regard to the J-integral computation, the Eq. (3.16) should be modified to consider the Mode III loading [79]:

$$J = \int_{\Pi} \left(-\sigma_{12}\frac{\partial u_1}{\partial x_1} - \sigma_{22}\frac{\partial u_2}{\partial x_1} - \sigma_{32}\frac{\partial u_3}{\partial x_1} \right) ds \quad (5.2)$$

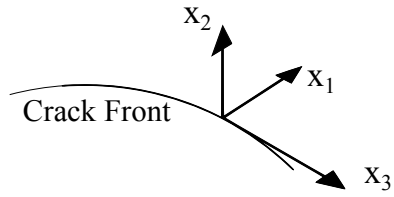

Figure 5.4: Definition of the local coordinate systems for a crack front point

Figure 5.4 can help explaining that the Eq. (5.2) must be evaluated in a local coordinate system for each crack front point. For this reason the output from *Abaqus*, that are referred in a global coordinate systems, must be converted to local ones.

After doing that for each crack, the strain energy release rate will be known. Further it will be possible to calculate ΔD_i^j and ΔN_{min}^j following the same algorithm described in Figure 3.5. The minimum number of cycles can this time be used to update the damage distribution of the crack front point only.

5.2 Mixed-Mode loading (I/II/III)

In order to obtain a comprehensive generalization of the new approach, also Mode III loading needs to considered. Therefore, a general formulation for decohesion elements dealing with mixed-mode delamination onset and propagation is required. As mentioned before, under pure Mode I, II or III loading, the onset of damage at the interface can be determined simply by comparing the traction components with their respective allowables. However, under mixed-mode loading damage onset and the corresponding softening behavior may occur before any of the traction components involved reaches their respective allowable. That is usually neglected in the formulation of decohesion elements. Instead it is assumed that the initiation of the softening process can be predicted using the quadratic failure criterion [81]:

$$\left(\frac{\sigma_{22}}{\sigma_{22max}^0}\right)^2 + \left(\frac{\sigma_{12}}{\sigma_{12max}^0}\right)^2 + \left(\frac{\sigma_{23}}{\sigma_{23max}^0}\right)^2 = 1 \tag{5.3}$$

The total mixed-mode relative displacement δ_{eq} is defined as:

$$\delta_{eq} = \sqrt{\left(\frac{\delta_{22} + \mid \delta_{22} \mid}{2}\right)^2 + (\delta_{shear})^2} \tag{5.4}$$

where $\delta_{shear} = \sqrt{\delta_{12}^2 + \delta_{23}^2}$ represents the norm of the vector defining the tangential relative displacements of the element. Assuming $\sigma_{12max}^0 = \sigma_{23max}^0$, it follows $\delta_{12}^0 = \delta_{23}^0$ where the superscripts, *0,* indicate the onset of softening process. The mixed-mode relative displacement corresponding to the onset of softening, δ_m^0, becomes:

$$\delta_m^0 = \delta_{22}^0 \delta_{12}^0 \sqrt{\frac{1+\beta^2}{(\delta_{12}^0)^2 + (\beta \delta_{22}^0)^2}} \tag{5.5}$$

where $\beta = \delta_{shear}/\delta_{22}$.

The criteria used to predict delamination propagation under mixed-mode loading conditions are usually established in terms of energy release rates and fracture toughness. As said in the previous chapter, there are established test methods to obtain the Mode I and II interlaminar fracture toughness: the DCB is used for Mode I, the ENF or the ELS specimens are used for Mode II and for mixed-mode I/ II the Mixed-Mode Bending (MMB) test specimen is normally used. However, further research is required to assess the Mode III interlaminar fracture toughness, G_{IIIC}. Furthermore, a reliable mixed-mode delamination failure criterion incorporating Mode III is not yet available because there is no mixed-mode test method which incorporates Mode III loading. Therefore, most of the failure criteria proposed for delamination growth were established for mixed-mode I and II loading only. For the reason explained above, the concept of energy release rate related with shear loading, $G_{shear} = G_{II} + G_{III}$, will be used in the current work. An equivalent strain energy release rate can then be obtained modifying the Eq. (3.23):

$$G_{eqC} = G_{IC} + (G_{IIC} - G_{IC}) \left(\frac{G_{shear}}{G_T} \right)^{\eta} \tag{5.6}$$

with $G_T = G_I + G_{shear}$. The last parameter used to predict completely the delamination propagation is the mixed-mode displacements corresponding to total decohesion, δ_m^c:

$$\delta_m^c = \frac{2}{K\delta_m^0} \left[G_{IC} + (G_{IIC} - G_{IC}) \left(\frac{\beta^2}{1+\beta^2} \right)^{\eta} \right] \tag{5.7}$$

The parameter C and n (see Eq. (2.3)) can be obtained using (3.25) and (3.26) where this time the mixed mode ratio MM is:

$$MM = \frac{G_{II} + G_{III}}{G_I + G_{II} + G_{III}} \tag{5.8}$$

5.3 Results

The procedure described in this chapter has been validated so far only for aluminum joint in Mode I, Mode II and Mixed-Mode I-II. The specimens dimensions and the applied loads are the same of Tab. 4.1. The cohesive law parameters and Paris law equation coefficients are given in Table 3.3. A structured sweep mesh of continuum shell elements *SC8R* with an element size of 1 *mm* was introduced with single element in thickness, while the cohesive zone was modelled with *COH3D8* element of the size 0.2 *mm*.

The first ten millimeters of crack propagation in a DCB test have been simulated. In order to verify the accuracy of this approach, the strain energy release rate has been compared with the analytical solution (Krenk, 1992). The values of G_I obtained by 3D VCCT and planar cracks 3D CZM are plotted on the same diagram. As the 3D crack front is slightly bowed, the $G_I$and crack length are average values. All the sets show quite a good match (see Figure 5.5).

The crack front during the propagation is shown in Fig. 5.6. Figure 5.7 shows as the crack front appears if fully damaged element, colored in red, are deleted . Since the fatigue damage is assigned only to the crack front points, the cohesive elements behind the front can be damaged because their stress conditions are outside the cohesive law.

For what concerns the Mode II, ELS test is simulated with the generalized approach. Figure 5.8 shows results in terms of G_{II} against the VCCT and the planar cracks 3D CZM. Also in this case all sets show a good match.

Lastly in Figure 5.9 the comparison between the new approach results and the VCCT and CZM 3D are shown. The values obtained with the new approach in this case highlight the differences found for the single modes. Both $G_I$and G_{II}trends are lower than the other one.

Figure 5.10 shows the stress-opening values in various integration points, located at different crack length, during all the fatigue simulation. As one can note, the area underling the stress-opening values grows with increasing distance of Integration point from the initial crack tip. Obviously this depends on the fact that strain energy release rate increases with the length of the crack.

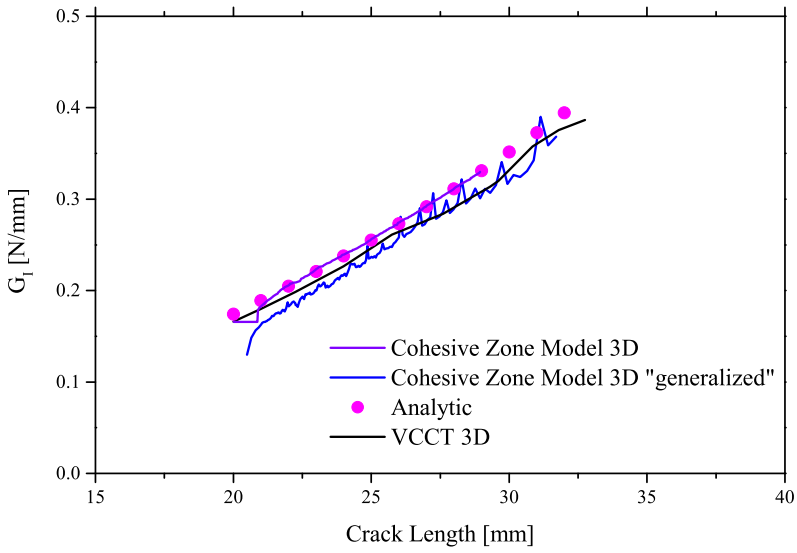

Figure 5.5: Comparison of a – G_I values

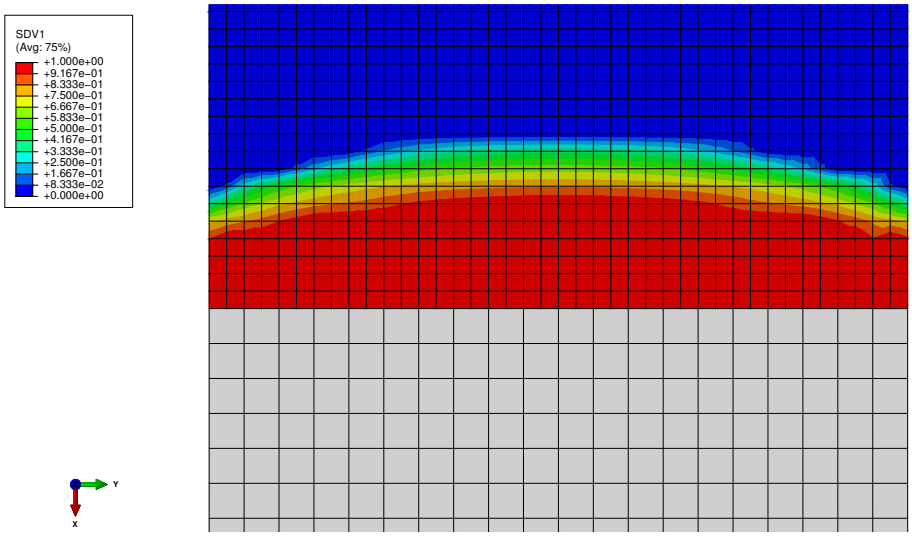

Figure 5.6: Crack front during the fatigue simulation

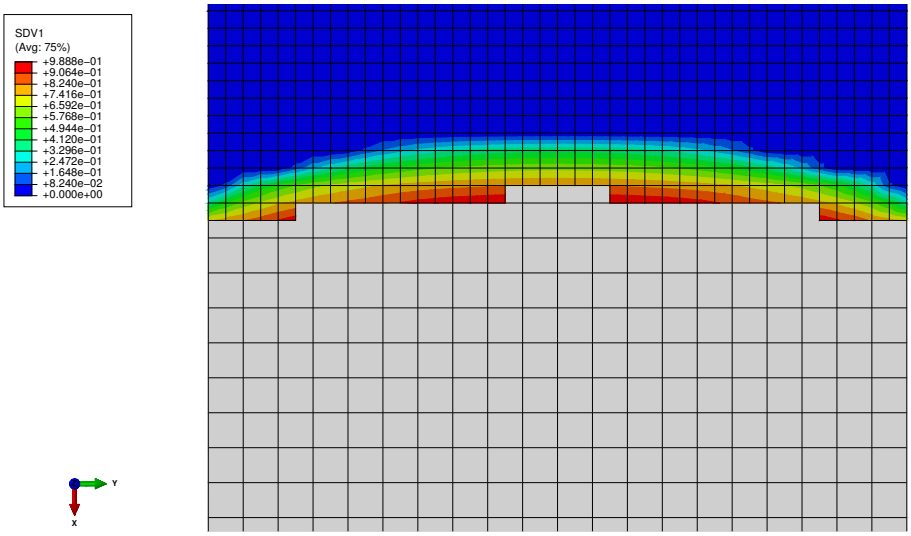

Figure 5.7: Crack front during the fatigue simulation (fully damaged element are deleted)

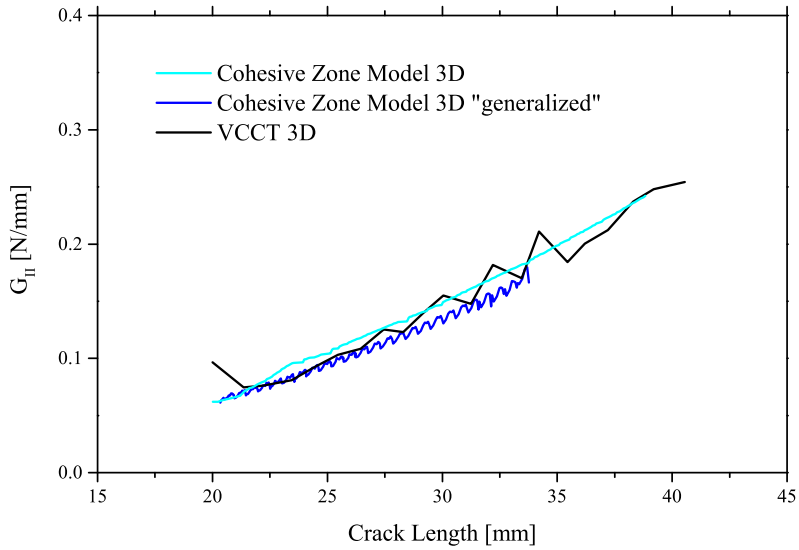

Figure 5.8: Comparison of a – G_{II} values

5.4 Conclusions

A new procedure for simulating fatigue debonding/delamination with cohesive zone is presented. Unlike the previous approach, propagation of arbitrarily shaped cracks can

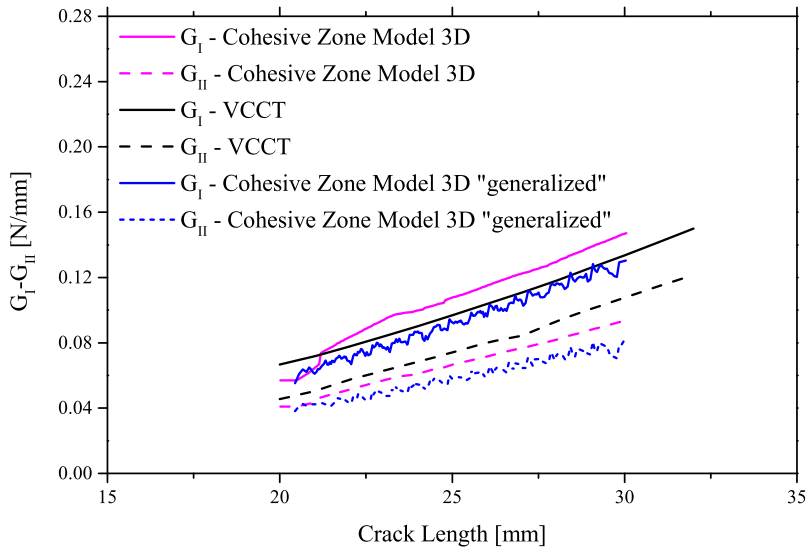

Figure 5.9: Comparison of a – G_I /$G_{I\ I}$ values

be simulated. Regular hexehedral meshes in cohesive zone are needed. So far this approach has been tested on simple geometries (DCB, ELS and MMELS) for adhesively bonded joints with adherends made by isotropic material. The results have shown a good agreement with previous FEA analysis (VCCT and CZM), but this approach requires further valdiations with proper technique, computational or experimental. Also the VCCT, implemented in commercial codes, cannot be attractive for this kind of delamination problems. The mesh can highly influence the results due to the fact that the nodes that must be released during the simulation. Also orthogonal mesh patterns becomes problematic due to the changing position and shape of the delamination front; the associated non-linear iterations, could make the analysis prohibitively large in most cases.

The next figures show a qualitative example of a fatigue simulation in a DCB test where the initial defect shaped like one quarter of ellipse.

Calculation time is increased in the worst case of about 2%, compared to the CZM 3D for planar cracks.

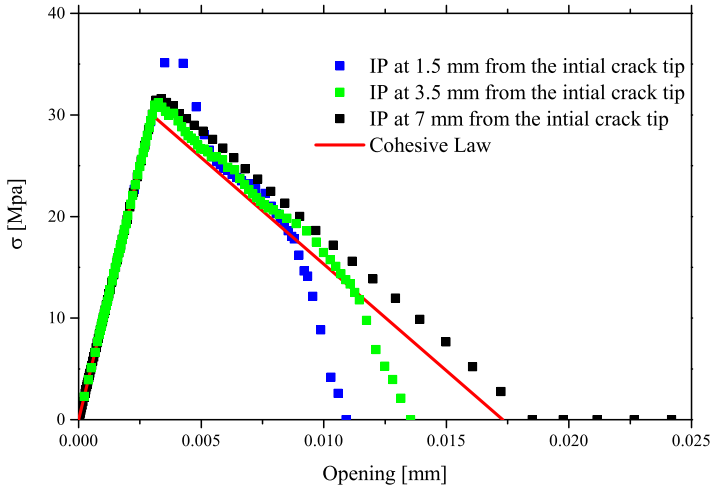

Figure 5.10: Fatigue Degradation of IP at half thickness for a DCB simulation ($\Delta D_{max} = 0.2$)

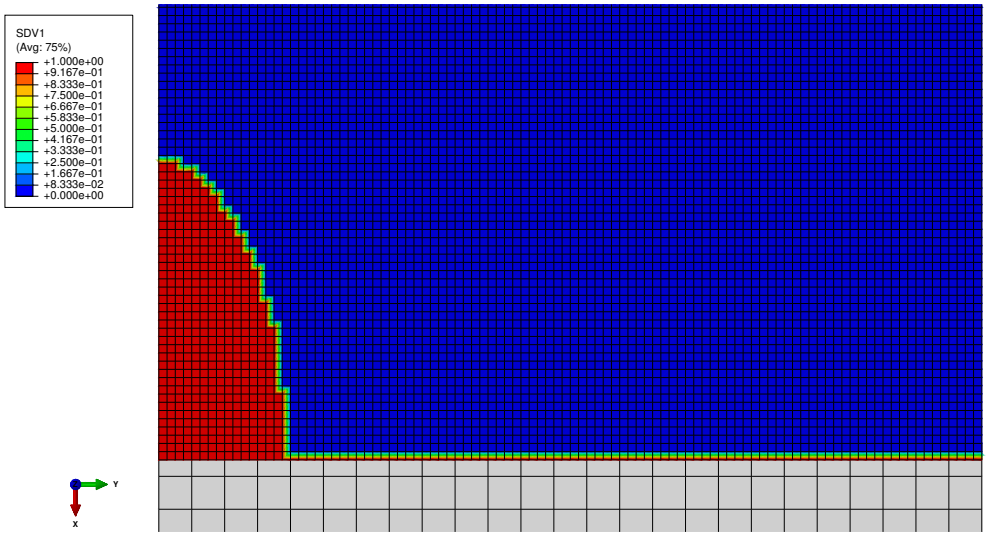

Figure 5.11: Initial crack front

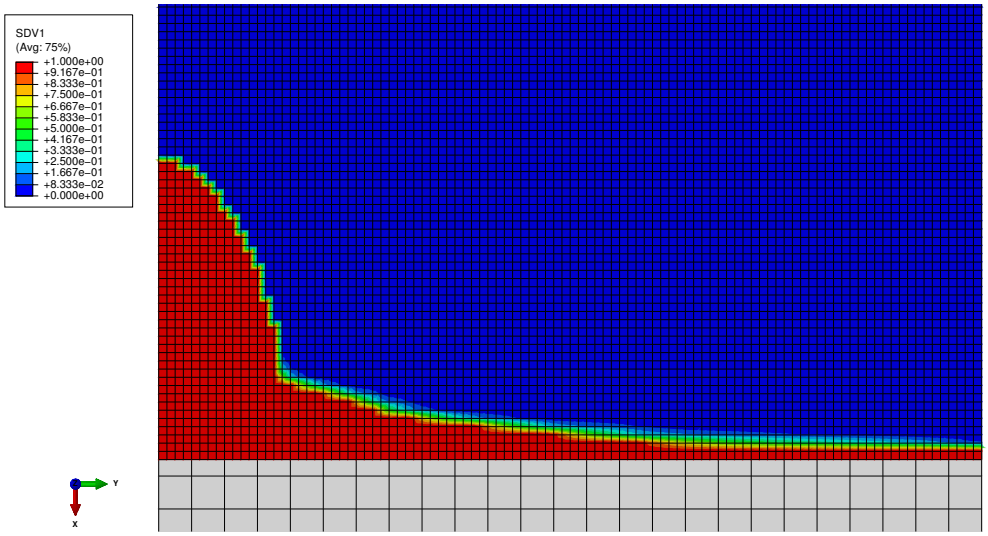

Figure 5.12: Crack front during the simulation (increment 120)

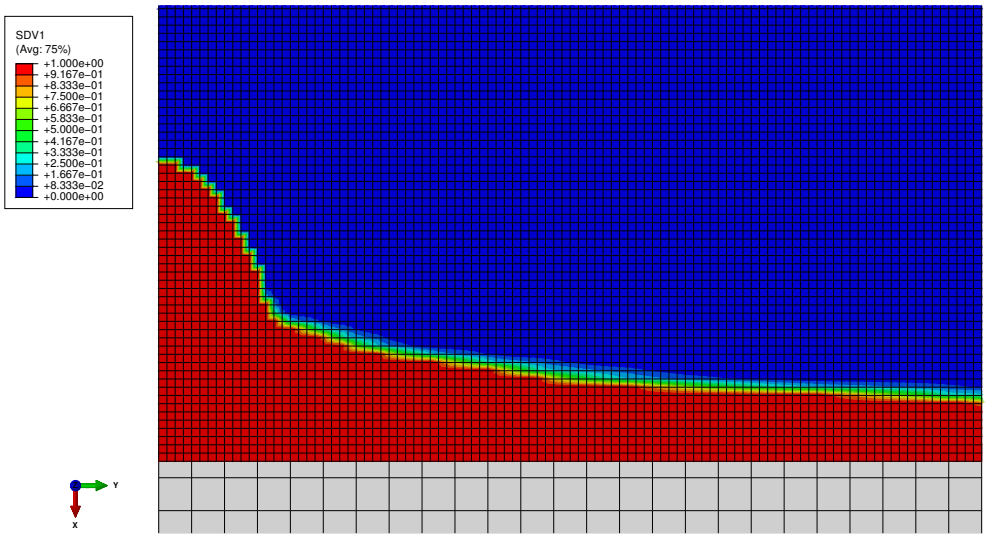

Figure 5.13: Crack front during the simulation (increment 450)

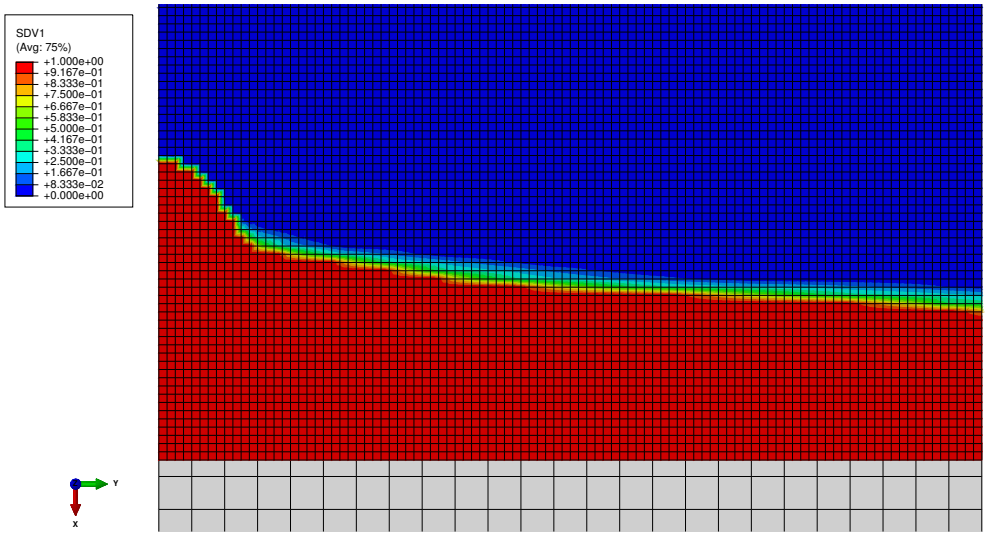

Figure 5.14: Crack front during the simulation (increment 1045)

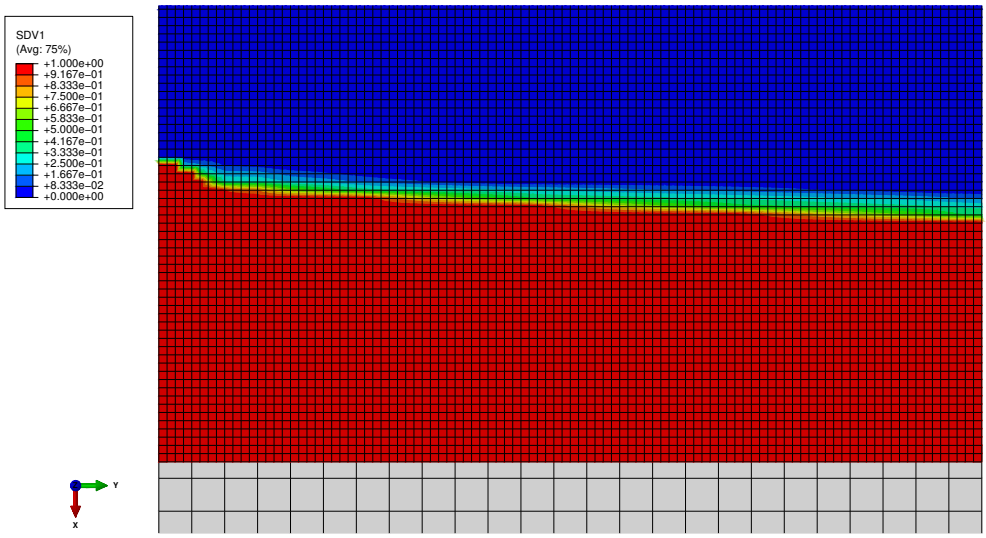

Figure 5.15: Crack front during the simulation (increment 1400)

References

[1] Griffith AA, 1920. The phenomena of rupture and flows in solids. Transactions, Royal Society of London, vol. 221.

[2] Lemaitre J, Chaboche J L1978. Aspect Phenomenologique de la Rupture per Endommagement, J. Méch. Applique (2), pp. 317-365

[2] Irwin G, 1957. Analysis of stress and strains near the end of a crack traversing a plate, J. Applied Mech. 24, 361-364.

[3] Rice J, 1968. A path indipendent integral and the approximate analysis of strain concentration by notched and cracks, J. Applied Mech. 35, 379.

[5] Hutchinson J, 1968. Plastic stress and strain fields at a crack tip, J. Mech. Phys. Solids 16, 337-342.

[6] Hutchinson J, 1968. Singular behavior at the end of a tensile crack in a hardening material, J. Mech. Phys. Solids 16, 13-31.

[7] Rice J, Rosengren G, 1968. Plane strain deformation near a crack tip in a power-law hardening material, J. Mech. Phys. Solids 16, 1-12.

[8] Rybicki EF, Kanninen MF, 1977.A Finite Element Calculation of Stress Intensity Factors by a Modified Crack Closure Integral, Eng. Fracture Mech., Vol. 9, pp. 931-938.

[9] Dugdale DS, 1960. Yielding of steel sheets containing slits, J. Mech. Phys. Solids 8, 100-104.

[10] Barenblatt G, 1962. The mathematical theory of equilibrium cracks in brittle fracture, Advances in Applied Mechanics 7, 55-129.

[11] Hillerborg A, Modeer M, Petersson PE, 1976. Analysis of crack formation and crack growth in concrete by means of fracture mechanics and finite elements, Cement Concrete Res. 6, 773-782.

[12] Petersson PE, 1981. Crack growth and development of fracture zones in plain concrete and similar materials, Technical Report, Division of Building Materials, Lund Institute of Technology.

[13] Carpinteri A, 1986. Mechanical damage and crack growth in slits, Martinus Nijhoff Kluwer.

[14] Brocks W, Cornec A, Scheider I, 2003. Computational Aspects of Nonlinear Fracture Mechanics. In: I. Milne, R.O. Ritchie, B. Karihaloo (Eds.): Comprehensive Structural Integrity. Fracture of Materials from Nano to Macro, Vol. 3: Numerical and Computational Methods, pp. 127-209.

[15] Brocks W, Cornec A, 2003. Cohesive models - special issue, Eng. Fract. Mech. 70(14), 1741-1986.

[16] Krenk K, 1992. Energy release rate of symmetric adhesive joints, Eng. Fract. Mech., 43(4), pp. 549-559.

[17] Paris P, Erdogan F, 1963. A critical analysis of crack propagation laws, J. Basic Eng. 85, pp. 528–534.

[18] Paris P, 1964. The fracture mechanics to fatigure, 10th Sagamore Army Material Research Conference, Syracuse University Press., pp. 107-132.

[19] Mostovoy S, Ripling E J, 1975. Flaw tolerance of a number of commercial and experimental adhesives. Adhesion science and technology, L H Lee (ed) 9. B, Plenum Press, NY, pp. 513–562.

[20] Russel A J, Street K N, 1987. The effect of matrix toughness on delamination: static and fatigue fracture under mode II shear loading of graphite fiber composites. Toughened Composites, ASTM STP 937, American Society for Testing and Materials, Philadelphia, PA, pp. 275-294.

[21] Russel A J, Street K N, 1988. A constant ΔG test for measuring mode I interlaminar fatigue crack growth rates, ASTM STP 972, American Society for Testing and Materials, Philadelphia, PA, pp. 259-277.

[22] Bernasconi A, Jamil A, Moroni F, Pirondi A, 2013. A study on fatigue crack propagation in thick composite adhesively bonded, International Journal of Fatigue, 50, pp. 18-25.

[23] ASTM D 3433 – 99, Standard Test Method for Fracture Strength in Cleavage of Adhesives in Bonded Metal Joints

[24] ASTM D 5528 – 01, Standard Test Method for Mode I Interlaminar Fracture Toughness of Unidirectional Fiber-Reinforced Polymer Matrix Composites

[25] ASTM WK22949, New test for determination of mode II interlaminar fracture toughness of unidirectional fiber reinforced plymer matrix composites using the End-Notched Flexure (ENF) test

[26] Crews J H, Reeder J R, 1988. A Mixed-Mode Bending Apparatus for Delamination Testing, NASA Technical Memorandum 100662, NASA Langley Research Center, Hampton, Va.

[27] Crews J H, Reeder J R, 1990. The Mixed-Mode Bending Method for Delamination Testing, AIAA Journal, Vol. 28, No. 7, pp. 1270-1276.

[28] ASTM D 6671/D 6671M - 06, Standard Test Method for Mixed Mode I-Mode II Interlaminar Fracture Toughness of Unidirectional Fiber Reinforced Polymer Matrix Composites.

[29] Murri G B, 2013. Evaluation of delamination onset and growth characterization methods under mode I fatigue loading. Tech Rep NASA/TM-2013-217966, NASA.

[30] Ishii K, Imanaka M, Nakayama H, Kodama H, 1999. Evaluation of the fatigue strength of adhesively bonded CFRP/metal single and single-step double-lap joints, Compos Sci Technol, 59, 1675–1683.

[31] Dessureault M, Spelt J K, 1997. Observations of fatigue crack initiation and propagation in an epoxy adhesive, Int J Adhes Adhes, 17, 183–195.

[32] Potter K D, Guild F J, Harvey H J, Wisnom M R, Adams R D, 2001. Understanding and control of adhesive crack propagation in bonded joints between carbon fibre composite adherends I. Experimental, Int J Adhes Adhes, 21, 435–443.

[33] Ashcroft I A, Abdel Wahab M M, Crocombe A D, Hughes D J, Shaw S J, 2001. The effect of environment on the fatigue of bonded composite joints. Part 1: testing and fractography, Composites A, 32, 45–58.

[34] Pascoe J A, Alderliesten R C, Benedictus R, 2013. Methods for the prediction of fatigue delamination growth in composites and adhesive bonds – A critical review, Engineering Fracture Mechanics, pp. 72-96

[35] Lemaitre J, 1985. A continuous damage mechanics model for ductile fracture. Trans. ASME, J. Engng Mat. Tech. 107, pp. 83-89.

[36] Crocombe A D, Richardson G, 1999. Assessing stress state and mean load effects on the fatigue response of adhesively bonded joints, Int J Adhes Adhes, 19, 19–27.

[37] Quaresimin M, Ricotta M, 2006. Fatigue behavior and damage evolution of single lap bonded joints in composite material, Compos Sci Technol, vol. 66, no. 2, pp. 176–187.

[38] Zhang Z H, Shang J K, and Lawrence F V, 1995. A backface strain technique for detecting fatigue-crack initiation in adhesive joints, The Journal of Adhesion , vol. 49, no. 1-2, pp. 23–36.

[39] Khoramishad H, Crocombe A D, Katnam K B, Ashcroft I A, 2010. A generalized damage model for constant amplitude fatigue loading of adhesively bonded joints, Int J of Adhes and Adhes, vol. 30, no. 6, pp. 513–521.

[40] Graner Solana A, Crocombe A D, Ashcroft I A, 2010. Fatigue life and backface strain predictions in adhesively bonded joints, Int J of Adhes and Adhes, vol. 30, no. 1, pp. 36–42.

[41] Shenoy V, Ashcroft I A, Critchlow G W, Crocombe A D, Abdel Wahab M M, 2009. An investigation into the crack initiation and propagation behavior of bonded single lap joints using backface strain, Int J of Adhes and Adhes, vol. 29, no. 4, pp. 361–371.

[42] Deng J, Lee M M K, 2007. Fatigue performance of metallic beam strengthened with a bonded CFRP plate, Composite Structures, vol. 78, no. 2, pp. 222–231.

[43] Crocombe A D, Ong C Y, Chan C M, Abdel Wahab M M, and I. A. Ashcroft, 2002. Investigating fatigue damage evolution in adhesively bonded structures using backface strain measurement, The Journal of Adhesion, vol. 78, no. 9, pp. 745–776.

[44] Capell T F, Palaniappan J, Ogin S L et al., 2007. The use of an embedded chirped fibre Bragg grating sensor to monitor disbond initiation and growth in adhesively bonded composite/metal single lap joints, Journal of Optics A, vol. 9, no. 6, article S07, pp. S40–S44.

[45] Ishii K, Imanaka M, Nakayama H, Kodama H, 1999. Evaluation of the fatigue strength of adhesively bonded CFRP/metal single and single-step double-lap joints, Composites Science and Technology, vol. 59, no. 11, pp. 1675–1683.

[46] Zeng Q, Sun C T, 2004. Fatigue performance of a bonded wavy composite lap joint, Fatigue & Fracture of Engineering Materials & Structures, vol. 27, no. 5, pp. 413–422.

[47] Foulk III JW, Allen D H, Helms K L E, 1998. A model for predicting the damage and environmental degradation dependent life of SCS-6/Timetal 21S $[0]_4$ metal matrix composite, Mech Mater; 29(1): pp. 53–68.

[48] De Andrés A, Pérez J L, Ortiz M, 1999. Elastoplastic finite element analysis of three-dimensional fatigue crack growth in aluminum shafts subjected to axial loading, International Journal of Solids and Structures, vol. 36, no. 15, pp. 2231–2258.

[49] Liu J, Li J, Wu B, 2013. The cohesive zone model for fatigue crack growth, Advances in Mechanical Engineering, Volume 2013, Article ID 737392, 16 pages

[50] O, Repetto E A, Ortiz M, Radovitzky R A, 2001. A cohesive model of fatigue crack growth, Int J Fract 2001, 110(4): pp. 351–369.

[51] Yang B, Mall S, Ravi-Chandar K, 2001. A cohesive zone model for fatigue crack growth in quasibrittle materials, Int J Solids Struct, 38(22–23): pp. 3927–3944.

[52] Roe K L, Siegmund T, 2003. An irreversible cohesive zone model for interface fatigue crack growth simulation, Eng Fract Mech, 70(2):209–232.

[53] Peerlings R H J, Brekelmans W A M, de Borst R, Geers M G D, 2000. Gradient-enhanced damage modelling of high-cycle fatigue, Int J Numer Methods Eng, 49(12): pp. 1547–1569.

[54] Robinson P, Galvanetto U, Tumino D, Bellucci G, Violeau D, 2005. Numerical simulation of fatigue-driven delamination using interface elements, Int J Numer Methods Eng, 63(13): pp. 1824-1848

[55] Paas M H J W, Schreurs P J G., Brekelmans W A M, 1993. A continuum approach to brittle and fatigue damage: theory and numerical procedures, International Journal of Solids and Structures, 30: pp. 579-599

[56] Blanco N, Gamstedt E K, Asp L E, Costa J, 2004. Mixed-mode delamination growth in carbon–fibre composite laminates under cyclic loading, Int J Solids Struct; 41(15): pp. 4219–4235.

[57] Tumino D, Cappello F, 2007. Simulation of fatigue delamination growth in composites with different mode mixtures, J Compos Mater, 41(20): pp. 2415–2441.

[58] Muñoz J J, Galvanetto U, Robinson P, 2006. On the numerical simulation of fatigue driven delamination with interface elements, Int J Fatigue, 28(10): pp. 1136–1146.

[59] Harper P W, Hallett S R, 2010. A fatigue degradation law for cohesive interface elements – development and application to composite materials. Int J Fatigue, 32(11): pp. 1774–1787.

[60] Asp LE, Sjögren A, Greenhalgh E, 2001. Delamination growth and thresholds in a carbon/epoxy composite under fatigue loading, J Compos Tech Res, 23(2): pp. 55–68.

[61] Turon A, Costa J, Camanho P P, Dávila C G, 2007. Simulation of delamination in composites under high-cycle fatigue, Composites Part A; 38(11): pp. 2270–2282.

[62] H, Crocombe A D, Katnam K B, Ashcroft I A, 2010. Predicting fatigue damage in adhesively bonded joints using a cohesive zone model, Int J Fatigue, 32(7): pp. 1146–1158.

[63] May M, Hallett S R, 2010. A combined model for initiation and propagation of damage under fatigue loading for cohesive interface elements, Composites Part A , 41(12): pp. 1787–1796.

[64] May M, Hallett S R, 2011. An advanced model for initiation and propagation of damage under fatigue loading – Part I: Model formulation, Composite Structures; 93(9): pp 2340–2349

[65] Pirondi A, Moroni F, 2010. A progressive damage model for the prediction of fatigue crack growth in bonded joints, J Adhes, 86 (5–6): pp. 501–521.

[66] Moroni F, Pirondi A, 2011. A procedure for the simulation of fatigue crack growth in adhesively bonded joints based on the cohesive zone model and different mixed-mode propagation criteria, Eng Fract Mech; 78(8): pp. 1808–1816.

[67] Moroni F, Pirondi A, 2012. A procedure for the simulation of fatigue crack growth in adhesively bonded joints based on a cohesive zone model and various mixed-mode propagation criteria, Engineering Fracture Mechanics, 89, pp. 129–138.

[68] Harper W P, Hallett S R, 2008. Cohesive zone length in numerical simulations of composite delamination, Engineering Fracture Mechanics, 75, pp. 4774–4792.

[69] Ungsuwarungsru T, Knauss, W G, 1987. The role of Damage-Softened Material Behaviour in the Fracture of Composites and Adhesives, International Journal of Fracture 35, pp. 221-241.

[70] Kenane M, Benzeggagh M L, 1996. Measurement of mixed mode delamination fracture toughness of unidirectional glass/epoxy composites with mixed mode bending apparatus, Composite Science and Technology, 56, pp. 439-449.

[71] Dassault Systèmes, Abaqus 6.11 Documentation, Analysis User's Manual.

[72] Krueger R, 2010. NASA=CR-2010-216723, NIA Report No. 2010-04.

[73] Pirondi A, Giuliese G, Moroni F, Bernasconi A, Jamil A, "Simulation of fatigue delamination/debonding using cohesive zone and virtual crack closure," in "Fatigue and fracture of adhesively bonded composite joints: Behaviour, simulation and modeling", edited by A. P. Vassilopoulos, ed: Woodhead Ed., (Pubblished).

[74] Wang Y, Williams J G, 1992. Corrections for mode II fracture toughness specimens of compostite materials, Composites Sci. Technol., 43, pp. 251-256

[75] Blanco N, Gamstedt E K, Costa J, Trias D, 2006. Analysis of the mixed-mode end load split delamination test, Composite Structure 76, pp. 14-20

[76] Moroni F, Pirondi A, Giuliese G, Simulation of fatigue debonding in adhesively bonded threedimensional joint geometries using a cohesive zone model approach, IGF XXII – 22nd Congress of the Italian Group on Fracture, Rome, Italy, 1–3 July (2013).

[77] Giuliese G, Pirondi A, Moroni F, Bernasconi A, Jamil A, Nikbakht A, Fatigue delamination: A comparison between virtual crack closure and cohesive zone simulation techniques, presented at the 19th ICCM Toronto, Canada, July 2013.

[78] Xie De, Biggers Sherill B, 2006. Strain Energy Release Rate calculation for a moving delamination front of arbitrary shape based on the virtual crack closure technique. Part I: formulation and validation, Engineering Fracture Mechanics, 73(6): pp. 771-785

[79] Chiarelli M, Frediani A, 1993. A computation of the three-dimensional J-integral for elastic materials with a view to applications in fracture mechanics, Engineering Fracture Mechanics, pp. 763–788.

[80] Hakimelahi B, Soltani N, 2010. 3D J-integral evaluation using the computation of line and surface integrals, Fatigue and Fracture of Engineering Materials and Structures 33, pp. 661-672

[81] Cui W, Wisnom M R, Jones M, 1992. A Comparison of Failure Criteria to Predict Delamination of Unidirectional Glass/Epoxy Specimens Waisted Through the Thickness, Composites 23(3): pp. 158-166.

[82] Krueger R. An approach to assess delamination propagation simulation capabilities in commercial finite element codes, NASA TM/2008-215123.

[83] Krueger R, Goetze D. Influence of finite element software on Strain Energy Release Rates computed using the virtual crack closure technique, NASA/CR- 2006-214523.

[84] Pietropaoli E, Riccio A, 2011. Formulation and assessment of an enhanced finite element procedure for the analysis of delamination growth phenomena in composite structures, Composites Science and Technology 71: pp. 836–846.

Ringraziamenti

Giunto al termine di questo mio 'viaggio', la prima persona che sento di ringraziare è il mio tutor, prof. Alessandro Pirondi, per il continuo supporto durante il mio percorso di dottorato. A lui va tutta la mia gratitudine, in quanto ha reso questo triennio una indimenticabile esperienza non solo dal punto di vista professionale ma anche umano.

Vorrei ringraziare inoltre:

Fabrizio Moroni, dal quale ho 'ereditato' il progetto di ricerca che ho svolto, per la pazienza che mi ha dimostrato e la disponibilità che non mi ha mai fatto mancare;

Enrico Bedogni, per la simpatia e per i suoi preziosi consigli sulla programmazione Fortran;

Azhar Jamil, del Politecnico di Milano, con il quale ho condiviso diversi mesi di lavoro, anche se a distanza. Lo scambio di idee avuto con lui è stato sempre produttivo e il sostegno reciproco soprattutto prima delle scadenze delle *submission* è stato di grande aiuto.

Infine, il mio Grazie va anche a: Giovanni Chiodo, il mio collega di dottorato, e Matteo Vettori, Stefano Pini e Luca Romoli per i tanti momenti spassosi passati insieme.